

A new EOS module for the atmosphere modelling code **PHOENIX**

Dissertation

zur Erlangung des Doktorgrades
an der Fakultät für Mathematik, Informatik und Naturwissenschaften
Fachbereich Physik
der Universität Hamburg

vorgelegt von

Marlies Meyer

Hamburg

2017

Gutachter der Dissertation:	Prof. Dr. Peter H. Hauschildt Prof. Dr. Ralph Neuhäuser
Zusammensetzung der Prüfungskommission:	Prof. Dr. Robi Banerjee Prof. Dr. Peter H. Hauschildt Prof. Dr. Dieter Horns Prof. Dr. Jochen Liske Prof. Dr. Jürgen H. M. M. Schmitt
Vorsitzender der Prüfungskommission:	Prof. Dr. Jochen Liske
Datum der Disputation:	12.07.2017
Vorsitzender Fach-Promotionsausschusses Physik:	Prof. Dr. Wolfgang Hansen
Leiter des Fachbereichs Physik:	Prof. Dr. Michael Potthoff
Dekan der Fakultät MIN:	Prof. Dr. Heinrich Graener

Zusammenfassung

PHOENIX ist ein allgemeiner Atmosphärencode. Um seine Fähigkeit bezüglich der Modellierung terrestrischer Bedingungen zu verbessern, wird ein neues Zustandsgleichungsmodul benötigt. Diese sogenannte EOS (**e**quation **o**f **s**tate) soll die chemische Zusammensetzung bei geringen Effektivtemperaturen von typischerweise wenigen hundert Kelvin bestimmen. Die EOS 'SESAM', welche auf die Methode von Villars-Cruise-Smith beruht, ist in diesem Zusammenhang geeignet. Sie kann Umgebungen meistern, die eine große Anzahl chemischer Spezies in einem breiten Temperatur- und Druckbereich aufweisen und geladene, inerte und kondensierte Spezies beinhalten, welche auch in Spuren vorkommen können. Zusätzlich besitzt diese EOS einen modernen und modularen Aufbau und ist leicht auf weitere Anwendungsbereiche erweiterbar.

SESAM wurde in PHOENIX eingebaut und das Zusammenspiel der beiden Codes wurde in dieser Arbeit diskutiert. In allen getesteten Atmosphären lieferte SESAM zu jeder Zeit numerisch stabile chemische Zusammensetzungen, was eine geradlinige Konvergenz von PHOENIX erzeugte. Darüber hinaus wurde SESAMs hervorragendes Konvergenzverhalten und die Zuverlässigkeit der Ergebnisse bei Variationen der anfänglichen Spezieshäufigkeiten präsentiert. Es folgte eine Nachberechnung der Tests mit ACES, der derzeit in PHOENIX verwendeten EOS. Für eine bessere Vergleichbarkeit wurde ACES insofern angepasst, dass Spezies, die in Spuren vorkommen, konsistent mit allen anderen Spezies behandelt wurden, anstelle der sonst in ACES verwendeten Festlegung einer voreingestellten geringen Häufigkeit. Dies beeinflusste das Konvergenzverhalten von PHOENIX und erzeugte Schwankungen in den Druckwerten zwischen den PHOENIX-Iterationen, welche bei der Verwendung von SESAM nicht auftraten. Es wurde gezeigt, dass die von ACES berechneten chemischen Zusammensetzungen stark von den anfänglichen Spezieshäufigkeiten abhängten. Dadurch erscheint die Stabilität von ACES Ergebnissen fragwürdig, wenn Spurenspezies explizit berücksichtigt werden. Hinsichtlich der Atmosphärenstruktur und des Spektrums waren die Abweichungen zwischen ACES und SESAM in den konvergierten PHOENIX-Modellen insgesamt gering. Dies deutet auf eine ausreichend physikalische Übereinstimmung der zwei EOS hin. Anschließend folgte ein Vergleich der Rechenzeiten beider EOS. Als Resultat benötigte SESAM für die Lösung des chemischen Gleichgewichtsproblems weniger Iterationen als ACES, wobei ACES dafür etwas weniger Zeit verwendete.

SESAM wurde erfolgreich in PHOENIX eingebaut. Obwohl eine weitere Entwicklung von PHOENIX bezüglich einer verbesserten Behandlung von erdähnlichen Atmosphären notwendig ist, bildet SESAM bereits eine solide Basis für zukünftige Anwendungen.

Abstract

PHOENIX is a general-purpose atmosphere modelling code. To enhance its capability to model terrestrial conditions, a new equation of state (EOS) module is required to determine the chemical compositions at low effective temperatures of typically few hundred Kelvin. The EOS 'SESAM', based on the Villars-Cruise-Smith method, is appropriate in this context. This EOS can handle environments with a high number of chemical species in a wide temperature and pressure range including charged, inert, condensed, and trace species. Furthermore, it has a modern and modular design and is easily expandable to other applications.

SESAM has been implemented in the PHOENIX framework and the interplay between both codes is discussed in this thesis. In all stellar models tested, SESAM produced a straightforward convergence of PHOENIX by providing numerically stable chemical compositions at all times. In addition, SESAM's excellent convergence behaviour and reliability of the results considering variations in the initial species abundances are presented.

The tests were recalculated using ACES, which is the EOS currently used in PHOENIX. For a better comparability, ACES was adjusted to treat trace species consistently with all other species rather than default to an arbitrarily chosen small value. This influenced PHOENIX convergence behaviour, resulting in pressure fluctuations between PHOENIX iterations, which did not occur when SESAM was applied. It is shown that the chemical compositions calculated by ACES strongly depend on the initial species abundances, questioning the stability of ACES's solutions when trace species are explicitly taken into account. With respect to the atmosphere structure and the spectrum, the deviations in the converged PHOENIX models between ACES and SESAM were overall minor. This indicates a sufficient physical agreement of both EOS's. Finally, the computational times of the two EOS's were compared. As a result, SESAM needed less iterations than ACES to solve the chemical equilibrium problem, whereas ACES required slightly less time.

SESAM was successfully included in PHOENIX. Although further development of PHOENIX is required for an improved treatment of Earth-like atmospheres, this new EOS provides a solid basis for future applications.

Contents

1	Introduction	1
2	Theory: Stellar atmospheres	4
2.1	Overview	4
2.2	Radiative transfer	6
2.2.1	Energy level populations	7
2.2.2	Solutions to the radiative transfer equation	9
3	Theory: The chemical equilibrium	11
3.1	The equation of state	12
3.2	The chemical equilibrium as a minimisation problem	13
3.3	The chemical potential	15
3.4	The approach of optimised stoichiometry	16
4	Methods: The atmosphere model code and its new EOS module	21
4.1	The new EOS module SESAM	21
4.1.1	Iterative method: Constraints of constant (T, P)	22
4.1.2	Treatment of condensed species and ions	27
4.1.3	Convergence behaviour	28
4.2	The atmosphere model code PHOENIX	30
4.3	Modifications and settings for the synergy of SESAM with PHOENIX	32
5	Results: Testing the new EOS module	37
5.1	Atmospheric temperature and pressure structure	38
5.2	Spectrum	54
5.3	Initial species abundances	56
5.4	Further model atmospheres	61
5.5	Computational performance	70
6	Conclusions and Outlook	72
	Appendix	77
	Bibliography	84

Chapter 1

Introduction

Atmosphere modelling

The solar surface is the only stellar surface observable with high detail. For all other stars, there are limited possibilities to directly access and understand their physical properties. The energy in terms of radiation released by the stars is an important source of information: photons interact with matter according to absorption, re-emission, and scattering processes, and travel through space until they impinge onto our telescopes. The photons' ensemble carries the signature of the stellar electromagnetic spectrum. Only by means of atmosphere modelling and the comparisons of observed and synthetic spectra it became possible to understand many of the physical processes involved. Furthermore, essential stellar properties could be determined such as, for instance, the effective temperature and the surface gravity. Over the last decades, a number of codes were developed, which significantly contributed to it: **ATLAS** (Kurucz, 1970), **MARCS** (Gustafsson et al., 1975), **TLUSTY** (Hubeny, 1988), **MULTI** (Carlsson, 1988), **PHOENIX** (Hauschildt, 1992, 1993), **PoWR** (Gräfener et al., 2002) to mention few. Since the beginning, huge progress was made by improvements considering numerical techniques, computing power and the quantity and accuracy of atomic data. In particular high-performance computing allowed to expand the complexity of the simulations to multi-dimensional computations of photospheres and are performed by, e.g., **MULTI3D** (Botnen and Carlsson, 1999), **CO⁵BOLD** (Freytag et al., 2002), and **PHOENIX/3D** (Hauschildt and Baron, 2014, and previous). Nevertheless, these models still rely on strong simplifications of physical and chemical processes.

Chemical equilibrium

The chemical composition of a stellar atmosphere determines the shape and features of the spectrum. This makes a detailed consideration of the neutral atoms, molecules, ions, and in cool stars even condensed species and dust grains, an essential requirement for state-of-the-art atmosphere simulations. An equation of state (EOS) provides an approximation of these chemical compositions by determining a chemical equilibrium once the parameters of the equilibrium problem are specified. These parameters depend on the algorithm applied and can be, e.g., the temperature, gas pressure, element abundances, a list of species assumed to be relevant, and the species' standard chemical potentials. The chemical equilibrium state can be considered as the limiting case of a system of chemical reactions. This assumption is appropriate when the chemical reactions are sufficiently rapid to attain a locally stable equilibrium state. This condition is given in atmospheres

that are approximated as quasi-static where the chemical system adapts quicker to local conditions than radiative and hydrodynamic processes change them.

At the end of the 19th century, major parts of the theory behind the chemical equilibrium in ideal systems has been formulated. Scientists like Cato Maximilian Guldberg and Peter Waage (Guldberg and Waage, 1864, law of mass action), Josiah Willard Gibbs (Gibbs, 1873, concept of chemical potential), Jacobus Henricus van't Hoff (Van't Hoff, 1884, "Studies in Chemical Dynamics"), Henry Louis Le Chatelier (Chatelier, 1884, Le Chatelier's principle), Walther Nernst (third law of thermodynamics), to name a few, substantially contributed to this. Especially the reinforced research in the 1940s considering rocket science in Germany and the 1950s for space science in the United States created the need for calculations of complex chemical systems. Building on the achievements in the mathematical description of chemical equilibria and the initial advancements in the development of computers, the first general-purpose algorithms did arise, e.g., the codes described in Brinkley (1947), White et al. (1958), and Naphtali (1959). The early algorithms mainly handled ideal, gaseous systems. Most of these codes were only partially capable or even failing in treating complex systems that include several hundreds of chemical species along with multi-phase systems (Smith, 1980). Within the last 60 years, various different approaches were developed like, for instance, the stoichiometric (e.g. Naphtali, 1959, 1961; Smith and Missen, 1982) and non-stoichiometric methods (e.g. Brinkley, 1947; Huff et al., 1951; White et al., 1958; Gordon and McBride, 1971; Freedman, 1982), and the element-potential method (e.g. Reynolds, 1986; Pope, 2003). Chemical non-equilibria are considered in the chemical kinetics approach (e.g. Reaction Design, 2016) and the rate-controlled constrained-equilibrium method (e.g. Keck, 1990; Bishnu et al., 1997; Metghalchi, 2009). Now it is possible to calculate large non-ideal systems that consist of multiple phases. The complexity of the system is mainly only limited by the available computational power and time, while the chemical and physical accuracy is mostly restricted by the quality of the measured and theoretically assessed thermodynamic data of the species.

A new equation of state module for PHOENIX

A promising future application of PHOENIX is the simulation of terrestrial-like atmospheres of objects like, e.g., the planets Venus and Mars, Saturn's moon Titan, and extrasolar planets. These atmospheres have typically low temperatures of only a few hundred Kelvin. The currently used EOS in PHOENIX, ACES, was neither explicitly designed nor verified to handle such low temperatures. The first step towards the simulation of terrestrial atmospheres is, therefore, to utilize an EOS in PHOENIX, which is capable to handle the respective low-temperature conditions. In addition, the new EOS must manage complex systems involving several hundreds of species, including neutral atoms, molecules, ions, and trace species. The chemical compositions must be determined reliably without convergence problems for the environments of terrestrial planets. Furthermore, an expansion to all conditions relevant in stellar atmospheres is favourable. These systems are varying from low temperatures and pressures in cool dwarfs where mostly molecules and neutral atoms are present in the atmosphere, to high temperatures and pressures in hot stars, dominated by ions and neutral species. Due to the fact that PHOENIX requests equilibrium compositions more than a thousand times in each iteration and its multi-dimensional configuration, PHOENIX/3D, even millions of times, the EOS must rapidly converge to not significantly

increase the computational time of the simulation.

The new EOS module **SESAM** (Stoichiometric Equilibrium Solver for Atoms and Molecules) meets the criteria for these essential requirements, allowing to reliably determine the equilibrium compositions (Meyer, 2013, where it was denoted as **StoiCES**). Based on the Villars-Cruise-Smith algorithm, it applies the optimised stoichiometric method. Compared to other approaches, this method has the advantage of showing a very good convergence behaviour, even if many condensed species and a high number of trace species are considered (Smith and Missen, 1982; Wong et al., 2003). For instance, non-stoichiometric codes bear the risk of convergence problems and matrix singularities that may occur when condensed species or phase-transitions are involved (Smith and Missen, 1982). In addition, the presence of trace species significantly prolongs the iterative processes in non-stoichiometric codes (Ruda, 1982). In environments where the hydrodynamic time-scales are in the same order of magnitude as the chemical reaction time-scales, a chemical kinetics approach is required. Depending on the number of species involved, the necessary identification of sets of reactions will result in enormous computational times. This issue is simplified by the rate-controlled constrained-equilibrium approach. This method is sophisticated and chemical equilibria are calculated efficiently only if the system's constraints are specified carefully.

All these considerations make **SESAM** a suitable new EOS module to improve the quality and numerical stability of the atmosphere modelling with **PHOENIX**. It is a modern and modular code, which has been designed specifically for the purpose of the low-temperature environments. Moreover, **SESAM** is easily extendible to other applications like, e.g., non-ideal systems, taking multi-phases and phase-transitions into account. This provides a promising initial step towards the simulation of terrestrial atmospheres with **PHOENIX**.

Goals and chapter overview of this thesis

Stellar modelling includes a vast number of different physical processes and the radiative transfer theory plays a major role in this context, describing the transport of photons through matter. Chapter 2 provides an introduction to radiative transfer theory, along with an overview of other physical phenomena, which are relevant for the simulation of atmospheres with **PHOENIX**. The newly EOS **SESAM** is based on the Villars-Cruise-Smith algorithm, applying the optimised stoichiometric method. The theoretical background of this approach is given in Chapter 3, whereas a detailed description of the code can be found in Chapter 4. Furthermore, Chapter 4 presents an overview about the **PHOENIX** framework and the modifications applied to provide a positive interplay between **PHOENIX** and the new EOS.

SESAM has been successfully added to **PHOENIX**. The corresponding tests considering the influence of the EOS on the atmospheric temperature and pressure structure and the spectrum of twelve different stars are presented in Chapter 5, sampling a wide stripe in the Hertzsprung-Russel diagram. In addition, the role of initially guessed species abundances is discussed and computational performance tests are presented. All tests have been also performed with **ACES**, which is the currently used EOS in **PHOENIX**, to provide a direct comparison of the two EOS's. The results are summarised in Chapter 6 along with an outlook regarding further tests, improvements, and applications of the new EOS.

Chapter 2

Theory: Stellar atmospheres

The stellar atmosphere forms the outermost region of a star. For the Sun, it can be divided into four layers: the innermost atmospheric shell is denoted as the photosphere, above which lies the chromosphere, followed by the transition region and the corona as the outermost layer. Although the radial extent of the photosphere is relatively small compared to the total stellar radius, almost all energy is emitted by it. Furthermore, it is the region where most spectral features emerge and it defines the overall shape of the spectrum.

Concerning the PHOENIX models computed for this thesis, this chapter and the discussion in Chapter 5 are concentrated on the photosphere. Therefore, whenever stellar atmosphere is mentioned in this thesis, it basically refers to the photosphere.

The theory of this chapter is based on Hubeny and Mihalas (2014), Hubeny (2013), Reid and Hawley (2005), Rutten (2003) and Mihalas (1970).

For the sake of clarity, the terms *particle* and *chemical species* simultaneously refer to atoms, molecules, and ions.

2.1 Overview

The density and pressure of the photosphere is mainly influenced by the surface gravity $g = GM/R^2$, with the gravitational constant G , the radius R , and the mass M of the star. A high gravity causes a higher absolute particle density gradient in the atmosphere, resulting in an increase of interactions. The respective spectrum will typically show broader spectral lines than a corresponding low-density atmosphere. Regarding super-giants, their lines are broader due to micro-turbulence.

Consistent with the Stefan-Boltzmann law, the effective temperature, T_{eff} , of a star is defined by the total flux that leaves the photosphere of the amount $F = \sigma T_{\text{eff}}^4$, with σ as Stefan-Boltzmann constant. Furthermore, radiation might not be the only effective energy transport mechanism in atmospheres. Convection can contribute to the total flux so that $F_{\text{rad}} + F_{\text{conv}} = \sigma T_{\text{eff}}^4$. Specifically, in environments with increasing opacity, the local radiative energy transport from the inner part of the atmosphere to the outer layers can become inefficient. In those dynamically unstable regions, large scale motions of stellar matter may arise and buoyancy forces cause displacements of the matter within the atmosphere. If these displacements act constructively to the surroundings, they can create a runaway effect with respect to the buoyant force, resulting in a convective flux. A

theoretical treatment of this chaotic process is complex and requires a lot of computational effort. In order to be able to compute the convective motions in a reasonable amount of time, model atmospheres often rely on simple approximations. Obviously, this cannot account for complex three-dimensional convective motions, but to consider convection in models, the mixing length theory (Böhm-Vitense, 1958; Böhm-Vitense and Nelson, 1976) was developed. It relates convection to rising and falling gas over a certain parametrised length. This mixing length is calibrated with solar observations and may not necessarily have the same value for other stars. This upwards and downwards travelling gas can be associated with mass elements, adiabatically moving, until they dissolve in the surrounding gas. The mass elements carry thermal energy, which is either in excess or deficiency of heat compared to the environment where they disintegrate. This way, the local energy can be increased or decreased. According to the Schwarzschild criterion, the ascending and descending movements become stable convective currents dominating the energy transport when

$$\left(\frac{d \ln T}{d \ln P}\right)_{\text{bg}} > \left(\frac{d \ln T}{d \ln P}\right)_{\text{ad}}, \quad (2.1)$$

namely when the temperature gradient of the radiative background (bg) is bigger than the adiabatic (ad) one in a certain depth.

In addition to radiation and convection, energy can be transported by heat conduction and mechanically by waves. However, these effects are only marginal for photospheres and occur predominantly in coronae and degenerate stellar interiors or, in the latter case, in coronae and chromospheres of cool stars.

The chemical composition plays a critical role for the properties of stellar atmospheres. It determines the opacity, influencing the energy transport at all scales and the spectroscopic features. These effects depend on the quantum mechanical interactions, which couple radiation to matter, the wavelength dependent cross sections of the species, and the number density of the species interacting with radiation. Although the number of absorbing atoms is associated with the strength of the absorption lines, it must not necessarily be the decisive factor. A further important contribution may arise from the individual absorption properties of the atom, i.e., their cross sections. Even low-abundant atoms may generate strong spectral features if the corresponding wavelengths are located in a range where the high-abundant atoms own only weak or no spectral lines. Analogously, the same consideration applies for emission.

The importance of molecules to the overall opacity grows with decreasing temperatures until they dominate the stellar spectra from effective temperatures below $T_{\text{eff}} = 3000$ K. Each molecule contains several nuclei of the constituent atoms. This causes a more complex system of excitation transitions than in a single atom because the molecules have additional vibrational and rotational excitation states. Therefore, one electronically excited state in a molecule creates thousands to millions of spectral lines. Like atoms, the chemical abundance of a molecule in an atmosphere does not have to entail its influence on the stellar spectrum. For instance, the diatomic molecules vanadium oxide and titanium oxide usually possess only low abundances in M- and L-dwarfs but may significantly contribute to the respective spectra due to their numerous strong transitions. This effect occurs because the constituent nuclei have quite different masses resulting in a tendency for stronger vibrational motions than in molecules consisting of similar nuclei masses.

Regarding the chemical abundances in atmospheres, an important quantity is the metallicity. It specifies the logarithmic abundance ratio of metals M and hydrogen H compared to the solar one:

$$\left[\frac{M}{H} \right] \equiv \log \left[\frac{M/H}{M_{\odot}/H_{\odot}} \right]. \quad (2.2)$$

Metals are referring in this context to all elements, except hydrogen and helium.

2.2 Radiative transfer

This section briefly introduces radiative transfer, which is the theory describing the transport of photons through matter and eventually allows for calculation of spectral properties of stellar atmospheres.

The specific intensity I_{λ} is defined as the energy that is transported by radiation through a surface dA into the solid angle $d\Omega$, in a certain wavelength interval $d\lambda$, depending on its location in space \mathbf{r} and on the propagation direction \mathbf{l} during a period of time dt :

$$dE_{\lambda} = I_{\lambda}(\mathbf{r}, \mathbf{l}, t) (\mathbf{l} \cdot \mathbf{n}) dA dt d\lambda d\Omega, \quad (2.3)$$

where the normal vector to the area dA is denoted as \mathbf{n} .

The average of the specific intensity over all directions is the mean intensity

$$J_{\lambda}(\mathbf{r}, t) = \frac{1}{4\pi} \oint I_{\lambda}(\mathbf{r}, \mathbf{l}, t) d\Omega. \quad (2.4)$$

The net rate of intensity, projected into the propagation direction \mathbf{l} , is the flux

$$\mathbf{F}_{\lambda}(\mathbf{r}, t) = \oint I_{\lambda}(\mathbf{r}, \mathbf{l}, t) \mathbf{l} d\Omega. \quad (2.5)$$

Physical processes in the gas may reduce the energy in the radiation beam: this property is called the opacity and is specified by the extinction coefficient χ_{λ} . Therefore, the energy removed from the beam is

$$dE_{\lambda}^{\text{rem}} = \chi_{\lambda}(\mathbf{r}, \mathbf{l}, t) I_{\lambda}(\mathbf{r}, \mathbf{l}, t) dA dt d\lambda d\Omega. \quad (2.6)$$

At the same time, energy can be added to the beam by emission, quantified by the emissivity η_{λ} , so that

$$dE_{\lambda}^{\text{add}} = \eta_{\lambda}(\mathbf{r}, \mathbf{l}, t) dA dt d\lambda d\Omega. \quad (2.7)$$

The energy removed from the beam and added to it sum up linearly:

$$dE_{\lambda} = dE_{\lambda}^{\text{rem}} + dE_{\lambda}^{\text{add}}. \quad (2.8)$$

The ratio of emissivity and extinction coefficient is called the source function

$$S_{\lambda} = \frac{\eta_{\lambda}}{\chi_{\lambda}}, \quad (2.9)$$

quantifying the energy loss or gain of the radiation in the beam.

The optical depth scale τ_λ specifies how strongly the light beam gets affected by extinction along a path length dz :

$$d\tau_\lambda = \chi_\lambda dz, \quad (2.10)$$

defined so that it increases from the outer atmosphere layers to the inner ones.

The radiative transfer equation is

$$\frac{dI_\lambda}{d\tau_\lambda} = I_\lambda - S_\lambda, \quad (2.11)$$

expressing the change of intensity along $d\tau_\lambda$.

Photons are removed from the beam by scattering and absorption. In particular in atmospheres where the gas is almost entirely or completely ionised, scattering between electrons and photons (Thomson scattering) increasingly affects the radiation. In cooler atmospheres, scattering of photons by atoms and molecules (Rayleigh scattering) plays an important role. Atoms, molecules, and ions can absorb photons of specific energies through electronic excitations. The electron is transferred from an orbital with a lower energy level to a higher one, with an energy shift identical to the photon's energy.

Assuming isotropy, the extinction coefficient is now

$$\chi_\lambda = \kappa_\lambda + \sigma_\lambda, \quad (2.12)$$

where κ_λ and σ_λ are the absorption and scattering terms, respectively.

Photons are added to the beam by scattering and emission. Emission occurs when an excited particle spontaneously or induced re-emits a photon or a cascade of photons while the electron goes from the excited energy level to a lower level. This spontaneous emission is a natural decay process and occurs independently of the presence or absence of a radiation field, but relies instead on the natural lifetime of the involved state. A stimulated emission of a photon is induced by an additional photon of the same energy that interacts with the excited atom, molecule, or ion.

Assuming isotropy, and taking both processes into account, the emissivity coefficient is

$$\eta_\lambda = \eta_\lambda^{\text{th}} + \sigma_\lambda J_\lambda, \quad (2.13)$$

including the thermal (th) emission and scattering into the beam.

The coefficients κ_λ and η_λ depend on the population density of the energy levels involved in the respective electron transitions. These densities are strongly correlated to the abundances of the chemical species present in the atmosphere. At the same time, a determination of χ_λ and η_λ requires the particle's ionisation and dissociation stages, their transition probabilities, their statistical weights and, in addition, the cross sections for the photons.

2.2.1 Energy level populations

Since a bound electron can occupy only discrete states, a detailed consideration of the occupation probabilities of the involved energy levels is essential in order to make quantitative assessments regarding the gas opacities.

Local thermodynamic equilibrium

For a transition from level i to a higher energy level j , the electron requires the excitation energy $\Phi_{ij} = hc/\lambda_{ij} = E_j - E_i$, with the Planck constant h and the velocity of light c . This is the energy difference between the respective states. Assuming local thermodynamic equilibrium (LTE), the population of the i^{th} energy level $n_{i,r}$, relative to the one of the j^{th} level $n_{j,r}$, is temperature dependent and is specified by the Boltzmann equation

$$\left[\frac{n_{i,r}}{n_{j,r}} \right]_{\text{LTE}} = \frac{g_{i,r}}{g_{j,r}} \exp\left(-\frac{\Phi_{ij}}{kT}\right), \quad (2.14)$$

considering a distribution in a specific r^{th} ionisation stage, with the statistical weights $g_{i,r}$ and $g_{j,r}$ describing the number of states having the energies E_i and E_j .

Summing Eq. 2.14 over all excitation levels leads to the population relative to the total number of atoms n_r ,

$$\left[\frac{n_{i,r}}{n_r} \right]_{\text{LTE}} = \frac{g_{i,r}}{Q_r(T)} \exp\left(-\frac{\Phi_{ij}}{kT}\right), \quad (2.15)$$

introducing the LTE partition function

$$Q_r(T) \equiv \sum_{i=0}^{\infty} g_{i,r} \exp\left(-\frac{\Phi_{ij}}{kT}\right). \quad (2.16)$$

Theoretically, $Q_r(T)$ is an infinite sum that diverges for an isolated atom but realistically an atom has only a finite number of orbitals occupied by electrons due to the atom's interaction with neighbouring particles.

The population ratio between the ground state, which is the 0^{th} energy level, of successive ionisation stages r and $r + 1$, is determined by the Saha equation

$$\left[\frac{n_{0,r+1}}{n_{0,r}} \right]_{\text{LTE}} = \frac{1}{n_e} \frac{2g_{0,r+1}}{g_{0,r}} \left(\frac{2\pi m_e kT}{h^2} \right)^{3/2} \exp\left(-\frac{\chi_r}{kT}\right), \quad (2.17)$$

by means of the electron density n_e , the statistical weights of the respective ionisation states $g_{0,r}$ and $g_{0,r+1}$, the electron mass m_e , and the ionisation energy χ_r , required to remove an electron from the ground state of the r^{th} ionisation stage to the continuum.

Or, analogously, summed over all energy levels,

$$\left[\frac{n_{r+1}}{n_r} \right]_{\text{LTE}} = \frac{1}{n_e} \frac{2Q_{r+1}(T)}{Q_r(T)} \left(\frac{2\pi m_e kT}{h^2} \right)^{3/2} \exp\left(-\frac{\chi_r}{kT}\right). \quad (2.18)$$

The gas particles follow a Maxwell-Boltzmann velocity distribution. Characteristic for LTE is that the level populations due to excitation and ionisation are fully described by the Boltzmann and Saha equations.

Non-local thermodynamic equilibrium

Most of the atmosphere of a cool main-sequence star can be approximated as LTE but there are always regions that are in distinctive non-local thermodynamic equilibrium (NLTE). Under many circumstances, the deviations from LTE apply to only a handful of

states of single gas species. For this reason, if the details are known, the situation can be treated as hybrid LTE-NLTE to save computing time with little to no loss in accuracy.

NLTE conditions may, though not imperatively, arise when atomic transitions due to radiative processes dominate over the collisional ones. However, an essential further prerequisite is the disequilibrium of the radiation so that the intensities are not represented by a Planck function corresponding to the same temperature as the local gas states. These situations emerge preferentially in atmospheric zones with a strong radiation field and low-density zones with notable temperature or density gradients.

Assuming a stationary ingoing and outgoing radiation field, rate equations must be solved, stating that the total number of transitions out of level i into other energy levels j is equal to the number of transitions of the reverse direction, namely the ones into the i^{th} energy level from other levels:

$$n_i \sum_{j \neq i} (R_{ij} + C_{ij}) = \sum_{j \neq i} n_j (R_{ji} + C_{ji}). \quad (2.19)$$

Therefore, the collisional rate coefficient C_{ij} and the radiative rate coefficient R_{ij} must be determined. These rate equations specify the level populations, which depend on the radiation field itself. This is in contrast to the LTE approximation where they depend only on the local gas temperature.

The deviation of the number of atoms in the i^{th} energy state in thermodynamic equilibrium, n_i^* , from the actual NLTE number of atoms, n_i , can be quantified by the departure coefficients

$$b_i \equiv \frac{n_i}{n_i^*}, \quad (2.20)$$

following Mihalas (1978). Under consideration of the r^{th} ionisation stage, and similar to LTE, the NLTE partition function is generalised as

$$Q_r(T) \equiv \sum_{i=0}^{\infty} b_{i,r} g_{i,r} \exp\left(-\frac{\Phi_{ij}}{kT}\right). \quad (2.21)$$

2.2.2 Solutions to the radiative transfer equation

If the radiation can be approximated by LTE without scattering, the source function S_λ is equal to a Planckian distribution function:

$$B_\lambda(T) \equiv \frac{2hc^2}{\lambda^5} \frac{1}{\exp(hc/\lambda kT) - 1}, \quad (2.22)$$

which specifies the radiation density of an object at thermal equilibrium at given temperature T , with the wavelength λ , the Boltzmann constant k , the Planck constant h , and the velocity of light c . Thus, the radiative transfer equation is a standard linear differential equation. Under this condition, matter and radiation are locally in equilibrium and Kirchhoff's law applies, stating that

$$\eta_\lambda^{\text{th}} = \kappa_\lambda B_\lambda(T). \quad (2.23)$$

Assuming additionally coherent scattering, S_λ is

$$S_\lambda = \frac{\kappa_\lambda}{\kappa_\lambda + \sigma_\lambda} B_\lambda(T) + \frac{\sigma_\lambda}{\kappa_\lambda + \sigma_\lambda} J_\lambda, \quad (2.24)$$

or by applying the parameter

$$\varepsilon_\lambda \equiv \frac{\kappa_\lambda}{\chi_\lambda} = \frac{\kappa_\lambda}{\kappa_\lambda + \sigma_\lambda}, \quad (2.25)$$

the source function is

$$S_\lambda = \varepsilon_\lambda B_\lambda(T) + (1 - \varepsilon_\lambda) J_\lambda. \quad (2.26)$$

The ε_λ is the thermal coupling parameter, associated with the probability of destruction of a photon by extinction compared to its probability of scattering.

Stellar atmospheres generally include non-coherent scattering and/or NLTE conditions. In this case, S_λ depends on the intensity and, therefore, Eq. 2.11 results in a non-linear differential equation. A formal solution of the radiative transfer equation must be found, required for iterative determination of the mean intensity J_λ . One approach to abbreviate this procedure is the Λ -operator with

$$J_\lambda = \Lambda S_\lambda. \quad (2.27)$$

However, in systems with a low destruction probability ε_λ and large optical depths, iteration methods like

$$J_{\lambda,\text{new}} = \Lambda S_{\lambda,\text{old}} \quad (2.28)$$

and

$$S_{\lambda,\text{new}} = \varepsilon_\lambda B_\lambda(T) + (1 - \varepsilon_\lambda) J_{\lambda,\text{new}} \quad (2.29)$$

require an exhaustive number of iterations, proportional to $1/\varepsilon_\lambda$, or do not numerically converge. In these environments, more complicated numerical methods must be applied. A possible solution is an operator splitting method where Λ is split along

$$\Lambda = \Lambda^* + (\Lambda - \Lambda^*), \quad (2.30)$$

with Λ^* as the approximate Λ -operator (Cannon, 1973). The resulting iterative equation,

$$J_{\lambda,\text{new}} = \Lambda^* S_{\lambda,\text{new}} + (\Lambda - \Lambda^*) S_{\lambda,\text{old}}, \quad (2.31)$$

provides the mean intensity by choosing a suitable Λ^* in a faster way than Eq. 2.28 (see, e.g. Hauschildt and Baron, 1999; Mihalas, 1970, and references therein).

Chapter 3

Theory: The chemical equilibrium

An equation of state sets thermodynamic parameters in a relation. These parameters can be, for instance, gas pressure, temperature, density or volume, and chemical composition. The ideal gas equation of state is presented in Sec. 3.1 along with a discussion on why the ideal gas law is valid in all stellar atmospheres that are considered in this thesis.

As shown in Chapter 2, the chemical abundances directly influence the energy level populations of atoms, molecules, and ions and, therefore, the opacity and emission in atmospheres. Thus, to simulate physical environments, the important chemical processes must be known. It is mandatory to assume that all chemical reactions lead to a well-defined equilibrium state as defined in Sec. 3.2. A fundamental quantity in this context is the chemical potential. It crucially influences the equilibrium composition and receives a more detailed consideration in Sec. 3.3.

The analytical equation of state, which relates the temperature, pressure and chemical composition in one equation, must be distinguished from the numerical one, hereafter referred to as its acronym: EOS. An EOS is an algorithm that is designed to numerically find solutions of the chemical equilibrium problem. In the context of this thesis, requirements like precision, calculation time and treatment of complex systems including several hundreds of chemical species and, to a limited degree, condensed species are important. A method that handles this well is the Villars-Cruise-Smith algorithm (Smith and Missen, 1982), based upon optimised stoichiometry. Its mathematical properties are described in Sec. 3.4. This method represents the basis of the new EOS module, which is included in the atmospheric model code PHOENIX as one goal of this thesis.

Unless stated otherwise, the theory detailed in Sec. 3.1 follows Mortimer and Müller (2014), Voigt (2012), Reid and Hawley (2005) and Schwarzschild (1958). Sections 3.2 - 3.4 are based on Smith and Missen (1982), Smith (1980), Wong et al. (2003), Smith and Missen (1979) and Sec. 3.3 in addition on Job and Herrmann (2006).

Frequently used terms in this chapter are chemical elements and species. A *chemical element* is a neutral atom with a unique number of protons. It can be transformed into another element only by nuclear reactions, which are ignored in this work. Similar to the previous chapter, *chemical species* and *particles* simultaneously refer to atoms, molecules and ions. *Free electrons* fulfil a special role in the EOS algorithm presented in this chapter: they are treated as both chemical element and species. The term *chemical abundance* refers to the amount of the species expressed in moles.

3.1 The equation of state

An equation of state connects the essential thermodynamic state variables, e.g., gas pressure P , density ρ or volume V , temperature T , and the chemical composition, which is here expressed by the number of moles n . This makes it an important tool for the description of the thermodynamical properties of a closed system. The simplest equation of state is based on the ideal gas law, assuming that there are no intermolecular forces between the species and the only interactions among themselves are collisional. In addition, the particles have an insignificant volume. It states

$$P_{\text{gas}} = \frac{R}{\bar{\mu}} \rho T = \frac{nRT}{V}, \quad (3.1)$$

with the ideal gas constant R , the gas pressure P_{gas} , and the mean molecular weight $\bar{\mu}$. However, depending on the gas temperatures and densities, radiative pressure P_{rad} and degeneracies may be important and contribute differently to the equation of state (Fig. 3.1). This eventually induces deviations between the total gas pressure P and the ideal gas pressure P_{gas} . Specifically the presence of intermolecular attraction forces is physically necessary in this regard because, otherwise, a gas could not liquefy. The higher the gas pressure, the spatially closer are the particles to one another, and the stronger are their interactions. Compared to the volume of an ideal gas, this causes a reduction of the volume

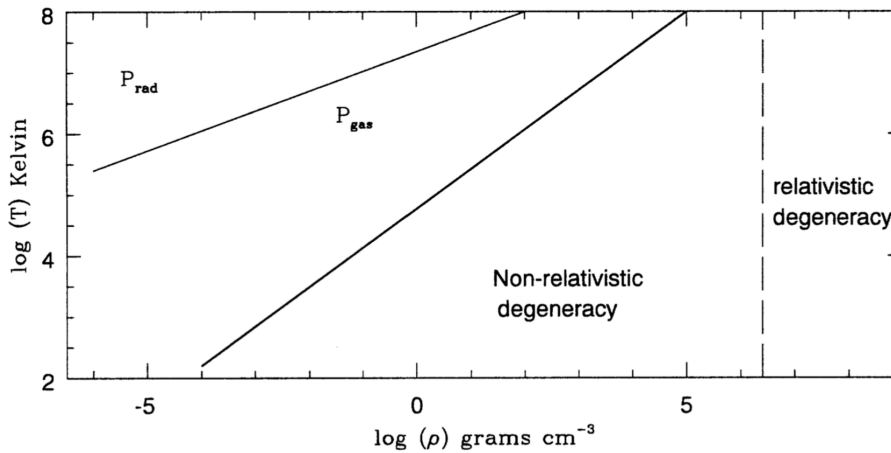


Figure 3.1: Main contributions to the equation of state by the radiation pressure P_{rad} , ideal gas pressure P_{gas} , and the degeneracy effects at different densities and temperatures (adapted from Reid and Hawley, 2005, and calculated by Schwarzschild, 1958). The lines between the different zones mark the conditions where the respective two contributors are equal. Their exact position is depending on the molecular weight and, therefore, on the composition. Here, pure hydrogen was used for the boundary between the P_{rad} and P_{gas} regimes and pure helium for the separation of the P_{gas} and degeneracy regimes.

occupied by them. Actually, and in contrast to the ideal gas law, each particle occupies a certain volume. For typical energies regarded in this work, species can be considered incompressible and the space between the particles is limited.

Regarding main-sequence stars, ranging from O-types with $T_{\text{eff}} \geq 30000$ K, to M-dwarfs with $T_{\text{eff}} \geq 2300$ K, their atmospheric densities are typically well below $\sim 10^{-5}$ g cm $^{-3}$. The atmospheres of these stellar objects are in the gas pressure (P_{gas}) dominated zone of Fig. 3.1 and, therefore, their total pressure can be described by an ideal gas law (Eq. 3.1). Van der Waals and other forces affect the gas in stellar atmospheres marginally since most molecules are simply far too rare to significantly disturb the equation of state directly. The possibly abundant molecular hydrogen (H_2) is extremely small, light and fast for typical stellar atmosphere temperatures being, therefore, only weakly affected by intermolecular forces.

The situation is different in environments with high densities, e.g., in stellar interiors. Since electrons are fermions, they obey the Pauli exclusion principle, which states that no quantum state can be occupied by more than one fermion. As a result, a quantum mechanical degeneracy takes place and becomes increasingly prevailing for higher densities. These extreme densities occur significantly in the inner parts of certain red giants and in almost all parts of cooled white dwarfs, and the ideal gas equation of state is far from valid there.

In addition, for low densities and very high temperatures, the interaction of the photon's momentum with matter gains importance. The pressure exerted by photons, i.e., radiation pressure contributes significantly to the total gas pressure and adjustments must thus be done for calculating P . This can be realised by simply summing up the ideal gas pressure and the radiative pressure. With increasing temperatures, the radiative pressure becomes a growing contribution to the total pressure, but only the outer layers of the heaviest non-degenerated stars can exceed temperatures where P_{rad} dominates over P_{gas} (e.g. Carroll and Ostlie, 2007).

There is still no single equation of state, which is simultaneously valid under all conditions. Nevertheless, the ideal gas law is a reasonable assumption for stellar photospheres of main-sequence stars.

3.2 The chemical equilibrium as a minimisation problem

In a closed thermodynamic system, the equilibrium state will eventually be reached including thermodynamic and phase equilibrium. In addition, a statistical chemical equilibrium is attained when there is no longer a macroscopic change in composition. This does not mean that there are no microscopic reactions occurring between the species. On the contrary, chemical reactions are still continuously taking place but with equal rates for their forward and reverse reactions. This is the principle of detailed balance.

To determine this chemical equilibrium state, the defining parameters of the system such as, for instance, the gas pressure and the gas temperature, have to be specified. The respective thermodynamic properties can be provided by a suitable equation of state. In the following, a system in a locally stable equilibrium state is assumed, which contains a number of chemical species N and a number of elements M , without any mass exchange

with the surroundings. Conservation of mass must, therefore, be fulfilled at all times. This can be expressed by a set of atom-balance equations as formulated by the following relation between the fixed number of moles b_k of the element k , and the number of moles of the i^{th} species n_i :

$$\sum_{i=1}^N a_{ki} n_i = b_k \quad \text{with} \quad k \in \{1, 2, \dots, M\}, \quad (3.2)$$

defining a_{ki} as the index of the element k in the molecular formula of the i^{th} species. Or, in vector-matrix-notation:

$$\mathbf{A}\mathbf{n} = \mathbf{b}, \quad (3.3)$$

with $\mathbf{A} = (\mathbf{a}_1, \mathbf{a}_2, \dots, \mathbf{a}_N)$ as a $(M \times N)$ formula matrix, which is composed of N formula vectors \mathbf{a}_i . The species abundance vector is represented by $\mathbf{n} = (n_1, n_2, \dots, n_N)^T$, with $n_i \geq 0$, and the element abundance vector by $\mathbf{b} = (b_1, b_2, \dots, b_M)^T$.

The physically crucial criterion

$$n_i \geq 0 \quad \forall i \in \{1, 2, \dots, N\}, \quad (3.4)$$

is called the non-negativity constraint and means that a species can either be present or not, but its abundance can never be negative.

In a closed system, a change in the element abundances is impossible and, therefore, changes in the moles between two compositional states of the system, $\delta n = n^{(2)} - n^{(1)}$, must satisfy

$$\sum_{i=1}^N a_{ki} \delta n_i = 0 \quad \text{with} \quad k \in \{1, 2, \dots, M\}, \quad (3.5)$$

or, analogously in vector-matrix notation,

$$\mathbf{A}\delta\mathbf{n} = 0. \quad (3.6)$$

The second law of thermodynamics, which defines the direction of processes (e.g. Clausius, 1856), allows to connect chemical equilibria conditions with potential functions. For example, in an adiabatic system in an equilibrium state, the entropy S cannot decrease,

$$dS_{\text{ad}} \geq 0, \quad (3.7)$$

and the Gibbs function G cannot increase in systems with fixed temperatures und pressures,

$$dG_{T,P} \leq 0. \quad (3.8)$$

In other words, G has its (global) minimum for systems in chemical equilibrium. The 'd' stands for an total differential of the potential functions.

G is a function of temperature, pressure and mole numbers of involved species with

$$dG = -SdT + VdP + \sum_{i=1}^N \mu_i dn_i, \quad (3.9)$$

with V as the system's volume and μ_i is the chemical potential of the i^{th} species.

Consequently, in an equilibrium system with fixed T and P , the differential of Gibbs

function is

$$dG = \sum_{i=1}^N \mu_i dn_i \quad (3.10)$$

and the corresponding chemical potential can be defined by

$$\mu_i = \left(\frac{\partial G}{\partial n_i} \right)_{T, P, n_j \neq i} . \quad (3.11)$$

Similarly to the minimisation of G , the equilibrium state can be determined with a minimisation of other potential functions like, e.g., the minimisations of the Helmholtz function A (for fixed T and V), the enthalpy H (for fixed P and S), or the internal energy U (for fixed V and S). Alternatively, in an isolated system, the equilibrium state can be found by maximising the entropy for a given internal energy U .

3.3 The chemical potential

The chemical potential μ plays a crucial role in the description of chemical and physical properties of the species, since it is a fundamental quantity in identifying the equilibrium composition. It characterises the tendency of a species to pursue a change of composition and aggregate state. An equilibrium state is reached if the total μ of the product species is equal to the total μ of the reactants.

Since only the differences in the chemical potentials can be measured, the values of μ are fixed on an arbitrarily scale to describe chemical reactions. Species with higher chemical potentials will more likely react than the species with lower ones. The lower the μ of the species, the more stable is its state and it will not spontaneously disintegrate into its chemical elements. Nevertheless, this process does not only depend on the value of μ : in addition, species have a specific resistance towards reactions, which is highly dependent on the temperature. With increasing temperatures, the reaction resistance decreases and the possibility for the reactions to take place grows. Although the chemical potentials are also temperature dependent in a way that, for a classical ideal gas, a gain in T reduces μ , the effect of the resistance has a stronger impact. Another influence on μ is given by the pressure, insofar that a higher pressure leads to an increase in the chemical potential.

Regarding a pure species system with fixed temperatures and a change in pressure, the partial change of μ is equal to the molar volume $v = (\partial V / \partial n)_{T, P}$:

$$\left(\frac{\partial \mu}{\partial P} \right)_T = v. \quad (3.12)$$

An integration with respect to the pressure results in

$$\mu(T, P) - \mu(T, P^0) = \int_{P^0}^P v \, dP, \quad (3.13)$$

with P^0 as the reference pressure of 1 bar for gases and of the vapour pressure for pure liquids or solids. This equation is valid for any pure system, even for non-ideal gases and condensed species. Assuming now an ideal system by applying the ideal equation of state,

$v = RT/P$, and rephrasing $\mu(T, P^0)$ as the standard chemical potential at its reference pressure $\mu^0(T)$, Eq. 3.13 becomes

$$\mu(T, P) = \mu^0(T) + RT \ln P. \quad (3.14)$$

A solution of ideal gases follows Amagat's law, stating that at fixed T and P , the sum of the volumes of the respective mixed gases are equal to the total volume of the gas. In this case, the chemical potential of the i^{th} species is

$$\mu_i(T, P, x_i) = \mu_i^0(T) + RT \ln p_i. \quad (3.15)$$

The composition dependence is added by means of the partial pressures p_i , defined as

$$p_i = \left(\frac{n_i}{n_t} \right) P \equiv x_i P, \quad (3.16)$$

with n_i as the number of moles of the considered species, n_t as the total moles in the system and x_i as the mole fractions. Now, Eq. 3.15 becomes

$$\mu_i(T, P, x_i) = \mu_i^0(T) + RT \ln P + RT \ln x_i, \quad (3.17)$$

and by setting

$$\mu_i^* \equiv \mu_i^0(T) + RT \ln P, \quad (3.18)$$

the chemical potential for an ideal solution is in its final form:

$$\mu_i = \mu_i^*(T, P) + RT \ln \left(\frac{n_i}{n_t} \right). \quad (3.19)$$

It shows that, next to its temperature and pressure dependence, a greater mole fraction of the i^{th} species increases the chemical potential. Furthermore, the species will more likely react since μ can be regarded as the driving force that influences the species amounts.

3.4 The approach of optimised stoichiometry

As shown in Sec. 3.2, the chemical equilibrium can be obtained by treating it as a minimisation problem of a potential function. By means of a stoichiometric approach, the element abundance constraints are always fulfilled.

The N total species in the system can be grouped in C component and R non-component species with

$$R = N - C, \quad (3.20)$$

so that the non-component species are build with help of the component species in the resulting chemical equations. Each non-component species requires an own chemical equation. Their number R can be related to the stoichiometric degree of freedom and, therefore, to the number of linearly independent chemical equations of the system. The number of component species C is equal to the rank of the formula matrix,

$$C = \text{rank}(\mathbf{A}) \leq M. \quad (3.21)$$

To find a solution of the element abundance equations 3.2 or 3.3 with the stoichiometric approach, the stoichiometric coefficient vectors $\boldsymbol{\nu}_j$, with $\boldsymbol{\nu}_j \neq \mathbf{0}$, are introduced and must satisfy

$$\mathbf{A}\boldsymbol{\nu}_j = \mathbf{0} \quad \text{with} \quad j \in \{1, 2, \dots, R\}. \quad (3.22)$$

Replacing the formula matrix \mathbf{A} with the respective species names A_i and the stoichiometric vector with its stoichiometric coefficient ν_{ij} of species i and element j , this becomes in scalar-notation

$$\sum_{i=1}^N A_i \nu_{ij} = 0 \quad \text{with} \quad j \in \{1, 2, \dots, R\}, \quad (3.23)$$

and represents a complete set of stoichiometric equations. By means of a set of arbitrary real numbers ξ_j , any possible solution of the element abundance equations 3.2 and 3.3 is

$$\mathbf{n} = \mathbf{n}^0 + \sum_{j=1}^R \boldsymbol{\nu}_j \xi_j, \quad (3.24)$$

or, respectively,

$$n_i = n_i^0 + \sum_{j=1}^R \nu_{ij} \xi_j \quad \text{with} \quad i \in \{1, 2, \dots, N\}. \quad (3.25)$$

Here, \mathbf{n}^0 and n_i^0 are any particular solution of Eq. 3.24 like, for instance, an initial composition of the chemical system. If n_i^0 is fixed, the stoichiometric coefficient ν_{ij} can be written as

$$\left(\frac{\partial n_i}{\partial \xi_j} \right)_{\xi_{k \neq j}} = \nu_{ij} \quad \text{with} \quad j \in \{1, 2, \dots, R\} \text{ and } i \in \{1, 2, \dots, N\}. \quad (3.26)$$

De Donder and Van Rysselberghe (1936) assign the real parameter ξ as the degree of advancement of the system. It can be regarded as the reaction-extent variable.

Since the stoichiometric coefficient vectors $\boldsymbol{\nu}_j$ are defined according to Eq. 3.22, a multiplication of Eq. 3.24 with the formula matrix \mathbf{A} shows that the result is equal to the element abundance vector \mathbf{b} :

$$\mathbf{A}\mathbf{n} = \mathbf{A}\mathbf{n}^0 + \sum_{j=1}^R \xi_j \mathbf{A}\boldsymbol{\nu}_j = \mathbf{b}. \quad (3.27)$$

Thus, Eq. 3.24 satisfies the requirement of mass conservation in a closed system.

All stoichiometric coefficient vectors can be written in a $(N \times R)$ complete stoichiometric coefficient matrix,

$$\mathbf{N} = (\boldsymbol{\nu}_1, \boldsymbol{\nu}_2, \dots, \boldsymbol{\nu}_R), \quad (3.28)$$

and Eq. 3.22 can consequently be rewritten as

$$\mathbf{A}\mathbf{N} = \mathbf{0}. \quad (3.29)$$

With the help of elementary row operations it is possible to form a unit matrix \mathbf{A}^* from the formula matrix \mathbf{A} :

$$\mathbf{A}^* = \begin{pmatrix} \mathbf{I}_C & \mathbf{Z} \end{pmatrix}. \quad (3.30)$$

The left part \mathbf{I}_C is assigned as a $(C \times C)$ unit matrix and the right part as a $(C \times R)$ sub-matrix \mathbf{Z} . Using \mathbf{Z} and a $(R \times R)$ unit matrix \mathbf{I}_R , the complete stoichiometric coefficient matrix for \mathbf{A}^* is

$$\mathbf{N} = \begin{pmatrix} -\mathbf{Z} \\ \mathbf{I}_R \end{pmatrix}. \quad (3.31)$$

Applying this procedure, \mathbf{Z} fulfils

$$\mathbf{A}_C \mathbf{Z} = \mathbf{A}_R, \quad (3.32)$$

with \mathbf{A}_C as the set of component species and \mathbf{A}_R as the set of non-component species of the system. From this, \mathbf{Z} can be written as

$$\mathbf{Z} = \mathbf{A}_C^{-1} \mathbf{A}_R \quad (3.33)$$

and Eq. 3.29 results in

$$\mathbf{A} \mathbf{N} = (\mathbf{A}_C, \mathbf{A}_R) \begin{pmatrix} -\mathbf{A}_C^{-1} \mathbf{A}_R \\ \mathbf{I}_R \end{pmatrix} = -\mathbf{A}_R + \mathbf{A}_R = \mathbf{0}. \quad (3.34)$$

The stoichiometric procedure is independent of the system's state. A criterion for an existing chemical equilibrium state can be linked to the procedure by minimising the Gibbs function G (Sec. 3.2).

G is a function of the temperature, pressure, and the chemical composition. Since the composition can be expressed by Eq. 3.25 in the stoichiometric formulation, the following equation is therefore a prerequisite for a minimum of the Gibbs function in systems with fixed temperatures and pressures:

$$\left(\frac{\partial G}{\partial \xi_j} \right)_{T,P,\xi_{i \neq j}} = \sum_{i=1}^N \left(\frac{\partial G}{\partial n_i} \right)_{T,P,n_{j \neq i}} \left(\frac{\partial n_i}{\partial \xi_j} \right)_{\xi_{i \neq j}} = 0 \quad \text{with} \quad j \in \{1, 2, \dots, R\}. \quad (3.35)$$

This is, in consistence with Eqs. 3.11 and 3.26, equal to

$$\sum_{i=1}^N \nu_{ij} \mu_i = 0 \quad \text{with} \quad j \in \{1, 2, \dots, R\}, \quad (3.36)$$

and states the equilibrium conditions. Thus, next to the stoichiometric coefficients ν_{ij} , the choice of a proper chemical potential of each i^{th} species μ_i has a crucial influence on the resulting equilibrium composition.

Alternatively to Eqs. 3.35 and 3.36, the equilibrium conditions are rewritable as

$$\Delta \mathbf{G} \equiv \left(\frac{\partial G}{\partial \xi} \right)_{T,P} = \mathbf{N}^T \boldsymbol{\mu}(\boldsymbol{\xi}) = \mathbf{0}. \quad (3.37)$$

This non-linear equation can be solved by a first-order optimisation method by modifying the reaction-extent variable ξ at each iteration step (m),

$$\delta \xi_j^{(m)} = - \left(\frac{\partial G}{\partial \xi_j} \right)^{(m)} = -\Delta G_j^{(m)} = - \sum_{i=1}^N \nu_{ij} \mu_i^{(m)} \quad \text{with} \quad j \in \{1, 2, \dots, R\}, \quad (3.38)$$

as suggested by Naphtali (1959). Since first-order methods converge rather slowly (e.g. Boyd and Vandenberghe, 2004), a solution of Eq. 3.37 can be found more advantageously by means of a second-order method like the Newton-Raphson method,

$$\delta\xi^{(m)} = - \left(\frac{\partial^2 G}{\partial \xi^2} \right)_{n^{(m)}}^{-1} \left(\frac{\partial G}{\partial \xi} \right)_{n^{(m)}}, \quad (3.39)$$

as proposed by, e.g., Stone (1966). Further improvement has been done by Smith and Missen (1982) who developed the Villars-Cruise-Smith (VCS) algorithm, an optimised stoichiometric approach. In the VCS algorithm, the stoichiometric matrix \mathbf{N} is constructed in a way that the Hessian matrix $\partial^2 G / \partial \xi^2$ can be easily inverted by assuming its diagonality. This is possible because \mathbf{N} can be chosen arbitrarily. With the Kronecker delta δ_{kl} and the total number of moles n_t , the Hessian matrix for an ideal system in a single phase is

$$\frac{\partial^2 G}{\partial \xi_i \partial \xi_j} = \frac{\partial}{\partial \xi_j} \left(\sum_{k=1}^N \nu_{ki} \mu_k \right) = RT \sum_{k=1}^N \sum_{l=1}^N \nu_{ki} \nu_{lj} \left(\frac{\delta_{kl}}{n_k} - \frac{1}{n_t} \right) \quad \text{with } i, j \in \{1, 2, \dots, R\}. \quad (3.40)$$

Using

$$\bar{\nu}_i = \sum_{k=1}^N \nu_{ki}, \quad (3.41)$$

Eq. 3.40 can be written as

$$\frac{1}{RT} \frac{\partial^2 G}{\partial \xi_i \partial \xi_j} = \sum_{k=1}^N \frac{\nu_{ki} \nu_{kj}}{n_k} - \frac{\bar{\nu}_i \bar{\nu}_j}{n_t} \quad \text{with } i, j \in \{1, 2, \dots, R\}. \quad (3.42)$$

As reminder, the C component species are forming the R non-component species in chemical equations. Each non-component species has one stoichiometric vector $\boldsymbol{\nu}$ where its stoichiometric coefficient is non-zero. Assuming a canonical stoichiometric matrix and species k to be a non-component, this leads to a product of the stoichiometric coefficients $\nu_{ki} \nu_{kj} = 1$, if the i^{th} species is equal to the j^{th} species, otherwise the product is zero. Choosing the indices for the component species from 1 to M , and for the non-component species from $(M + 1)$ to N , Eq. 3.42 can be written as

$$\frac{1}{RT} \frac{\partial^2 G}{\partial \xi_i \partial \xi_j} = \frac{\delta_{ij}}{n_{j+M}} + \sum_{k=1}^M \frac{\nu_{ki} \nu_{kj}}{n_k} - \frac{\bar{\nu}_i \bar{\nu}_j}{n_t} \quad \text{with } i, j \in \{1, 2, \dots, R\}. \quad (3.43)$$

If the stoichiometric matrix is constructed in a way that the most abundant species in the system are the component species, this will result in

$$\sum_{k=1}^M \frac{\nu_{ki} \nu_{kj}}{n_k} - \frac{\bar{\nu}_i \bar{\nu}_j}{n_t} \ll \frac{\delta_{ij}}{n_{j+M}}, \quad (3.44)$$

because the n_k and n_t are larger than the n_{j+M} . Hence, the diagonality of the Hessian matrix can be assumed and it can be easily inverted, becoming

$$RT \left(\frac{\partial^2 G}{\partial \xi_i \partial \xi_j} \right)^{-1} \approx \left(\frac{1}{n_{i+M}} + \sum_{k=1}^M \frac{\nu_{ki}^2}{n_k} - \frac{\bar{\nu}_i^2}{n_t} \right)^{-1} \delta_{ij}. \quad (3.45)$$

By means of Eqs. 3.39 and 3.45, the non-linear equation 3.37 can be solved in the VCS algorithm with the corrections to the reaction-extent variables:

$$\delta\xi_j^{(m)} = - \left(\frac{1}{n_{j+M}^{(m)}} + \sum_{k=1}^M \frac{\nu_{kj}^2}{n_k^{(m)}} - \frac{\bar{\nu}_j^2}{n_t} \right)^{-1} \frac{\Delta G_j^{(m)}}{RT} \quad \text{with } j \in \{1, 2, \dots, R\}. \quad (3.46)$$

For the VCS procedure it is, therefore, crucial that the species with the largest mole numbers are selected to be the component species.

Adjusting Eq. 3.46 to systems with π_m multi-species phases α , the reaction-extent variables are modified by

$$\delta\xi_j^{(m)} = - \left(\frac{\delta_{j+M,\alpha}^*}{n_{j+M}^{(m)}} + \sum_{k=1}^M \frac{\nu_{kj}^2 \delta_{k\alpha}^*}{n_k^{(m)}} - \sum_{\alpha=1}^{\pi_m} \sum_{k=1}^N \frac{(\nu_{kj} \delta_{k\alpha})^2}{n_{t\alpha}} \right)^{-1} \frac{\Delta G_j^{(m)}}{RT} \quad (3.47)$$

at the m^{th} iteration step. Here, $\delta_{k\alpha}$ is the Kronecker delta and is 1 if the k^{th} species is in the specific phase α and, similar to this, $\delta_{k\alpha}^*$ is 1 if the k^{th} species exists in at least one of the phases α .

Finally, with Eq. 3.47 and the complete stoichiometric coefficient matrix, the iterative changes to the species abundances can be obtained using

$$\delta\mathbf{n} = \mathbf{N}\delta\xi. \quad (3.48)$$

Chapter 4

Methods: The atmosphere model code and its new EOS module

The main part of this thesis was to include the new EOS module named **SESAM** (Stoichiometric Equilibrium Solver for Atoms and Molecules) in the general-purpose atmosphere model code **PHOENIX** (Hauschildt, 1992, 1993). The EOS is based on the optimised stoichiometry method (Sec. 3.4) and reliably determines accurate chemical equilibrium compositions (Meyer, 2013). Next to gaseous species, it can take into account condensed species by treating them as single species phases. In addition, an initial estimate had been implemented to minimise the required number of iterations until the chemical equilibrium problem is solved. A more detailed description of the code is given in Sec. 4.1. **SESAM** can be used stand-alone while it is far more useful if implemented as a detailed EOS in larger codes: from hydrodynamic codes that require the chemical compositions for systems located within a finite volume with adiabatic boundaries, to environments where the chemical systems proceed much faster than the changes in temperatures and pressures allowing densities and internal energies to evolve. Whenever **PHOENIX** uses the approximation of a static atmosphere, it specifically demands the EOS for the latter case. Section 4.2 provides an overview of the basic features of the atmosphere model code and shows the role of the EOS in its simulations.

For **SESAM**'s inclusion in **PHOENIX**, particular modifications were necessary, which are described in Sec. 4.3.

4.1 The new EOS module **SESAM**

In **SESAM**, the chemical equilibrium problem is treated by the minimisation of the Gibbs energy G (Sec. 3.2), applying the optimised stoichiometry method as described in Sec. 3.4. An earlier version of **SESAM** was extensively evaluated and tested in Meyer (2013) where it was denoted as **StoiCES**. Validations were performed by comparing results with published data and the NASA Glenn computer program **CEA** (Gordon and McBride, 1994; McBride and Gordon, 1996). It was shown that equilibrium compositions of complex systems that contain several hundreds of gaseous species are successfully reproduced, including the abundances of very small trace species at temperatures of few hundred Kelvin. This is true for the application of the thermodynamic state constraint of constant (T, P) and constant (U, V) . The CPU times required for solving the equilibrium problem was considerably

improved by implementing a numerical estimate of initial species abundances.

For the inclusion in PHOENIX, SESAM only applies the thermodynamic state constraint of constant (T, P) . The features of it are described in Sec. 4.1.1 and build up on the basic considerations in Sec. 3.4. After Meyer (2013), SESAM has been further developed to take condensed species and ions into account. The respective code modifications are presented in Sec. 4.1.2. SESAM's impeccable convergence behaviour is shown in Sec. 4.1.3.

4.1.1 Iterative method: Constraints of constant (T, P)

To calculate the equilibrium composition of a gaseous system using the constraint of constant temperature and pressure, SESAM follows the iterative scheme depicted in Fig. 4.1. As input, the gas temperature T and gas pressure P of the environment are required. In addition, the involved species and elements must be specified for the later construction of the formula matrix. The moles or relative abundances of the elements are completing the input data.

Read-in of thermodynamic data

Based on the selection of the required elements and species, SESAM reads in the thermodynamic data. As initial configuration, this data is taken from the thermodynamic library of the NASA Glenn computer program CEA. Their origin is predominantly the NIST-JANAF Thermochemical Tables (Chase, 1998) from which Bonnie J. McBride and Sanford Gordon made curve fits for chemical species, based on measured properties and estimates. A detailed description of the data sources and their format can be found in, e.g., McBride et al. (2002). For the computation of the chemical potentials of the individual species i , SESAM requires initially the enthalpies $H_i^0(T)/RT$ and entropies $S_i^0(T)/R$ for the requested temperature. The superscript 0 indicates the reference state 298.15 K and 1 bar. These properties are stored in the CEA library in the form of least-squares coefficients a_1 to a_7 and integration constants b_1 and b_2 and can be accessed by applying the following equations:

$$\frac{H^0(T)}{RT} = -a_1 T^{-2} + a_2 \frac{\ln T}{T} + a_3 + a_4 \frac{T}{2} + a_5 \frac{T^2}{3} + a_6 \frac{T^3}{4} + a_7 \frac{T^4}{5} + \frac{b_1}{T} \quad (4.1)$$

$$\frac{S^0(T)}{R} = -a_1 \frac{T^{-2}}{2} - a_2 T^{-1} + a_3 \ln T + a_4 T + a_5 \frac{T^2}{2} + a_6 \frac{T^3}{3} + a_7 \frac{T^4}{4} + b_2. \quad (4.2)$$

Using the list of the required species, SESAM creates the formula vectors \mathbf{a}_i and constructs the formula matrix \mathbf{A} . Now, the standard chemical potentials μ_i^0 are calculated by means of the standard enthalpies and entropies data of all species:

$$\frac{\mu_i^0}{RT} = \frac{H_i^0}{RT} - \frac{S_i^0}{R} \quad \text{with} \quad i \in \{1, 2, \dots, N\}. \quad (4.3)$$

Set-up of the equilibrium problem

The next step is to separate the species in the formula matrix \mathbf{A} into a set of components \mathbf{A}_C and non-components \mathbf{A}_R . Their total numbers C and R are determined according to Eqs. 3.21 and 3.20. As mentioned in Sec. 3.4, the species with the highest moles should be

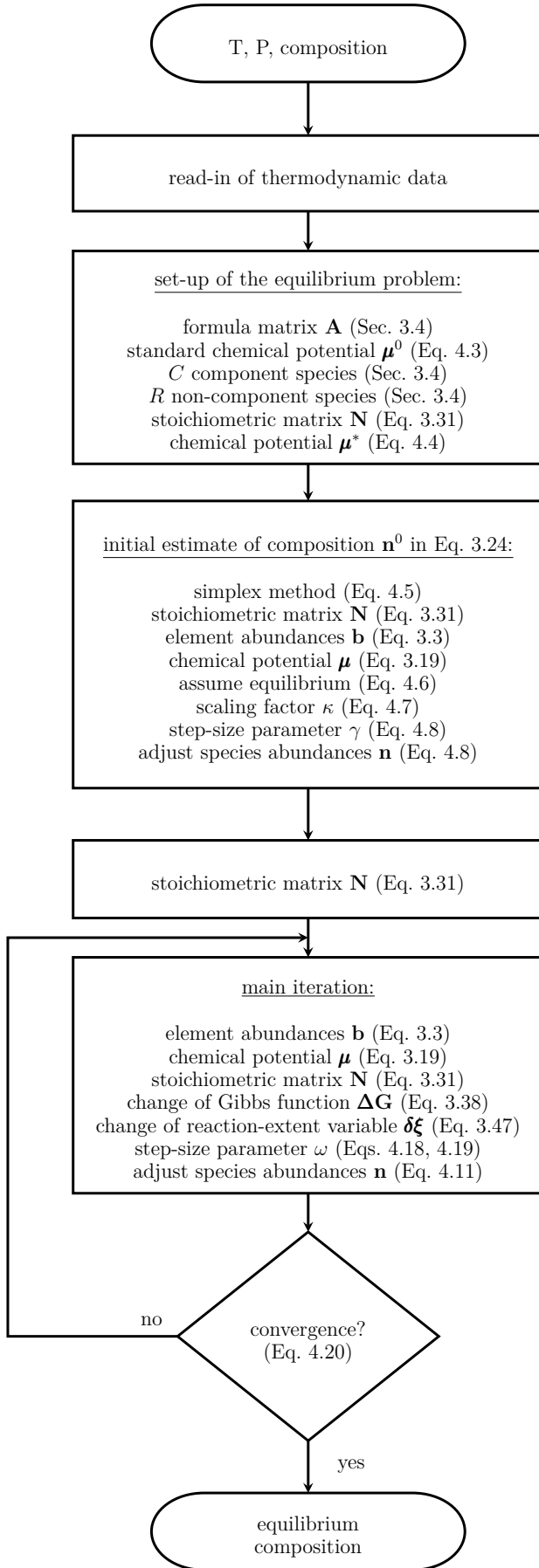


Figure 4.1: The basic method of SESAM to calculate the equilibrium composition using the constraints of constant temperatures and pressures. A detailed description of the code and the quantities listed is presented in Sec. 4.1.1.

selected as component species in order to ensure the diagonality of the Hessian matrix, which will be constructed later in the iterative process. It is important to check the linear independence of these component species to ensure that the non-components can be constructed from them in the resulting chemical equations. If this is not the case, a new selection of component species is chosen until linear independence is achieved. This check is realised by the orthogonalisation method provided by the Gram-Schmidt process. Applying Eq. 3.33 on \mathbf{A}_C and \mathbf{A}_R , the sub-matrix \mathbf{Z} is determined. The building of the stoichiometric matrix \mathbf{N} follows including its stoichiometric vectors $\nu_1, \nu_2, \dots, \nu_R$ from Eq. 3.31. Afterwards, the pressure-dependent part of the chemical potential is individually calculated for each species by applying

$$\frac{\mu_i^*}{RT} = \frac{\mu_i^0}{RT} + \ln P \quad \text{with} \quad i \in \{1, 2, \dots, N\}. \quad (4.4)$$

Initial estimate of the chemical composition

To accelerate the computation, a simplex method (Press, 1992) is implemented to provide an initial estimate for the equilibrium composition \mathbf{n}^0 in Eq. 3.24. It consistently solves the following linear problem,

$$\min_{\boldsymbol{\mu}^* \in \mathbb{R}^n} \{ \mathbf{n}^T \boldsymbol{\mu}^* \mid \mathbf{A}\mathbf{n} = \mathbf{b}, n_i \geq 0 \}, \quad (4.5)$$

with the conservation of mass and the non-negativity constraint. Here, \mathbf{n}^T refers to the transposed of the species abundance vector and $\boldsymbol{\mu}^*$ to the standard chemical potential vector without contribution from the partial pressures (Eq. 4.4). Using the resulting new abundances, the species are separated in linearly independent components and non-components, the stoichiometric matrix \mathbf{N} is recreated (Eq. 3.31) and the element abundances \mathbf{b} are calculated (Eq. 3.3). In addition, the chemical potentials are updated with the partial pressures of the species (Eq. 3.19). Following Smith and Missen (1968), SESAM assumes that the chemical reactions, which are composed of the R non-component species, obtained equilibrium. In order to accomplish this, the respective ΔG_j are set to zero and the abundances of the remaining components are kept constant. From Eqs. 3.19 and 3.38 it follows that the abundances of the non-components are

$$n_j = n_t \exp \left(-\mu_j^* - \sum_{k=1}^M \nu_{kj} \mu_k \right) = \xi_j \quad \text{with} \quad j \in \{1, 2, \dots, R\}, \quad (4.6)$$

which are consistent with the extents of reaction-extent variables ξ_j . The n_t are the total number of moles. To ensure that the non-negativity constraint is always fulfilled, a scaling factor κ is applied so that the n_i are always positive. Thereby, the correction-vector of the species abundances $\boldsymbol{\delta}\mathbf{n}$ is modified to

$$\boldsymbol{\delta}\mathbf{n} = \kappa \mathbf{N}\boldsymbol{\xi} \quad \text{with} \quad 0 < \kappa \leq 1. \quad (4.7)$$

The parameter κ is very similar to the one of the main iteration (cf. Eqs. 4.13 and 4.14) and determined in the same way. Next step is to adjust the previously estimated species abundances \mathbf{n}^0 in order to approximately minimise the Gibbs function. This is done by

means of a step-size parameter γ ,

$$\mathbf{n} = \mathbf{n}^0 + \gamma \boldsymbol{\delta n} \quad \text{with} \quad 0 < \gamma \leq 1, \quad (4.8)$$

and its most appropriate value is the one that minimises G in

$$\left(\frac{dG}{d\gamma} \right) = \boldsymbol{\mu}^T \boldsymbol{\delta n}, \quad (4.9)$$

assuming G is locally a parabolic function of γ . To find the best γ , Eq. 4.9 is evaluated at $\gamma = 1$. A result less or equal 0 indicates that the minimising γ is found and the full correction can be applied in Eq. 4.8. Otherwise, Eq. 4.9 is recalculated using $\gamma = 0.5$ in Eq. 4.8, and the updated chemical potentials (Eq. 3.19). Now, three different cases are distinguished:

- (1) $(dG/d\gamma)|_{\gamma=0.5} > 0$,
- (2) $(dG/d\gamma)|_{\gamma=0.5} = 0$, and
- (3) $(dG/d\gamma)|_{\gamma=0.5} < 0$.

The most suitable γ is found in case (1) and will be applied. If case (2) occurs, the final γ is set to 0.2 and case (3) implies the calculation of a new parameter β :

$$\beta = 0.5 \left(\frac{1 - (dG/d\gamma)_{\gamma=0.5}}{(dG/d\gamma)_{\gamma=1} - (dG/d\gamma)_{\gamma=0.5}} \right). \quad (4.10)$$

A $\beta \leq 1$ leads to a $\gamma = \beta$ and a $\beta > 1$ to $\gamma = 1$ as the preferable values. After finding the suitable γ , the species abundances \mathbf{n} are calculated with Eq. 4.8 and the initial estimate procedure is terminated.

Stoichiometric matrix and main iteration

Based on the estimated initial species abundances, the stoichiometric matrix is rebuilt and the element abundance vector \mathbf{b} is determined conform to the conservation of mass constraint (Eq. 3.3). Now, the accuracies of the chemical potentials are improved by adding the partial pressure dependent part to them, as shown in Eq. 3.19. If necessary, \mathbf{N} is rebuilt (Eq. 3.31). Using the updated μ_i and the stoichiometric coefficients ν_{ij} , the changes of the R linearly independent Gibbs functions ΔG_j are determined by Eq. 3.38. From this, the reaction-extent variables ξ_j are modified applying Eq. 3.47. Since the equilibrium problem of minimising G is solved iteratively, the previously estimated species abundances \mathbf{n} are corrected until a minimum of G is found. Applying the procedure as described by Smith and Missen (1982) and Wong et al. (2003), the \mathbf{n} are modified by means of a step-size parameter ω and the correction-vector $\boldsymbol{\delta n}$ in a way that for each $(m+1)^{th}$ iteration the species abundances change by

$$\mathbf{n}^{(m+1)} = \mathbf{n}^{(m)} + \omega^{(m)} \boldsymbol{\delta n}^{(m)}. \quad (4.11)$$

In accordance with Eq. 3.24, the correction-vector is given as

$$\boldsymbol{\delta n} = \mathbf{N} \boldsymbol{\delta \xi}. \quad (4.12)$$

Nevertheless, to fulfil the non-negativity constraint, a scaling factor κ is used (similar to κ in Eq. 4.7):

$$\delta \mathbf{n} = \kappa \mathbf{N} \delta \boldsymbol{\xi} \quad \text{with} \quad 0 < \kappa \leq 1. \quad (4.13)$$

Here, κ ensures that the changes $\delta \mathbf{n}$ do not exceed the current abundances and prevents negative abundances. To determine the factor, **SESAM** initially regards

$$\max_{1 \leq i \leq N} \left\{ -\frac{\delta n_i}{n_i} \right\} \quad \text{with} \quad n_i \geq 0. \quad (4.14)$$

Only if the maximum of this ratio is lower than one, which means that the changes in the abundances are always positive, a full correction of the species amounts is applied by setting $\kappa = 1$ in Eq. 4.13. In all other cases, $\delta \mathbf{n}$ is reduced by setting $\kappa = 0.99 / \max(-\delta n_i / n_i)$ to avoid negative species abundances. Afterwards, the step-size parameter ω must be determined. Since finding G is a minimisation problem, ω has to be chosen so that G diminishes with each iteration step m :

$$G(\mathbf{n}^{(m)} + \omega^{(m)} \delta \mathbf{n}^{(m)}) < G(\mathbf{n}^{(m)}). \quad (4.15)$$

Applying the descent method approach, this condition is met when $\delta \mathbf{n}^{(m)}$ satisfies

$$\left(\frac{dG}{d\omega^{(m)}} \right)_{\omega^{(m)}=0} \equiv \sum_{i=1}^N \left(\frac{\partial G}{\partial n_i} \right)_{\mathbf{n}^{(m)}} \delta n_i^{(m)} < 0, \quad (4.16)$$

unless $\partial G / \partial \mathbf{n} = \mathbf{0}$. The derivative $dG/d\omega$ can be obtained by means of Eq. 3.11 and $\delta \mathbf{n}$ from Eq. 4.13:

$$\frac{dG}{d\omega} = \sum_{i=1}^N \mu_i \delta n_i. \quad (4.17)$$

To find the suitable value of ω that minimises the Gibbs function

$$\left(\frac{dG}{d\omega} \right)_{\omega=1} = \sum_{i=1}^N \left(\frac{\partial G}{\partial n_i} \right)_{\omega=1} \delta n_i^{(m)} \quad (4.18)$$

is calculated. If the resulting value is positive, ω will be reduced by

$$\omega^{(m)} = \frac{(dG/d\omega)_{\omega=0}}{(dG/d\omega)_{\omega=0} - (dG/d\omega)_{\omega=1}} \quad (4.19)$$

because a positive $dG/d\omega$ means that a minimum in G has already been exceeded by the applied quantity of ω , assuming the Gibbs function as a parabolic function of ω . If Eq. 4.18 is equal to zero or negative, **SESAM** continues the calculation of the changes in the species abundances using $\omega = 1$ in Eq. 4.11, since G is not yet minimised by ω and the full correction by $\delta \mathbf{n}$ is needed. Once the new species abundances are determined, the convergence criterion

$$\max_{1 \leq i \leq N} \left| \frac{\delta n_i^{(m)}}{n_i^{(m)}} \right| \leq \varepsilon \quad \text{with} \quad \varepsilon = 1 \cdot 10^{-8} \quad (4.20)$$

is checked and if fulfilled, SESAM's iterative method is considered terminated and the equilibrium composition is found. Otherwise the code repeats the calculation of the \mathbf{b} , μ_i , ΔG_j , $\delta \xi_j$ and ω using the latest species abundances until convergence is achieved.

4.1.2 Treatment of condensed species and ions

Condensed species

Liquids and solids form in high-pressure and low-temperature environments where a high number of collisions takes place. These conditions can typically be found in the photospheres of ultra-cool dwarfs and stars.

In SESAM, condensed species can be treated as single species phases, which means that a solid or liquid phase contains only exactly one species. There are no equilibrium effects within one condensed phase but each condensed species is in equilibrium with the gaseous phase. This represents the condition that the liquids and solids do not always mix with each other. Instead, they are spread in the system and do not bond together into large lumps. Figuratively speaking, this corresponds to many little crumbs (or fine droplets, respectively) floating in the gas.

Due to these considerations, disparities from Sec. 4.1.1 occur, regarding the handling of condensed species, following Smith and Missen (1982). First of all, the species must be separated in the respective phases α , to consider them as being in the gaseous, liquid, solid, or single species phase. During each iteration, single species phases may be deleted or included in the main calculation, depending if an introduction increases or, respectively, decreases the Gibbs function. Therefore, it is necessary to consider them as non-component species and not as component species because components must be non-zero to successfully form the non-components.

For the calculation of the chemical potentials (Eq. 3.19), the mole fractions x_i must be considered as being phase-dependent: $x_{i,\alpha} = n_{i,\alpha}/n_{t,\alpha}$. A single species phase has consequently $x_{i,\alpha} = 1$, resulting in $\mu_i = \mu_i^*(T, P)$. The condition for it to be present or absent in the chemical composition replaces Eq. 3.36 and is given by

$$\frac{\partial G}{\partial n_i} \equiv \frac{\partial G}{\partial \xi_j} = \mu_i^* + \sum_{k=1}^M \nu_{kj} \mu_k = 0 \quad \text{with} \quad j \in \{1, 2, \dots, R\}; \quad i \in \{1, 2, \dots, N\}, \quad (4.21)$$

for $n_i > 0$, i.e. for the presence of the single species phase, and

$$\frac{\partial G}{\partial n_i} \equiv \frac{\partial G}{\partial \xi_j} = \mu_i^* + \sum_{k=1}^M \nu_{kj} \mu_k > 0 \quad \text{with} \quad j \in \{1, 2, \dots, R\}; \quad i \in \{1, 2, \dots, N\}, \quad (4.22)$$

for its absence, $n_i = 0$. The μ_i^* represents the standard chemical potential of the respective condensed species (Eq. 4.4), which is determined from the NIST-JANAF Thermochemical Tables, analogously to the μ_i^* of the gaseous species.

This approach of single species phases is not as physically realistic as the detailed dust treatment in PHOENIX' DRIFT-module (Dehn, 2007, based on the dust model code of Helling et al. 2008) where the complex processes of nucleation, growth, evaporation, and motions of dust grains are taken into account. DRIFT solves the rate equations of these

processes, thus, it is slower than **SESAM**, which relies on the energy minimization method. However, as a simple approximation of chemical equilibria containing condensed species in a gaseous environment, **SESAM**'s approach is substantially more accurate than the one of the currently used EOS in **PHOENIX**, **ACES**, which assumes a multi-species condensed matter phase (see Sec. 4.2). **ACES** does not treat liquids and solids separately and, consequently, they are all clumped together. This situation is not very realistic in atmospheres because condensed species are mainly widely dispersed instead of forming one single lump.

Ions

As mentioned in Sec. 2.2.1, at sufficiently high gas temperatures, particles ionise and the released free electrons eventually interact with other free electrons, bound electrons, and nuclei. In **SESAM**, the resulting plasmas are treated ideally. This is an appropriate approximation in environments where the Coulomb collisions are negligibly small. While this assumption is valid in stellar photospheres, for rarefied environments, e.g., the corona, or for the very dense atmospheres of degenerated objects like white dwarfs and neutron stars, the plasma should be treated non-ideally.

To take the charge-balance constraint into account, the formula matrix **A** includes an additional row for each species, specifying if the respective species is neutral or if it has an excess or deficiency of electrons relative to the neutral species. This way, charge conservation is always satisfied in the stoichiometric procedure.

4.1.3 Convergence behaviour

In **SESAM**, the chemical equilibrium problem is considered as solved when all species fulfil the convergence criterion in Eq. 4.20. Figure 4.2 displays the respective changes $|\delta n_i^{(m)} / n_i^{(m)}|$ during the iterative process of four arbitrary temperature and pressure points representing typical stellar environments.

- The 1500 K, $5 \cdot 10^{-5}$ Pa condition can be found in the upper photospheric layers of M-dwarfs, i.e., at an optical depth τ_{std} (will be defined in Sec. 4.2) of around $1 \cdot 10^{-10}$. The atmosphere is dominated by molecules and neutral species. The positive values in the figure are caused by an overestimate of the initial abundances of a few condensed species: these values are eventually strongly reduced and convergence is achieved.
- A T - and P -point at $\tau_{\text{std}} = 1 \cdot 10^{-4}$ of a F-dwarf is symbolised by the 4000 K and 55 Pa point. Here, fewer molecules and more ions are present in equilibrium compared to the 1500 K case.
- In the deeper photospheric layers, at optical depths of 16, the F-star features high-temperature, high-pressure environments, represented by the 10000 K and 7000 Pa point. The respective chemical composition contains mostly ions and neutral atoms.
- The fourth case has a temperature of 25000 K and a pressure of 3000 Pa. This condition can be found deep in the photospheres at around $\tau_{\text{std}} = 100$ in A-dwarfs. Mostly ions and neutral species are present in these high-temperature environments.

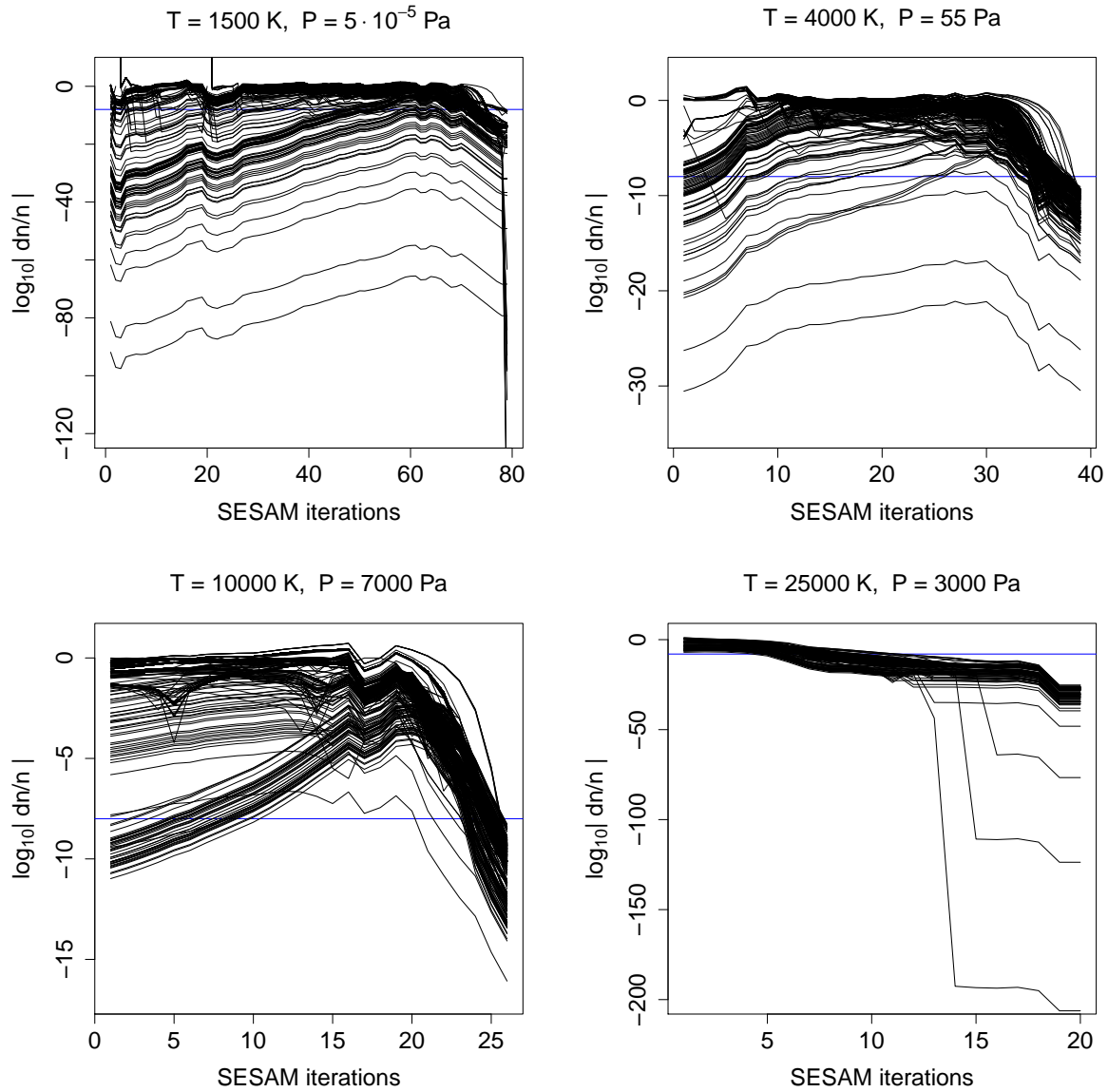


Figure 4.2: SESAM's convergence behaviour of four typical T - and P -points in stellar models. The changes $|\delta n_i^{(m)} / n_i^{(m)}|$ as function of the iterations m are plotted for each individual species i (black lines). The blue line at $1 \cdot 10^{-8}$ marks the threshold of which the iterative process is considered terminated (Eq. 4.20).

In the first iteration, **SESAM** takes the guessed species abundances and corrects them during the next iterations. Once the chemical composition is close to the equilibrium one, the correction of the species abundances are steadily decreasing until they are considered to be converged (for instance, from iteration 20 to 26 in the 10000 K case). This particular smooth behaviour can be seen in each plot of Fig. 4.2.

Furthermore, the results are stable and do not change if the number of iterations is artificially increased, which is presented in Fig. 4.3, taking the 4000 K and 55 Pa test case as example. In this figure, the changes $|\delta n_i^{(m)}/n_i^{(m)}|$ for all 747 species i are plotted from iteration $m = 100$ to 10^6 . The maximum changes are $\sim 10^{-16}$, being significantly lower than the relative error due to the machine precision and certainly much lower than the errors of the thermodynamic data.

SESAM shows a straightforward convergence behaviour. The species abundances do not change significantly after they were considered converged, which is an indispensable criterion for reliable and trustworthy solutions. Especially with a look for overall convergence of an atmosphere with potential feedback on the EOS once combined with the radiative transfer or hydrodynamic modules. Stable and unambiguous results limit a potential destabilisation of such feedback loops to a minimum.

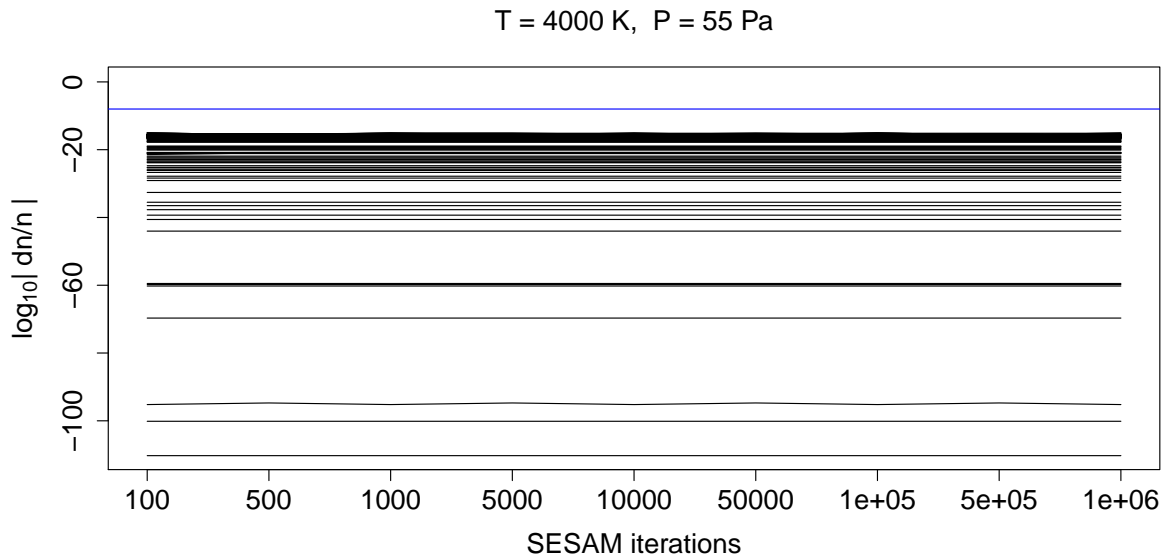


Figure 4.3: Same as the 4000 K and 55 Pa test case in Fig. 4.2, but the $|\delta n_i^{(m)}/n_i^{(m)}|$ are plotted up to 1 million **SESAM** iterations. The plot starts with the 100th iteration to show the changes $|\delta n_i^{(m)}/n_i^{(m)}|$ of an already converged system.

4.2 The atmosphere model code **PHOENIX**

PHOENIX is a general-purpose atmosphere code, calculating the atmospheric structure and spectrum of different stars and star-like objects including, for instance, main-sequence stars, supernovae, novae, white dwarfs, brown dwarfs, giants, Jovian planets, and even disks. In order to accomplish this, lots of computational time is required, which is substantially reduced by simplifying approximations and a high parallelisation of the code. Depending

on the objects under investigation, PHOENIX uses different physical conditions, e.g., the expanding supernovae atmospheres are treated dynamically, while it is in many cases physically sufficient to consider main-sequence stars statically. Next to the one-dimensional computation, the code is capable to calculate three-dimensional radiative transfer. The validation of the newly included EOS module SESAM has been specifically done for time-independent model atmospheres, using the thermodynamic approximations LTE and NLTE (Chapter 5). Accordingly, the following description of the PHOENIX code focuses on this configuration.

The models feature spherical symmetry. Each atmosphere computed in this thesis is divided in 64 concentric shells, also referred to as layers. Discrete values of physical quantities are considered for each layer, for instance, the temperature, gas pressure, density, and moments of the radiation field. The atmospheric layers are defined by a standard optical depth grid, τ_{std} . It is calculated for the continuum at a standard wavelength λ_{std} with $\lambda_{\text{std}} = 1.2 \mu\text{m}$ for cool models und $\lambda_{\text{std}} = 500 \text{ nm}$ for hot models. The standard optical depth for the first layer, $\tau_{\text{std},1}$, is zero, and it is logarithmically spaced between the second and 64th layer with $\tau_{\text{std},2} = 10^{-10}$ and $\tau_{\text{std},64} = 100$.

Iterative method

After specifying the model stellar parameters like, e.g., the mass, effective temperature, radius and element abundances, PHOENIX typically imports an atmosphere for nearby stellar parameters as starting point.

Supplied with the initial atmospheric temperature profile, the pressure profile, the element abundances, and a list of species, the currently used EOS ACES solves the chemical equilibrium problem based on the VCS method (Smith and Missen, 1982). This is done for each T - and P -point. ACES uses the partial pressures from pre-computed partial pressure tables as initial species abundances for the equilibrium determination. Due to the limitation of table sizes and numbers, it is not expedient to store all T - and P -points that may occur during a model calculation. For this reason, ACES will pick the abundances of the T - and P -point as close as possible to the actual temperature and pressure required for the demanded equilibrium. In contrast to SESAM, ACES takes only the chemical potentials for molecules from the polynomial data (Eqs. 4.3 and 4.4). The atomic data for neutral atoms, condensed species, and ions are calculated from the LTE and NLTE partition functions (Eqs. 2.16 and 2.21) provided by PHOENIX. This ensures consistency of the NLTE line data with the NLTE level data. During the ACES-iterations, trace species with moles lower than $1 \cdot 10^{-34}$ are skipped and arbitrarily set to $1 \cdot 10^{-26}$ mol. Solids and liquids are treated with the approach of a multi-species condensed matter phase where equilibrium effect are present in the condensed phases. ACES does not distinguish between solids and liquids. In other words, all solids and liquids are formed together into one single lump.

Based on the computation of the altitude-depending chemical compositions, PHOENIX obtains the gas pressures in the next step. Assuming that radiation and convective motions are not significantly affecting the gas pressure, the pressure profile is calculated from the integration of the hydrostatic equation

$$\frac{dP}{dr} = -\rho(r)g \quad (4.23)$$

where the radius r defines the radial distance to the stellar centre, g is the surface gravity, and ρ is the density.

If convection is included in the model set-up, PHOENIX applies the mixing-length theory (Böhm-Vitense, 1958). For each τ_{std} , the temperature gradient is compared to the adiabatic gradient and layers are assumed to be convective if the condition expressed in Eq. 2.1 is met.

To decrease the computational time of the line opacities, PHOENIX selects dynamically the appropriate atomic and molecular line opacities from databases (e.g. the Kurucz atomic line data: Kurucz and Bell, 2011). This means that LTE lines are included in the calculation if their absorption coefficient κ_{line} is greater or equal a certain threshold, which is typically set to $10^{-4} \cdot \kappa_{\text{cont}}$ at selected reference depth points, with the continuous absorption coefficient $\kappa_{\text{cont}} = \kappa_{\text{bf}} + \kappa_{\text{ff}}$. These coefficients from the bound-free and free-free transitions are highly dependent on the chemical composition. PHOENIX assumes the depth-dependent profiles of these lines to be either Voigt or, for weak lines, Doppler profiles.

Rate equations and the radiative transfer equation are solved iteratively until a stable solution is found. A detailed description of the full iterative scheme can be found in, e.g., Hauschildt (1993); Hauschildt and Baron (1999). Considering static atmospheres, radiative equilibrium must be satisfied in the radiative zones, stating that the flux is conserved in each optical depth. The local gas temperatures are corrected so that this condition is locally fulfilled. For this purpose, PHOENIX uses the modified Unsöld-Lucy method, described in Hauschildt et al. (2003). Only when the temperature correction is sufficiently small in each layer, the atmospheric structure is in radiative equilibrium and the model is considered physically consistent. Otherwise, the new atmospheric temperature and density structures may serve as reasonable starting values for a new PHOENIX run with slightly different parameters.

4.3 Modifications and settings for the synergy of SESAM with PHOENIX

For the inclusion of the stand-alone SESAM code as a module in PHOENIX, modifications were done in order to use this new EOS. It is now possible to adopt SESAM by simply picking one PHOENIX input parameter. No further settings must be done by the user.

To determine the opacities of the atmospheres, PHOENIX demands the respective equilibrium compositions for numerous different temperature and pressure points. SESAM provides this by applying the constraints of constant (T, P) . For this purpose, the module receives the element abundances from PHOENIX, the list of species considered to be relevant, and the current T - and P -point as input data for the EOS. After solving the chemical equilibrium problem, SESAM hands over the mole fractions of all species to PHOENIX.

Furthermore, SESAM's source of the chemical potentials had to be modified and, for a better comparability with ACES, minor species should be treated identically in the two modules. Both issues are discussed below.

Chemical potentials for LTE and NLTE species

As discussed above in Sec. 4.2 and 4.1, both EOS's determine the chemical potentials μ_i of the i^{th} species by means of the polynomial data (Eqs. 4.3 and 4.4), whereas ACES applies them only for molecules. To ensure consistency of the NLTE line data with the NLTE level data, ACES' values for the neutral atoms, condensed species, and ions are provided by the PHOENIX generalised partition functions (Eqs. 2.16 and 2.21). Consequently, the two different approaches will generate μ_i that deviate from each other. This is true for several species. For instance, Fig. 4.4 displays the differences for neutral barium and singly-ionised barium: at temperatures below 2000 K, the partition functions provide in both cases higher chemical potentials than the polynomial data, which means the species will more likely react with other species.

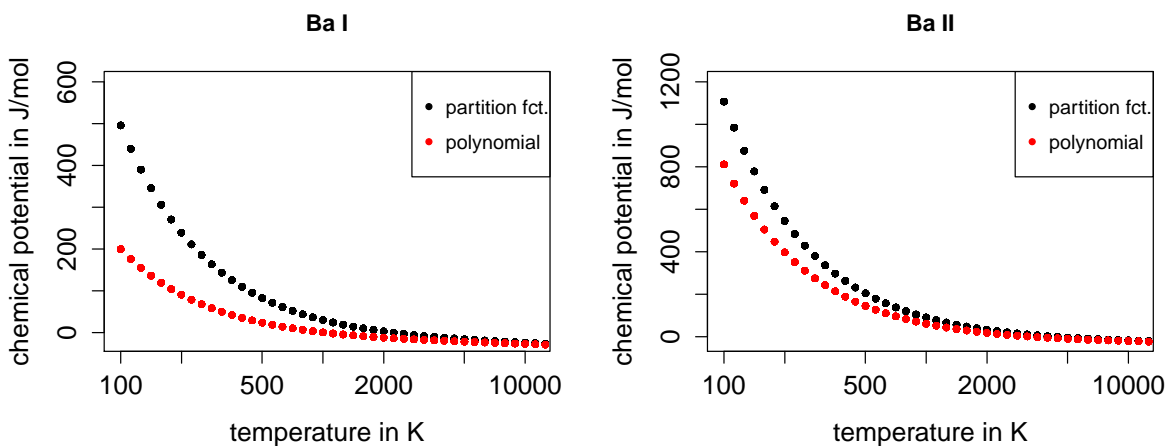


Figure 4.4: The chemical potentials for Ba I (left panel) and Ba II (right panel). Red values are based on polynomial thermodynamic data and black values on the partition function, as implemented in PHOENIX.

Due to the fact that the μ_i crucially affect the equilibrium compositions, the two EOS's eventually produce different opacities and the respective spectra will deviate from each other. This is emphasized in the following exemplary atmosphere of a $T_{\text{eff}} = 3000$ K star, calculated with the help of SESAM. Because most polynomials cover temperatures from 200 K to 6000 K for molecules, and from 200 K to 20000 K for neutral atoms and ions, the low effective temperature model guarantees a high number of μ_i being calculated from the polynomial data. SESAM was modified in a way that this data were used for all species if provided, otherwise the chemical potentials from the partition functions were taken. Afterwards, this model was compared with an atmosphere where SESAM took all chemical potentials (except for the molecules) from the PHOENIX partition functions. Consequently, the resulting fluxes deviate from each other, as displayed in Fig. 4.5. In this figure, spikes represent differences in the lines. This occurs predominantly in the spectral lines of various neutral elements and ions, which chemical potentials deviate, respectively, regarding the two kinds of data sources. For example, particularly noticeable are the lines at 455.5 nm, 614.3 nm, 1130.3 nm, and 1500.4 nm where the first two belong to Ba II and the latter two to Ba I. A closer look (Figs. 4.6 and 4.7) reveals that there is less absorption when the chemical potentials are taken from partitions functions compared to polynomial data. This is in agreement with both Ba I and Ba II: the μ_i of the

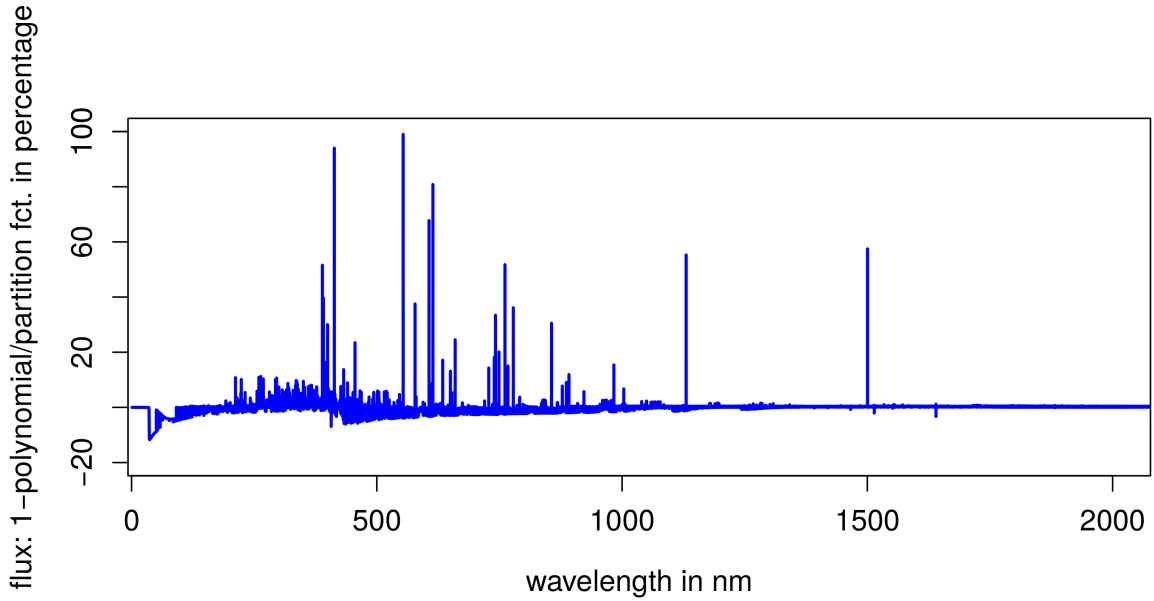


Figure 4.5: Percentage deviation of a spectrum, using the chemical potentials based on the polynomial thermodynamic data, from a spectrum with the chemical potentials determined by the partition functions. Both models represent the same M-dwarf of $T_{\text{eff}} = 3000$ K and $\log(g) = 4$ and were calculated by applying SESAM.

polynomial data is at any temperature considered in this model higher than the μ_i from the partition functions, consequently, the species reacts more likely and is less abundant in the equilibrium composition. Therefore, the differences in the μ_i of the Ba I and Ba II directly impact the opacities: spectral lines that involve these species show less absorption when only values from the partition functions were applied, compared to the polynomial data.

Thus, for the determination of accurate spectra, one essential requirement is to carefully select the respective data sources for the chemical potentials. To provide consistency within PHOENIX considering the NLTE data, SESAM was modified so that the μ_i of the neutral atoms, ions and condensed species are directly taken from the PHOENIX partition functions. The application of the molecular polynomial data according to Eqs. 4.3 and 4.4 is unchanged.

Minor species

During the iteration process of the EOS, the species abundances are modified according to Eq. 4.11 until the minimum of the Gibbs function is found. If the emerging species amounts are low, the corresponding step-size parameter ω also has to be low to serve the non-negativity constraint (Eq. 3.4). This decelerates the calculation time for finding the suitable G (Smith and Missen, 1982). However, it can be avoided by excluding the minor species from the equilibrium calculation as it is done in ACES with species that have abundances of less than 10^{-34} mol. In ACES, these skipped minor species are generally set to 10^{-26} mol. Due to the conservation of mass constraint (Eq. 3.2), the amount of these minor species may reach a critical quantity, so that this could affect the other species abundances. SESAM, on the contrary, does not exclude any species and consequently

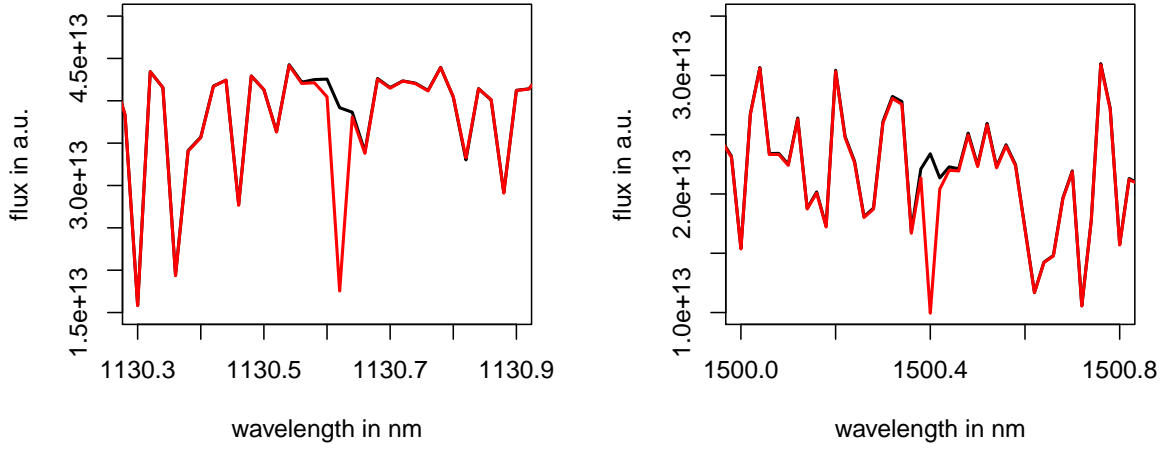


Figure 4.6: Sections of the spectra of the model from Fig. 4.5. The red lines represent the case where the chemical potentials are based on polynomial data, the black lines the case where they are determined by the partition functions. Deviations are visible in the Ba I lines at 1130.6 nm and 1500.4 nm.

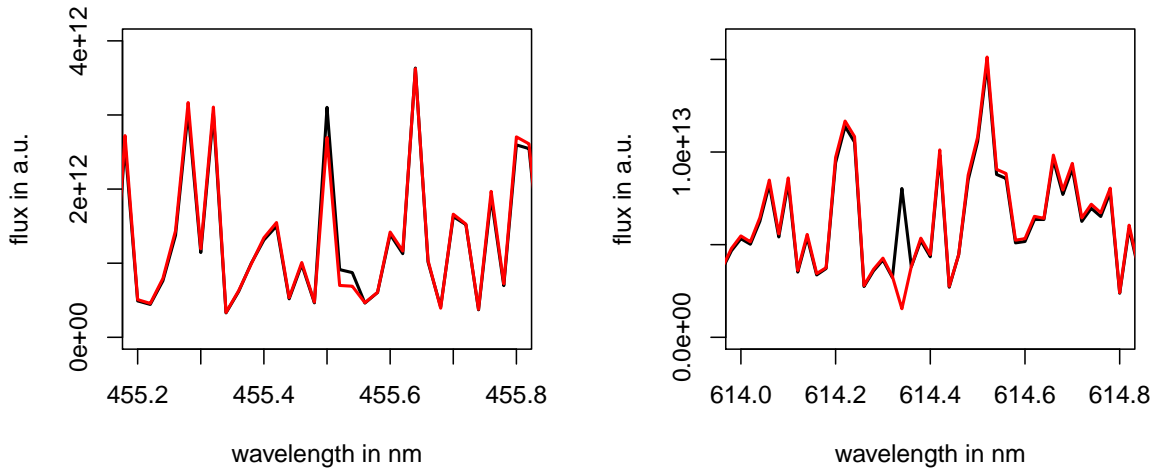


Figure 4.7: Sections of the spectra of the model from Fig. 4.5. The red lines represent the case where the chemical potentials are based on polynomial data, the black lines the case where they are determined by the partition functions. Deviations are visible in the Ba II lines at 455.5 nm and 614.3 nm.

uses the respective determined abundances. For a better comparison of the two modules, skipping of minor species and overwriting of abundances are disabled in **ACES** throughout the calculations.

Chapter 5

Results: Testing the new EOS module

SESAM is a well tested EOS, reliably calculating accurate equilibrium compositions, as shown and summarised in Sec. 4.1. It has been included in the model atmosphere code PHOENIX and the interplay between both codes is investigated in this chapter. A direct comparison with ACES, the currently used EOS in PHOENIX, displays the differences between them.

A measurable quantity in this context is the atmospheric pressure, calculated by PHOENIX utilising SESAM's and ACES' equilibrium abundances. The agreement of the respective pressure profiles is examined in detail in Sec. 5.1 for nine different models along with a convergence analysis of the atmosphere structure. Furthermore, also the radiative fluxes must be identical for all wavelengths if both EOS's provide the same equilibrium compositions, which is tested in Sec. 5.2.

A solution of the EOS is fully defined by the temperature and pressure point, the element abundances and the species considered to be relevant in the calculation. Both SESAM and ACES use initial species abundances to improve their convergence speed. Indispensable condition for reliability is the independence of the equilibrium compositions from these initial estimates, though. Section 5.3 deals with the sensitivity of the EOS codes' convergence with respect to variations of these abundances.

In Sec. 5.4, the test models are complemented by atmospheres involving convection, species in non-local thermodynamic equilibrium, and sub-solar metallicities, all including a direct comparison between SESAM and ACES.

During each PHOENIX iteration, the EOS is called more than a thousand times, while in the multi-dimensional configuration, PHOENIX/3D, it is called even millions of times. Consequently, the slower an EOS, the more computationally expensive is the calculation of a model atmosphere. In this context, SESAM's performance was measured and corresponding tests are presented in Sec. 5.5.

The term *chemical abundance* refers to the amount of the species expressed in moles, as calculated by the EOS's. *Chemical concentration* refers to the number of particles per cm^{-3} , which is determined by PHOENIX.

5.1 Atmospheric temperature and pressure structure

As described in Sec. 4.2, PHOENIX determines the pressure structure of a model atmosphere by solving the hydrostatic equation (Eq. 4.23), resulting in discrete pressure values for each atmospheric layer. Provided with the respective temperatures and the element abundances, the EOS computes the equilibrium composition. PHOENIX uses the results from the EOS to calculate the opacities, which in turn affect the intensities and eventually the spectrum and the radiative flux. The EOS is, therefore, a determining factor for the construction of the model atmosphere during this iterative process.

The PHOENIX code simulates atmospheres that entail a wide range of different physical conditions. From molecule-rich environments at low effective temperatures, to plasmas at high effective temperatures, SESAM must determine the respective chemical equilibria reliably and physically consistently. This is investigated by calculating atmospheres of stars with effective temperatures of 3000 K, 6000 K, and 10000 K as important test cases. This is combined with varied surface gravities $\log(g)$ of 3, 4, and 5 to sample a wide stripe in the Hertzsprung-Russell diagram in order to study the interplay between SESAM and PHOENIX. All nine models were calculated using SESAM and ACES. To provide a better comparison, convective motions were not taken into account excluding their influence on the results. Furthermore, minor species were explicitly included in the consideration. The starting models were taken from the library of PHOENIX stellar atmospheres calculated by Husser et al. (2013). The starting and calculated models have identical stellar parameters effective temperature, surface gravity, metallicity, and mass.

The choice of the EOS affects the number of iterations that PHOENIX needed to converge, with a slight advantage on the side of SESAM: all models combined needed 613 iterations with ACES and 608 iterations with SESAM.

Figure 5.1 shows the changes in temperatures between PHOENIX iterations for each atmospheric layer and iteration utilising SESAM. The first layer refers to an optical depth $\tau_{\text{std},1} = 0$ and the last layer, i.e. the 64th layer, to $\tau_{\text{std},64} = 100$ (see Sec. 4.2). This plot displays the same convergence behaviour for all nine models tested, irrespective of whether SESAM or ACES were used. The temperature changes are typically quickly decreasing without any strong fluctuations between the PHOENIX iterations, indicating a very good and straightforward convergence of PHOENIX and consistent with other error measurements. Only the temperature changes in the upper layers have a tiny decreasing trend. This region converges slower due to the complexity of the environment: the temperatures and densities are lower than in the rest of the photosphere. This low-opacity environment complicates the radiative transfer problem, allowing only small correction steps between the PHOENIX iterations.

In Figs. 5.2 - 5.10, the pressure profiles of the nine models with effective temperatures of 3000 K, 6000 K and 10000 K, all with a $\log(g)$ of 3, 4, and 5, are plotted, displaying the changes in pressures for each atmospheric layer with each iteration during the PHOENIX run. To enhance the clarity of the plots, red areas represent negative pressure changes, and blue areas positive ones.

In all nine models, SESAM produces a particularly smooth behaviour without significant

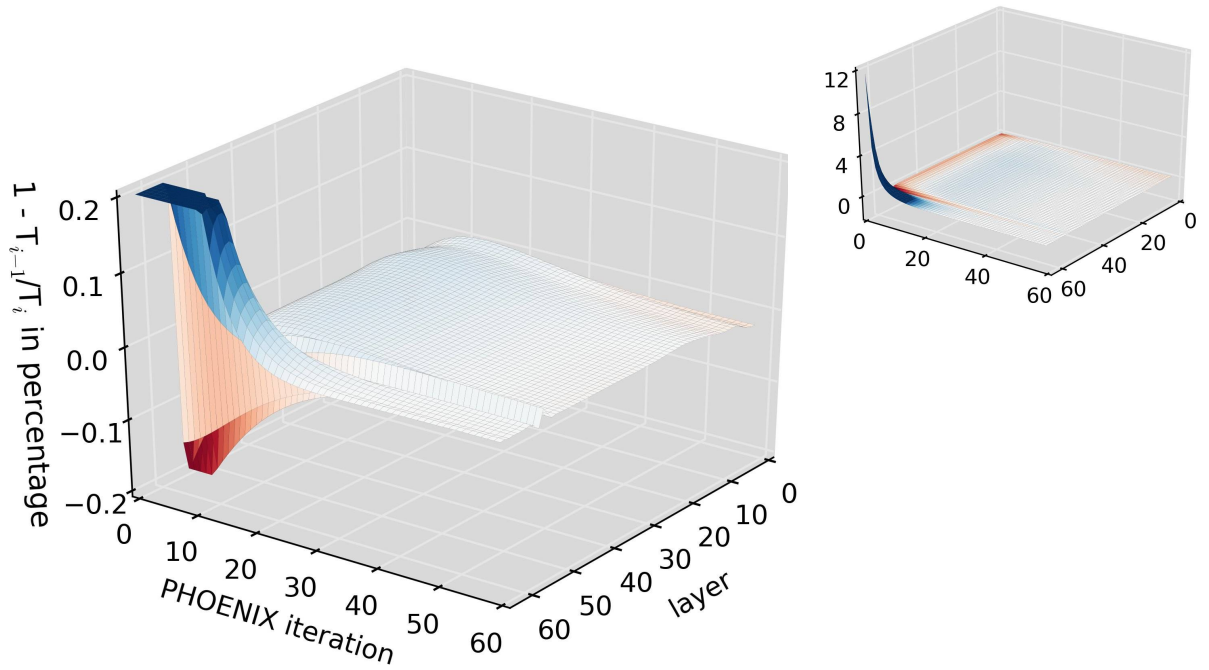


Figure 5.1: Changes in temperature between the i^{th} iteration of PHOENIX, T_i , and the previous iteration, T_{i-1} , for each atmospheric layer and each PHOENIX iteration. The left panel is the reduced scale of the full-scale representation on the right side, using identical axes. These plots show the model with $T_{\text{eff}} = 6000$ K and $\log(g) = 4$, calculated by the means of SESAM. The other cases discussed in Sec. 5.1 present the same convergence behaviour, regardless whether SESAM or ACES were applied.

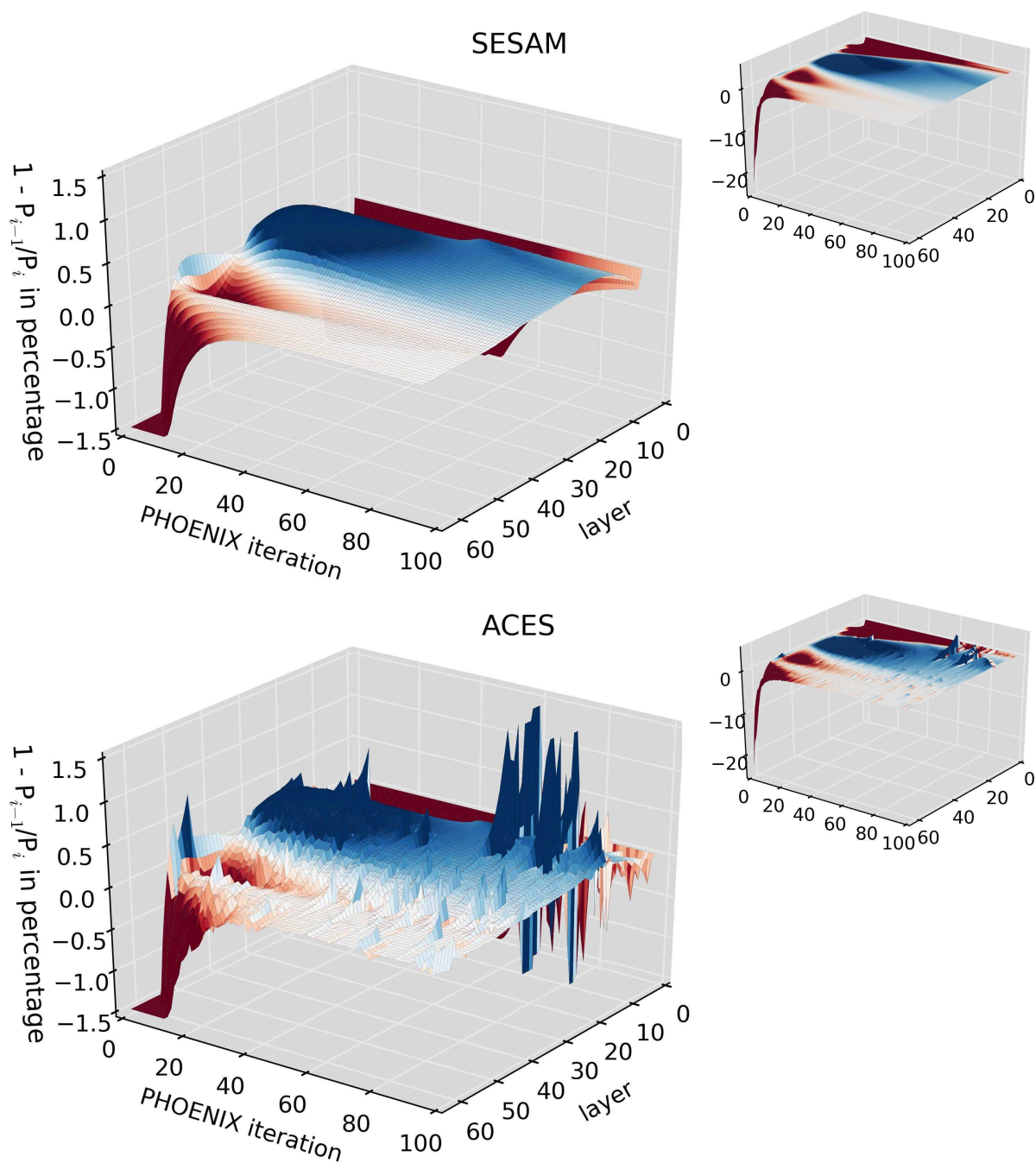


Figure 5.2: Changes in pressure between the i^{th} iteration of PHOENIX, P_i , and the previous iteration, P_{i-1} , for each atmospheric layer and each PHOENIX iteration of a $T_{\text{eff}} = 3000$ K and $\log(g) = 3$ model. The left panels are the reduced scale of the full-scale representations on the right side, using identical axes. SESAM and ACES were applied for the top and bottom panel, respectively.

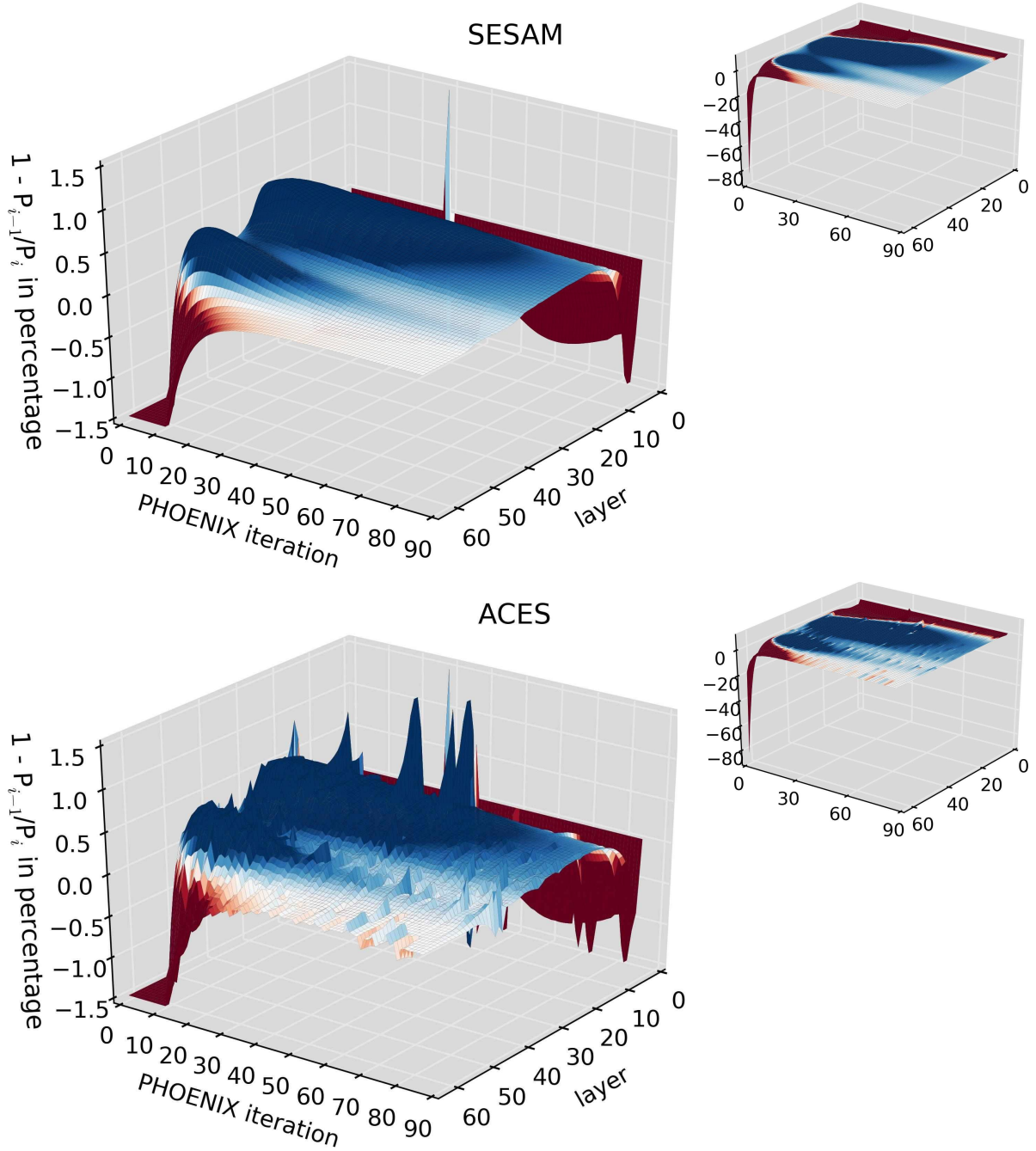


Figure 5.3: Same as in Fig. 5.2 but for a $T_{\text{eff}} = 3000$ K and $\log(g) = 4$ model.

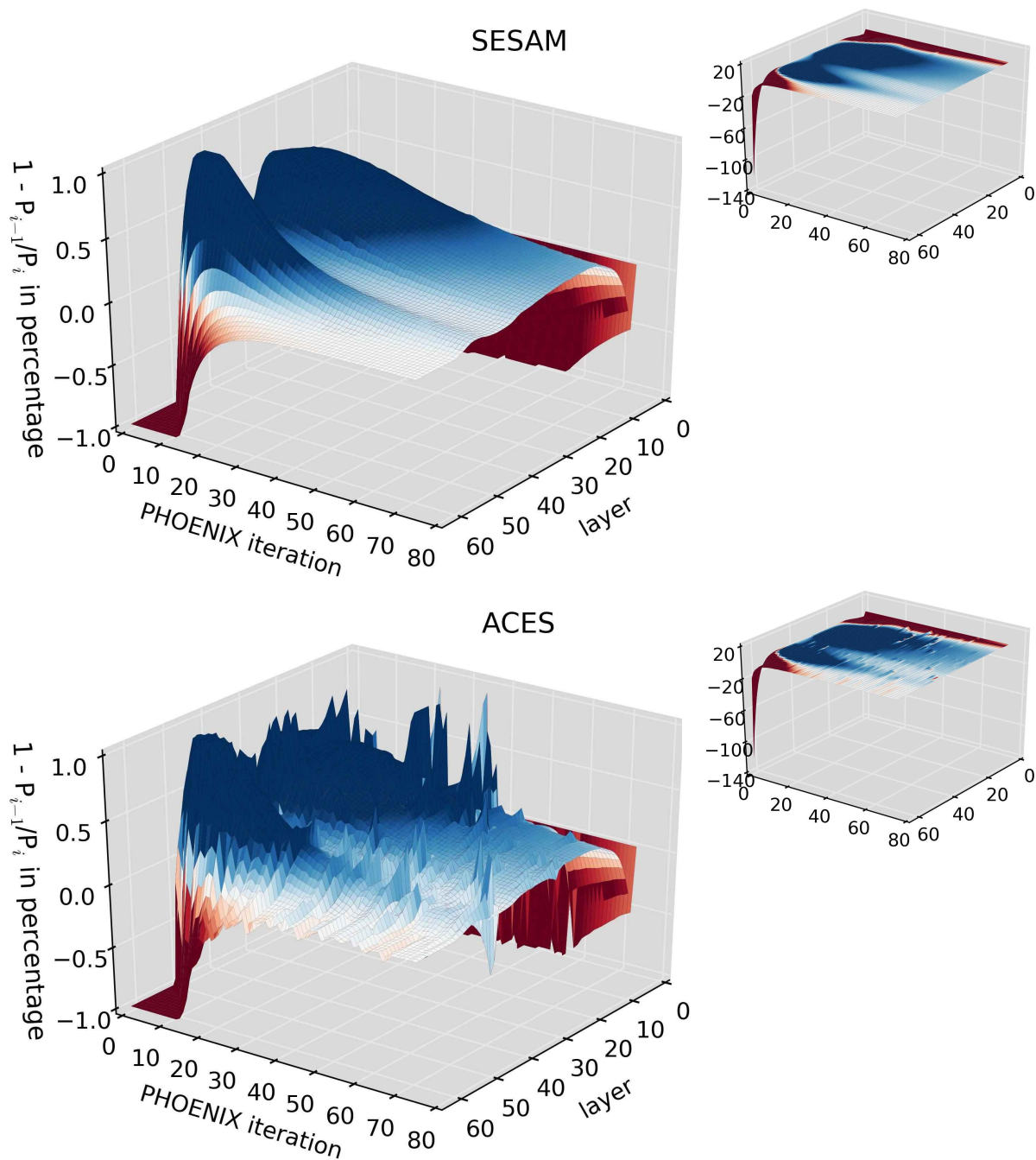
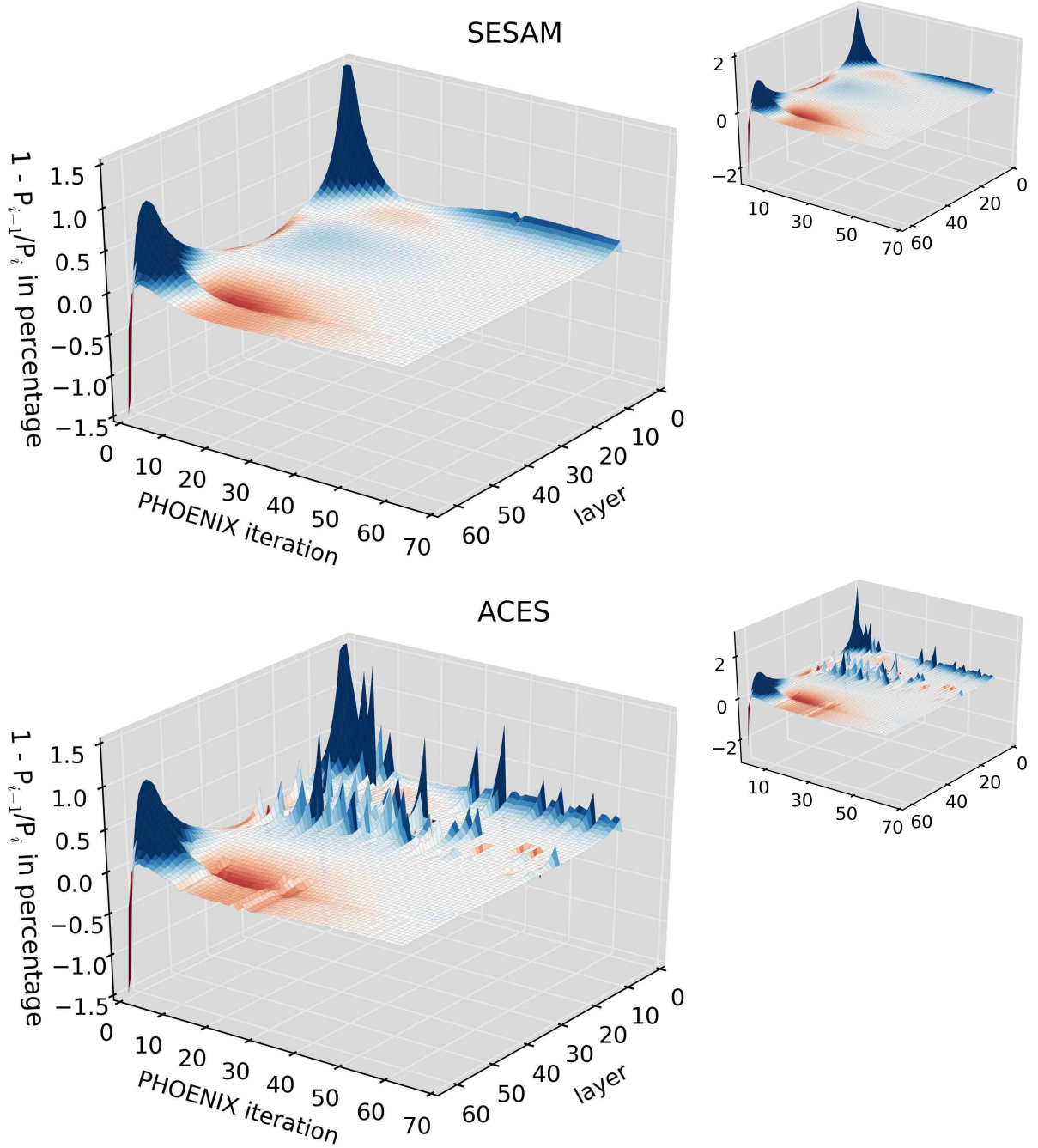


Figure 5.4: Same as in Fig. 5.2 but for a $T_{\text{eff}} = 3000$ K and $\log(g) = 5$ model.



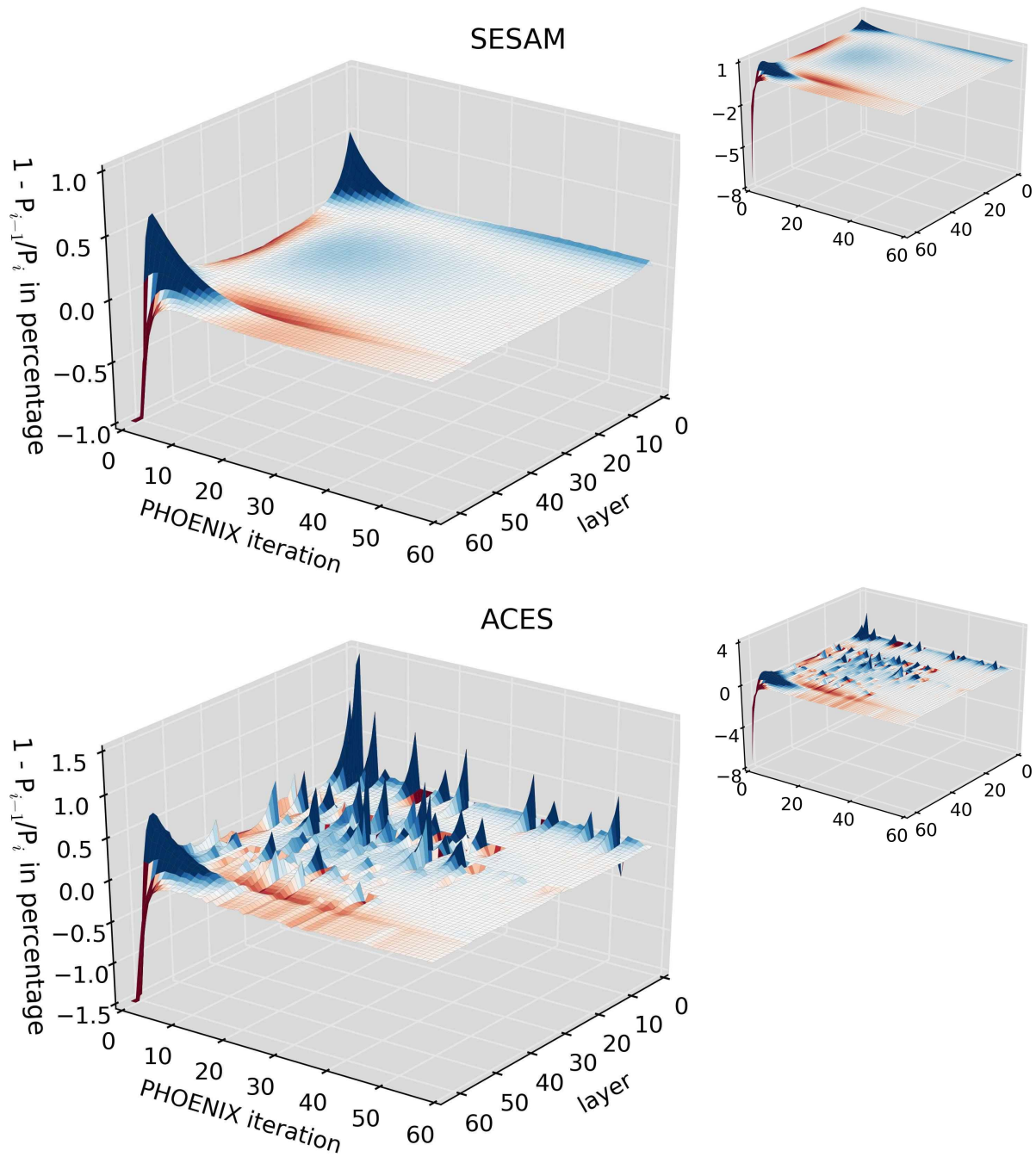
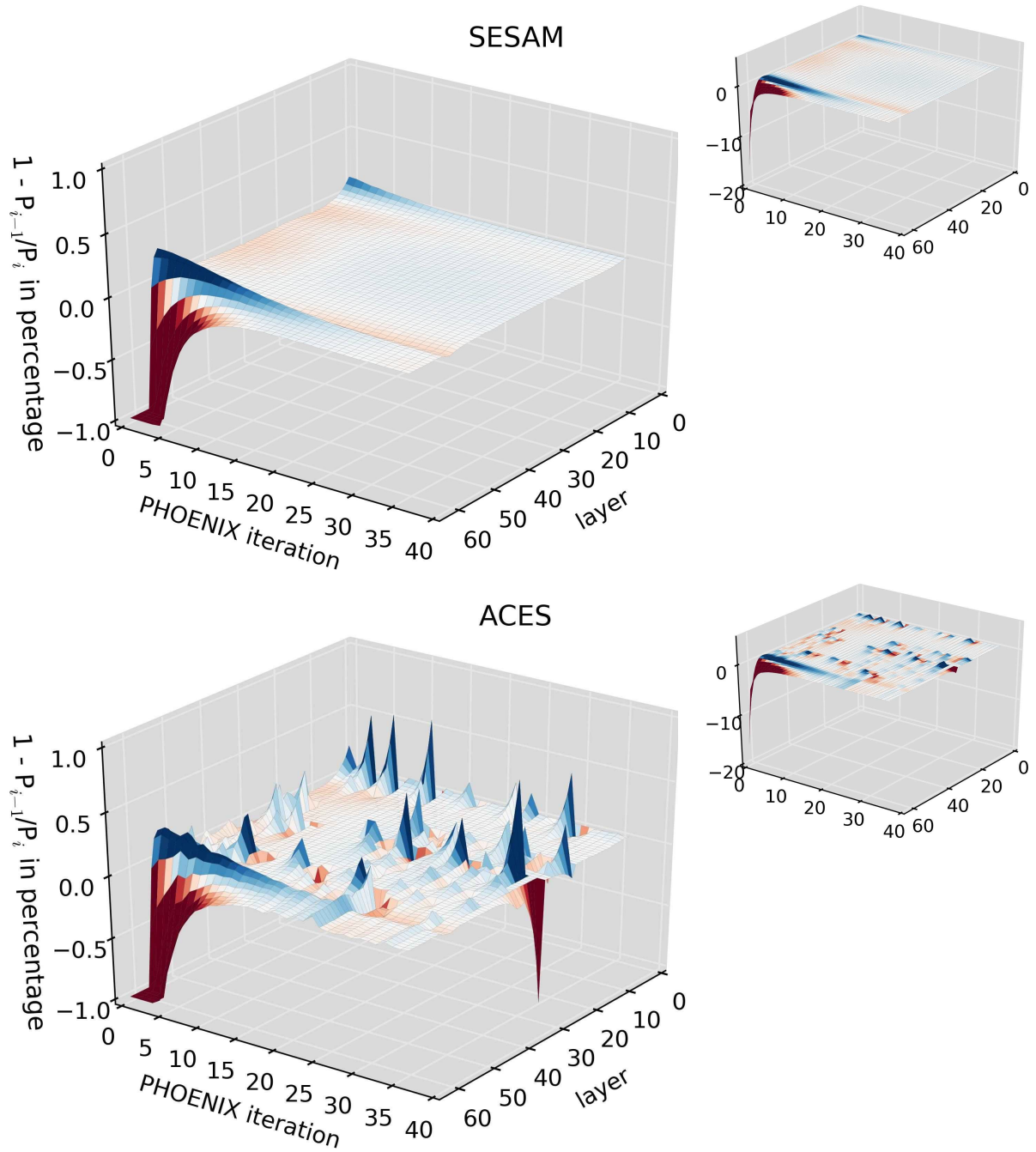


Figure 5.6: Same as in Fig. 5.2 but for a $T_{\text{eff}} = 6000$ K and $\log(g) = 4$ model.



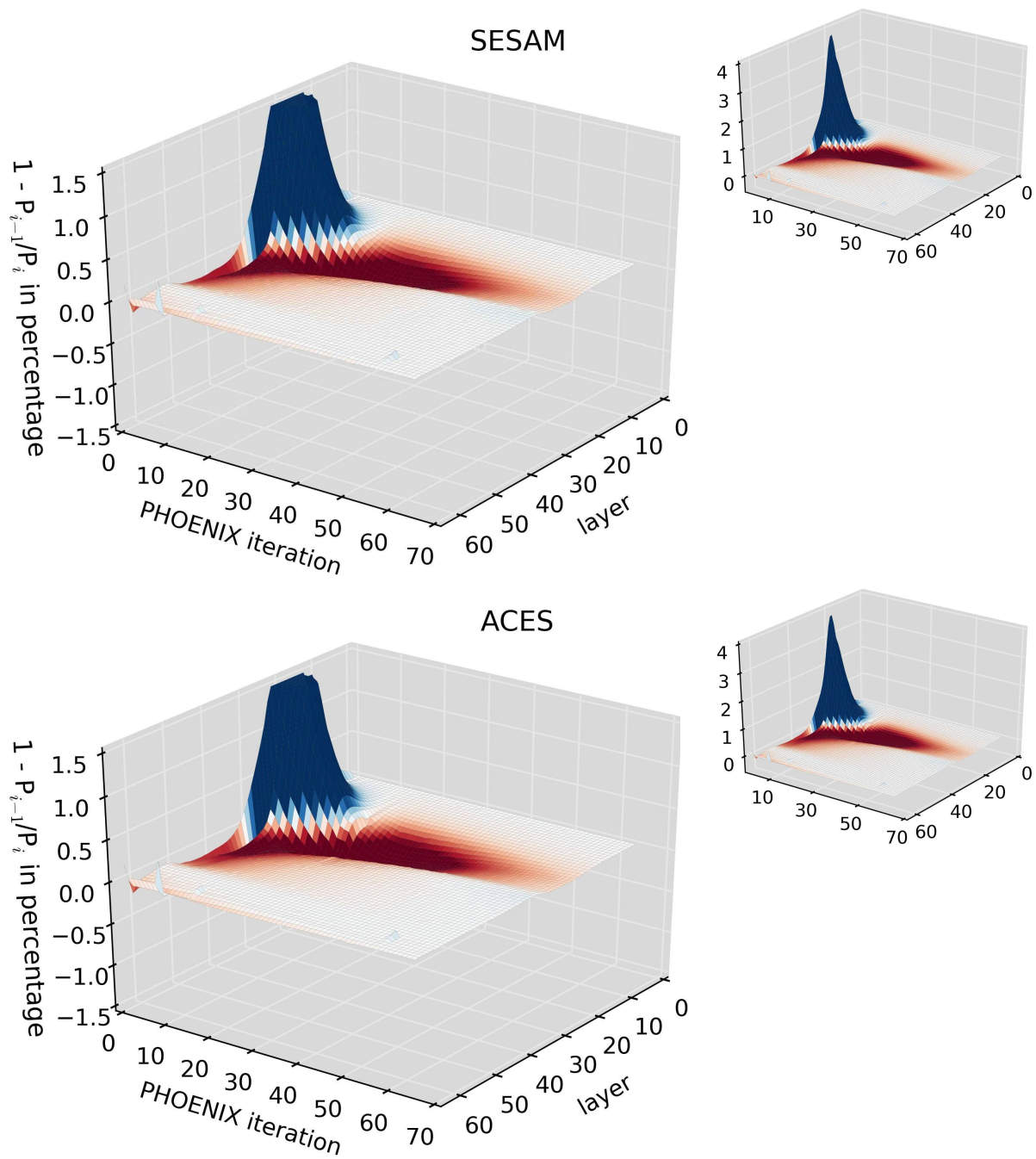


Figure 5.8: Same as in Fig. 5.2 but for a $T_{\text{eff}} = 10000$ K and $\log(g) = 3$ model.

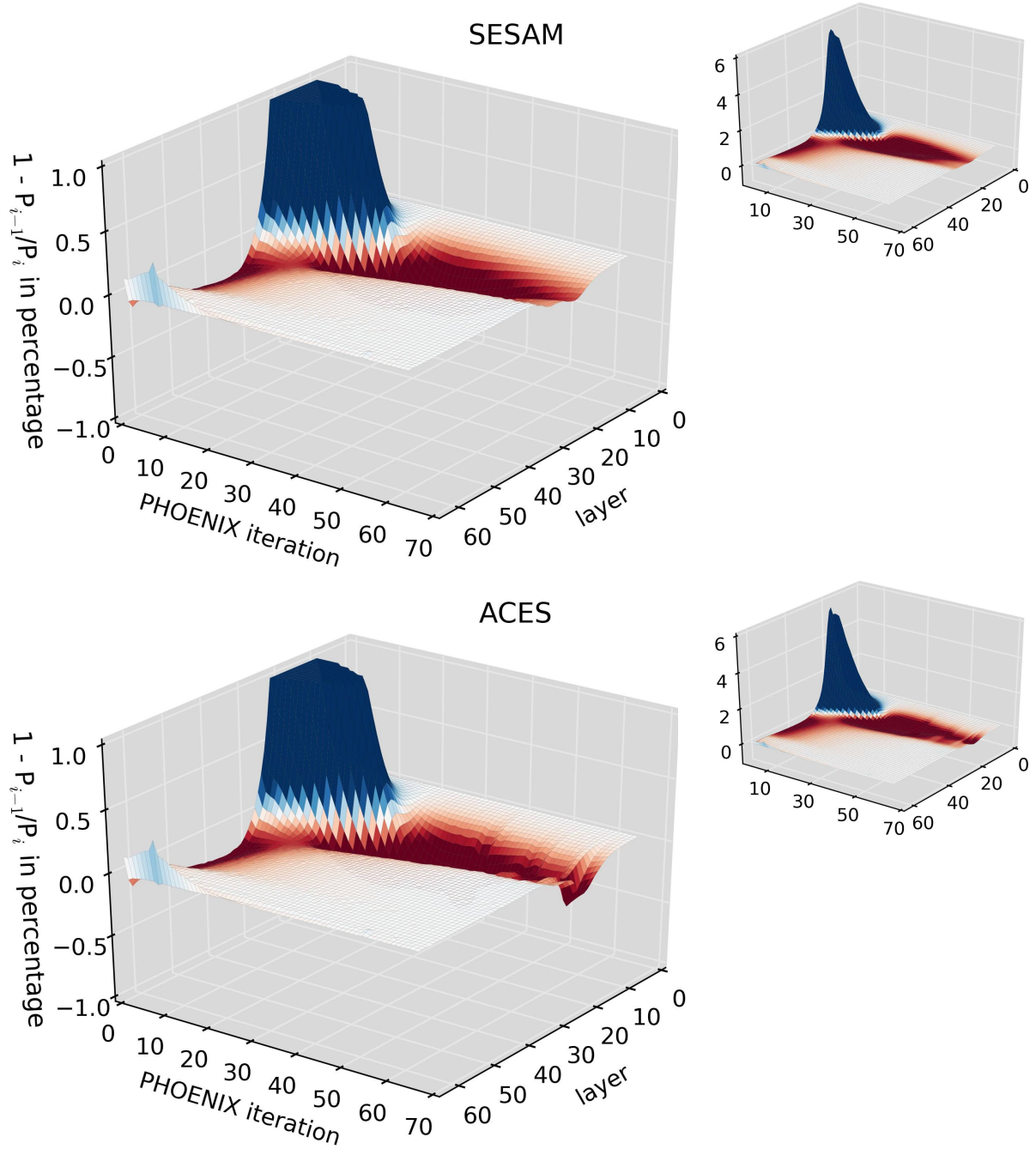


Figure 5.9: Same as in Fig. 5.2 but for a $T_{\text{eff}} = 10000$ K and $\log(g) = 4$ model.

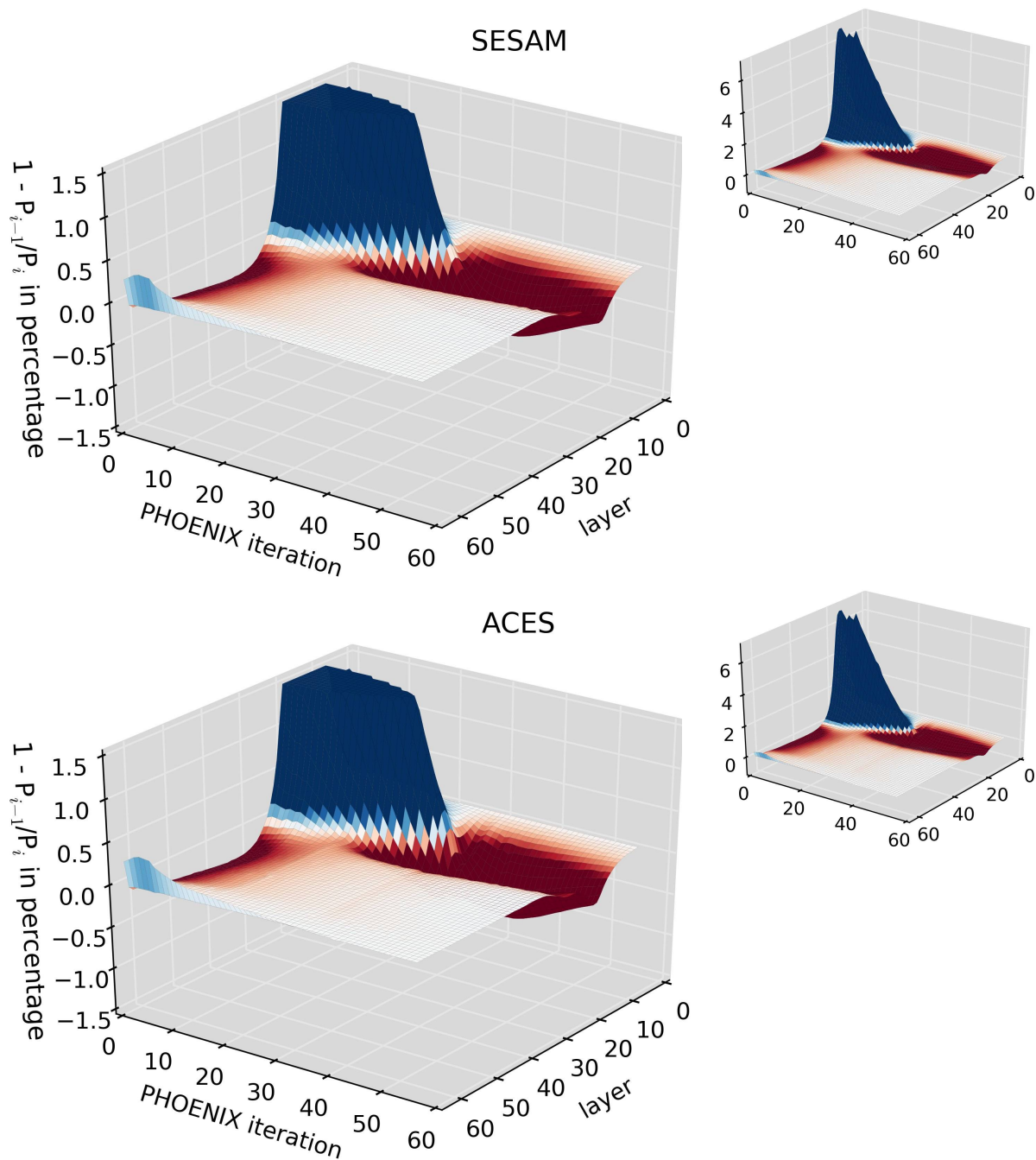


Figure 5.10: Same as in Fig. 5.2 but for a $T_{\text{eff}} = 10000$ K and $\log(g) = 5$ model.

pressure variations within the atmosphere from one PHOENIX iteration to another. This demonstrates that it reliably finds stable solutions for slight variations in the respective temperature and pressure points.

Considering ACES, the situation is different: in the six atmospheres with effective temperatures of 3000 K and 6000 K, ACES causes fluctuations in the pressures between the PHOENIX iterations. These jumps in the pressure changes are located in the lower single-digit percentage range and do not affect the global T - and P -profiles of the converged models.

A possible reason is the existence of not negligible variations in the ACES equilibrium compositions within neighbouring temperature and pressure points, indicating a non proper convergence. In the tested models, this was particularly caused by the consideration of trace species in ACES' iterative process. A general exclusion of minor species with abundances below $1 \cdot 10^{-34}$ mol, as described in Sec. 4.3, results in pressure changes similar to the smooth behaviours from SESAM. The respective ACES plots can be found in the appendix, Figs. 1 - 9. Consequently, SESAM produces more reliable trace abundances than ACES.

This affects primarily the cooler models due to the complex chemistry caused by the large number of molecules present. Because the element abundances are always conserved, a high number of trace species can, therefore, influence the abundances of the other species. This is the reason why the 10000 K ACES models do not show any strong pressure fluctuations: mostly ions and neutral elements are present in the atmosphere, which simplifies the chemistry and makes the treatment of molecules almost negligible.

It can be seen in the 3000 K models in Figs. 5.2 - 5.4 that the upper atmospheric layers do not yet show a convergence considering the pressure structures (whereas PHOENIX stops due to temperature convergence). As mentioned above, these low-density regions involve more complicated physics than the lower, hotter layers, prolonging the convergence process. The effect is independent of the EOS utilised and furthermore a general problem of the simulations.

Figure 5.11 compares the T - and P -profiles of the converged PHOENIX models with $T_{\text{eff}} = 3000$ K and $\log(g) = 3$ where SESAM and ACES were used. For all optical depths, the respective temperatures and pressures are in good agreement with each other. The exclusion of trace species in ACES produces even more consistent results of both EOS's. The maximum temperature and pressure deviations are ~ 0.1 % and ~ 1 %, respectively, located around the 15st layer, indicating that the strongest differences between the chemical compositions of the two EOS's occur here.

This can be seen in Fig. 5.12, where the deviations in the relative concentrations of the three most abundant species atomic hydrogen, helium, and molecular hydrogen are displayed. In this case, the T -profile is mainly affected by deviations in the H concentrations of SESAM and ACES. In the model where ACES skipped the trace species, the H values are in all layers in a better agreement with each other compared to the model where ACES takes all trace species into account. Consequently, the temperature deviations are smaller throughout the atmosphere.

However, this influence does not work in only one direction, it is rather a constant interplay between the atmospheric temperatures and the chemical abundances during the PHOENIX iterations. The initially assumed temperatures result in corresponding chemical equilibria, which, in turn, influence the temperature corrections at the end of the PHOENIX iteration. New temperature values cause new chemical equilibria and so on until the

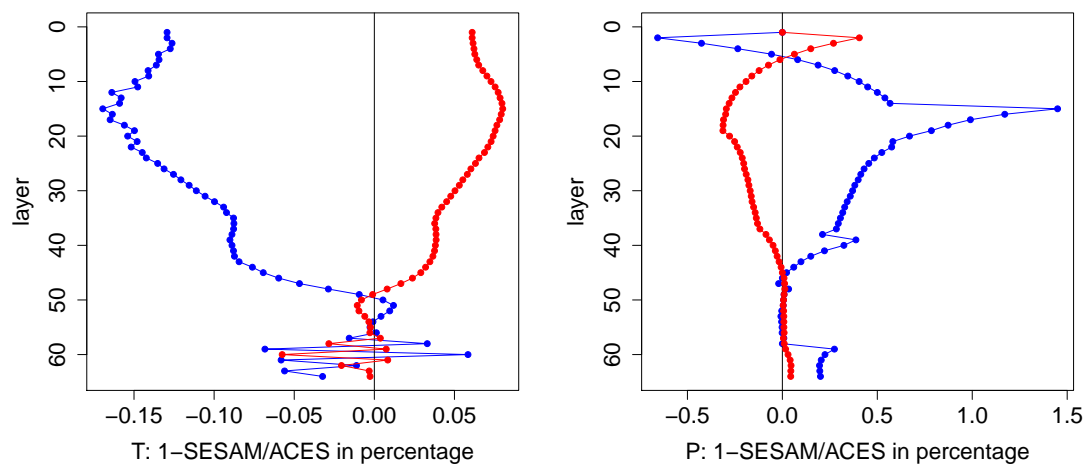


Figure 5.11: Percentage deviations in the final temperature (left) and pressure (right) profiles between SESAM and ACES for the model with $T_{\text{eff}} = 3000$ K and $\log(g) = 3$. In blue are the deviations between the codes when ACES takes trace species into account; in red are the deviations when ACES excludes them.

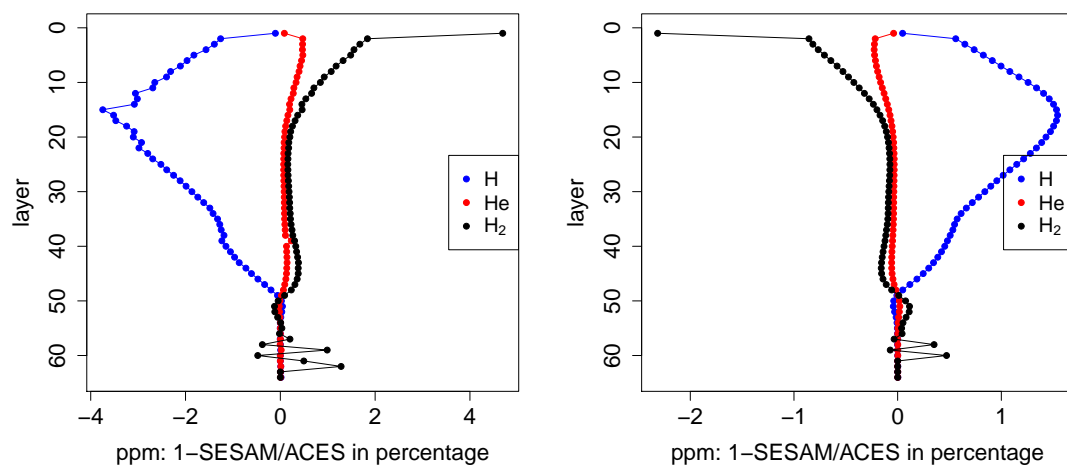


Figure 5.12: Percentage deviations of the relative concentrations (in ppm) of the three most abundant species H, He, and H₂ between SESAM and ACES of the same model of Fig. 5.11. In the left panel, ACES took trace species into account; in the right panel, ACES skipped the trace species.

model is considered converged. EOS's that calculate slight differences in the equilibrium abundances will, therefore, let the model converge to a different atmospheric equilibrium. The decisive quantity in this connection is the temperature and not the pressure: due to the considerable dependence of the chemical potentials on the temperature (see Sec. 3.3), the equilibrium composition and, consequently, the opacities are strongly affected. The pressure, however, is only marginally influencing the chemical abundances (Eq. 3.19).

Figures 5.13 - 5.20 present the differences in the T - and P -profiles of the remaining eight models, which show only minor deviations from each other in all optical depths. Except for the $T_{\text{eff}} = 3000$ K and $\log(g) = 4$ model, the exclusion of trace species in ACES results in even better agreements between both EOS's. The differences in the equilibrium compositions between SESAM and ACES are, therefore, sufficiently low to not significantly affect the temperature and pressure profiles.

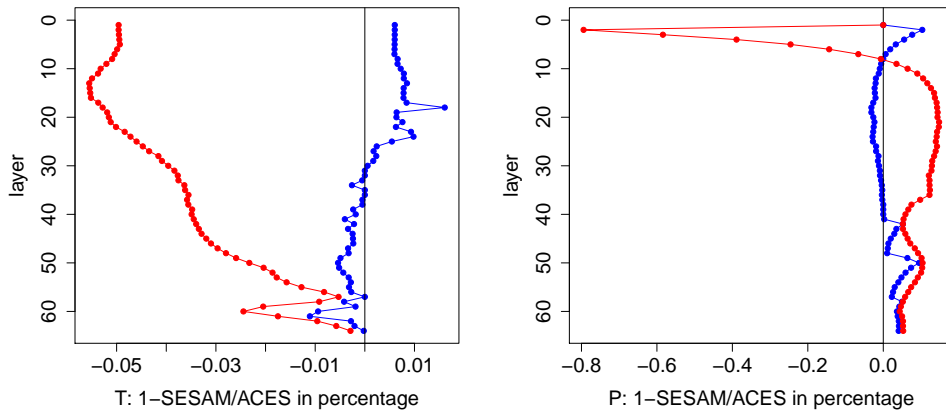


Figure 5.13: Same as in Fig 5.11 but for a $T_{\text{eff}} = 3000$ K and $\log(g) = 4$ model.

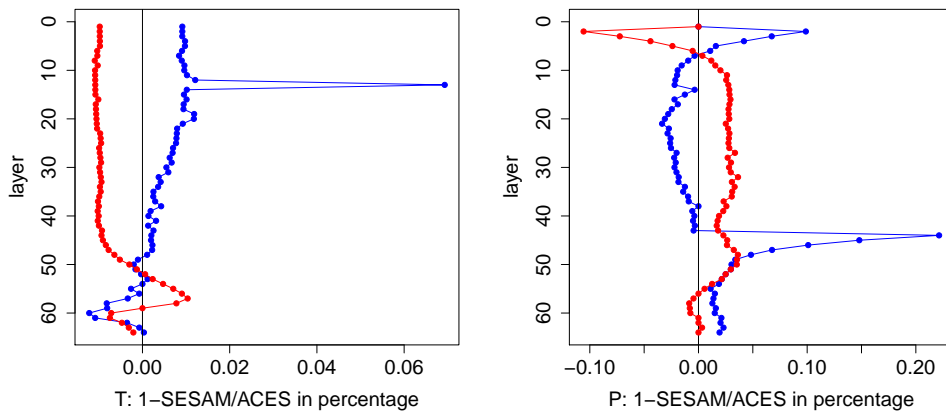


Figure 5.14: Same as in Fig 5.11 but for a $T_{\text{eff}} = 3000$ K and $\log(g) = 5$ model.

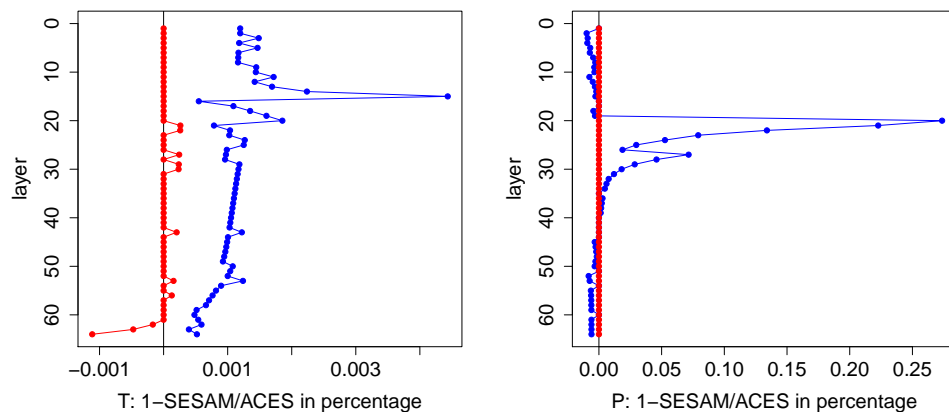


Figure 5.15: Same as in Fig 5.11 but for a $T_{\text{eff}} = 6000$ K and $\log(g) = 3$ model.

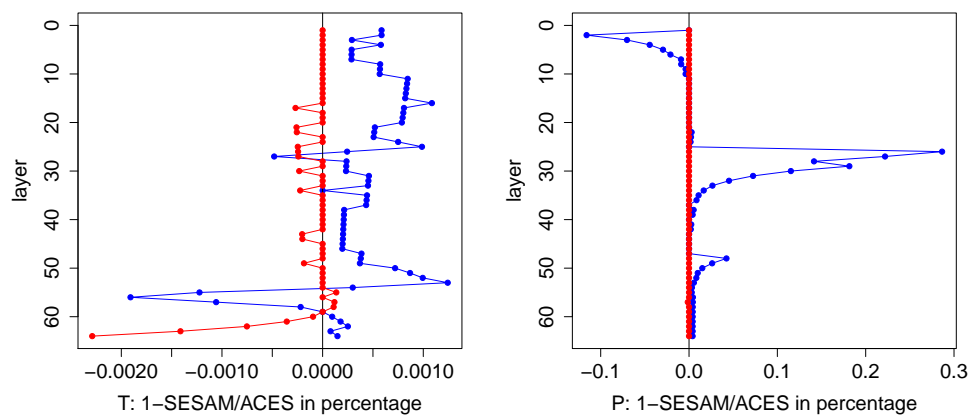


Figure 5.16: Same as in Fig 5.11 but for a $T_{\text{eff}} = 6000$ K and $\log(g) = 4$ model.

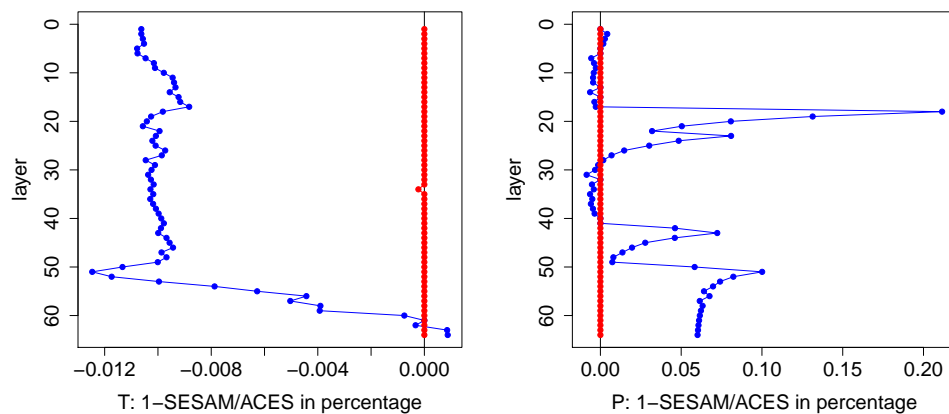


Figure 5.17: Same as in Fig 5.11 but for a $T_{\text{eff}} = 6000$ K and $\log(g) = 5$ model.

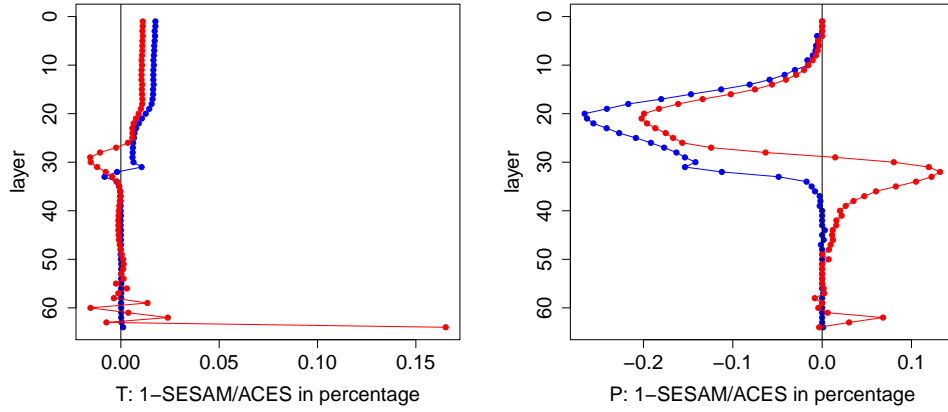


Figure 5.18: Same as in Fig 5.11 but for a $T_{\text{eff}} = 10000$ K and $\log(g) = 3$ model.

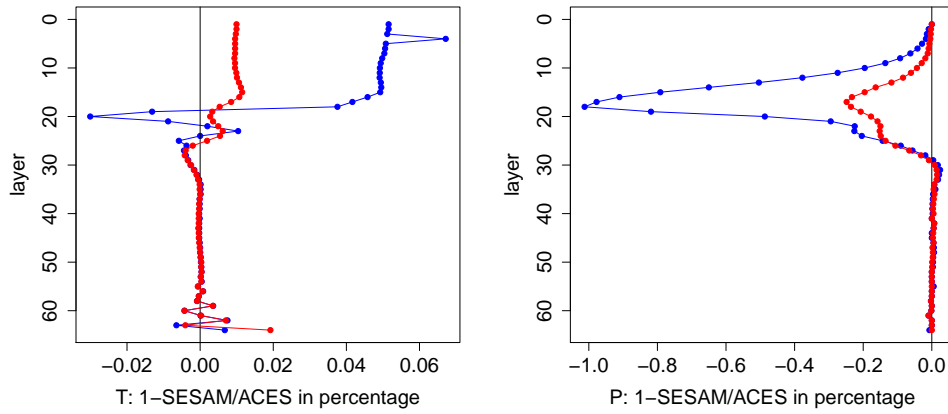


Figure 5.19: Same as in Fig 5.11 but for a $T_{\text{eff}} = 10000$ K and $\log(g) = 4$ model.

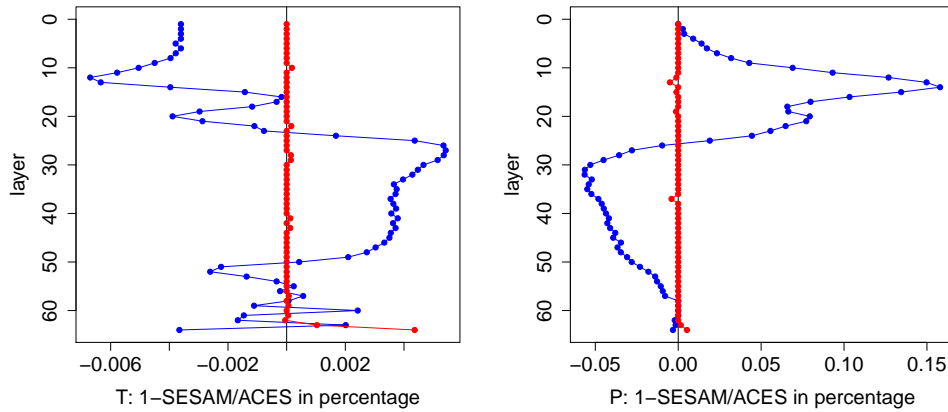


Figure 5.20: Same as in Fig 5.11 but for a $T_{\text{eff}} = 10000$ K and $\log(g) = 5$ model.

5.2 Spectrum

PHOENIX is a radiative transfer focused code, which produces as central result the spectrum of the simulated star. The EOS is in this regard crucial for the simulations. Each spectral line depends on the opacities of individual species and, therefore, on the chemical abundances in the atmosphere. In this section, the spectra of the nine models in Sec. 5.1 are discussed. Each model was calculated with the help of **SESAM** and **ACES**, taking minor species into account. The deviations between the fluxes f_λ were determined according to $1 - f_{\lambda,\text{SESAM}}/f_{\lambda,\text{ACES}}$ for all wavelengths λ from 1 nm to $5 \cdot 10^4$ nm.

Figure 5.21 shows the discrepancies between three exemplary fluxes of models with effective temperatures of 3000 K, 6000 K, and 10000 K with a $\log(g) = 4$. The $\log(g)$ of 3 and 5 cases show similar behaviours compared to the $\log(g) = 4$ models. The spikes are corresponding to differences in the spectral lines.

A full list of all nine model spectra is presented in Table 5.1. To quantify the deviations, the absolute values of $1 - f_{\lambda,\text{SESAM}}/f_{\lambda,\text{ACES}}$ were integrated and normalised on the following wavelength intervals: the ultraviolet (1 nm - 380 nm), optical (380 nm - 780 nm), near-infrared (780 nm - 3 μm), and mid-infrared (3 μm - 50 μm) ranges.

model:		deviation in percentage:			
T_{eff}	$\log(g)$	UV	optical	NIR	MIR
3000 K	3	6.5	$3.7 \cdot 10^{-1}$	$8.8 \cdot 10^{-2}$	$6.0 \cdot 10^{-2}$
3000 K	4	$3.8 \cdot 10^{-1}$	$2.7 \cdot 10^{-1}$	$8.5 \cdot 10^{-2}$	$1.0 \cdot 10^{-2}$
3000 K	5	$3.1 \cdot 10^{-1}$	$6.5 \cdot 10^{-2}$	$5.5 \cdot 10^{-2}$	$2.2 \cdot 10^{-2}$
6000 K	3	$8.1 \cdot 10^{-2}$	$3.2 \cdot 10^{-3}$	$1.2 \cdot 10^{-3}$	$1.6 \cdot 10^{-3}$
6000 K	4	$4.9 \cdot 10^{-2}$	$1.8 \cdot 10^{-3}$	$4.6 \cdot 10^{-4}$	$5.7 \cdot 10^{-4}$
6000 K	5	$5.8 \cdot 10^{-1}$	$6.9 \cdot 10^{-2}$	$1.4 \cdot 10^{-2}$	$7.7 \cdot 10^{-3}$
10000 K	3	$2.6 \cdot 10^{-1}$	$9.3 \cdot 10^{-4}$	$1.1 \cdot 10^{-3}$	$1.1 \cdot 10^{-3}$
10000 K	4	$3.0 \cdot 10^{-1}$	$3.4 \cdot 10^{-4}$	$6.2 \cdot 10^{-4}$	$8.9 \cdot 10^{-4}$
10000 K	5	$1.0 \cdot 10^{-1}$	$1.0 \cdot 10^{-3}$	$1.3 \cdot 10^{-3}$	$3.4 \cdot 10^{-3}$

Table 5.1: Absolute values of the percentage deviations between the spectra of the models where either **SESAM** or **ACES** were used, normalised on the ultraviolet (1 nm - 380 nm), optical (380 nm - 780 nm), near-infrared (780 nm - 3 μm), and mid-infrared (3 μm - 50 μm) wavelength intervals.

For the 3000 K and 6000 K models, the largest deviations in the f_λ occur in the ultraviolet and optical wavelengths, indicating that the equilibrium composition of neutral and ionised atoms, and molecules of the two EOS's are differing from each other. The smallest deviations are found in the near- and mid-infrared where the differences between **SESAM**- and **ACES**-based lines are weaker and the continuum is dominating the spectrum. The respective opacities of the species are in a better agreement with each other there. Exception from this are the $T_{\text{eff}} = 10000$ K models: here, the best match is located in the optical. The opacity in low effective temperature objects is dominated by neutral atoms and especially molecules. Differences amongst the EOS's are more pronounced in the 3000 K model than in the solar-like 6000 K model. Except for the $\log(g) = 5$ model, this effect arises for all other tested surface gravities over all wavelengths: at 3000 K, the deviations are ranging from 6.5 % to $\sim 10^{-2}$ %, and at 6000 K from $\sim 10^{-1}$ % to $\sim 10^{-4}$ %. With

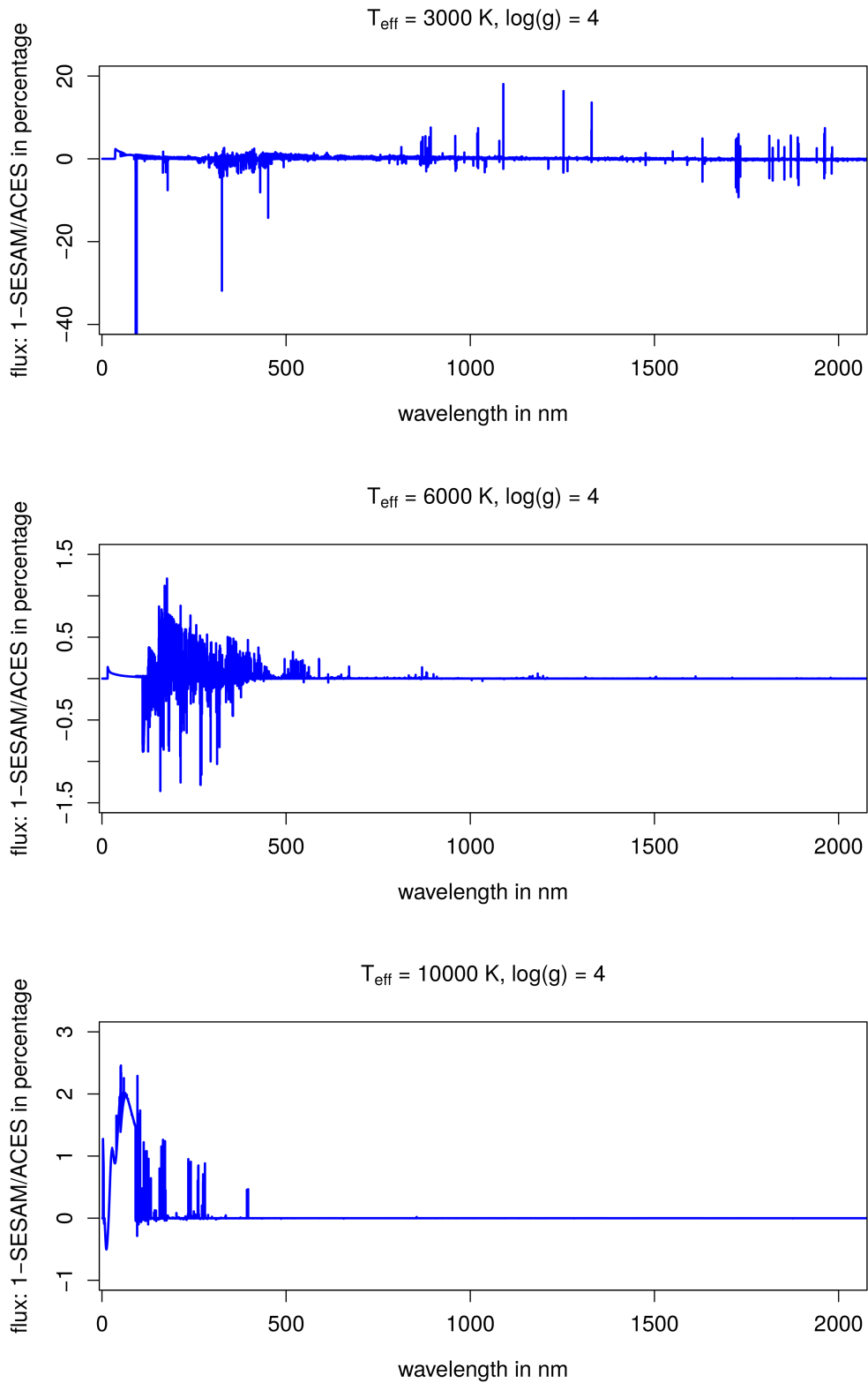


Figure 5.21: Flux deviations between the application of SESAM and ACES on the respective model atmosphere flux spectra.

increasing effective temperature, the strength of molecular lines decreases and ionisation emerges. For 10000 K, mostly ions and neutral atomic species are affecting the flux. Here, the deviations are ranging from $\sim 10^{-1}$ % to $\sim 10^{-4}$ %.

Although the application of the two EOS's causes differences in the final fluxes, the compared spectra deviate only marginally from each other.

5.3 Initial species abundances

The system, for which the EOS modules **ACES** and **SESAM** determine the equilibrium composition, is completely defined by temperature, pressure, element abundances and a list of species. Both EOS's are guessing initial abundances for the species to accelerate their iterative processes. **ACES** uses pre-computed partial pressure tables (Sec. 4.2), whereby **SESAM** calculates them on the fly via a simplex method (Sec. 4.1). In all cases, the equilibrium composition must be independent from the values of the initial species abundances. This is an indispensable condition for a reasonable EOS. Therefore, a model atmosphere, calculated with variations in these guessed abundances, should never differ regarding the atmospheric temperature and pressure profiles and the flux.

To investigate this, the model with $T_{\text{eff}} = 6000$ K and $\log(g) = 4$ was recalculated with **ACES** but, this time, using partial pressure tables of a sub-solar metallicity of -2 . Unchanged is the assumption that the atmosphere contains solar element abundances, i.e., $[M/H] = 0$. Consequently, **ACES** estimates initial abundances that deviate stronger from the equilibrium ones than in the original test case where a table with solar species abundances was used. At first, all trace species are taken into account.

As a result, **PHOENIX** reached temperature convergence even faster than previously, namely within 57 iterations instead of 60. However, the final pressure profiles are not identical. The changes in pressures of the model with $[M/H] = -2$ are presented in Fig. 5.22, which differ to the one with solar abundances (Fig. 5.6). The pressure fluctuations are particularly significant between layer 13 and 43 and occur until the last **PHOENIX** iteration, making a stable solution of the atmospheric pressure profile questionable. The figure demonstrates the influence of inconsistently calculated trace species on the atmospheric pressure structures. Compared to the upper layers, the lower regions are warmer and less molecules contribute to the total opacity. In the higher, cooler layers, molecules are more likely abundant. Here, the interplay between the abundant molecules and the trace molecules has a significant impact on the resulting equilibrium abundances due to the conservation of element abundances. This manifests in the pressure fluctuations between layer 13 and 43. In fact, a direct comparison between the two converged **ACES** models, based on $[M/H] = 0$ and $[M/H] = -2$ partial pressure tables, shows deviations in these layers (see Fig. 5.23). An application of other partial pressure tables with metallicities of -1 and -3 show similar results.

The situation is different when **ACES** uses the table of $[M/H] = 1$. This model had not converged after 160 **PHOENIX** iterations. An eventual convergence could not be expected. This can be seen in Fig. 5.24: the profile of the changes in temperature shows an oscillation across all layers until the end of iteration 160. It contrasts with the original model, calculated with the $[M/H] = 0$ table, where convergence was achieved within 60 iterations.

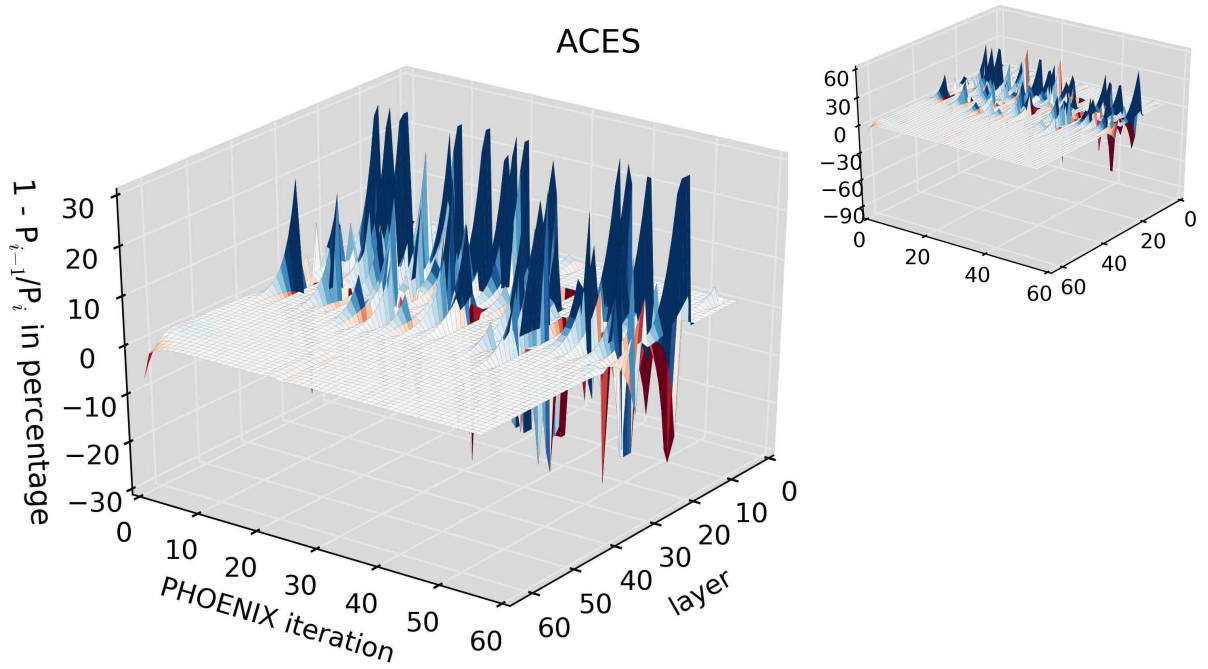


Figure 5.22: Changes in pressure between the i^{th} iteration of PHOENIX, P_i , and the previous iteration, P_{i-1} , for each atmospheric layer and each PHOENIX iteration of a $T_{\text{eff}} = 6000$ K and $\log(g) = 4$ model with solar element abundances but using the partial pressure table with a metallicity of -2 as starting species abundances for ACES. The left panel is the reduced scale of the full-scale representation on the right side, using identical axes.

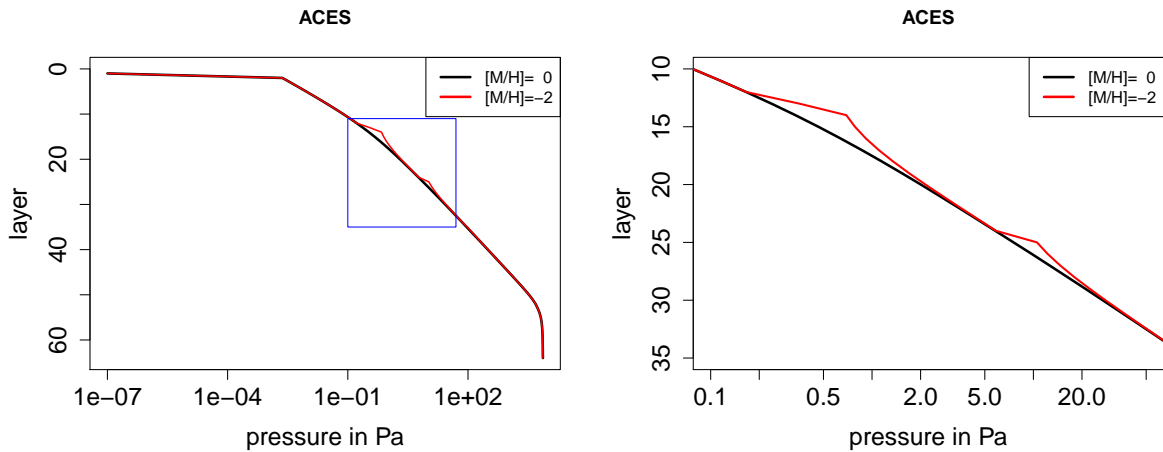


Figure 5.23: The final atmospheric pressure profiles of two converged models of a star with $T_{\text{eff}} = 6000$ K, $\log(g) = 4$ and solar element abundances. Both atmospheres are calculated using ACES but different partial pressure tables to generate initial guesses (of $[M/H] = 0$ and $[M/H] = -2$) are applied. The right panel represents the area within the blue box in the left panel.

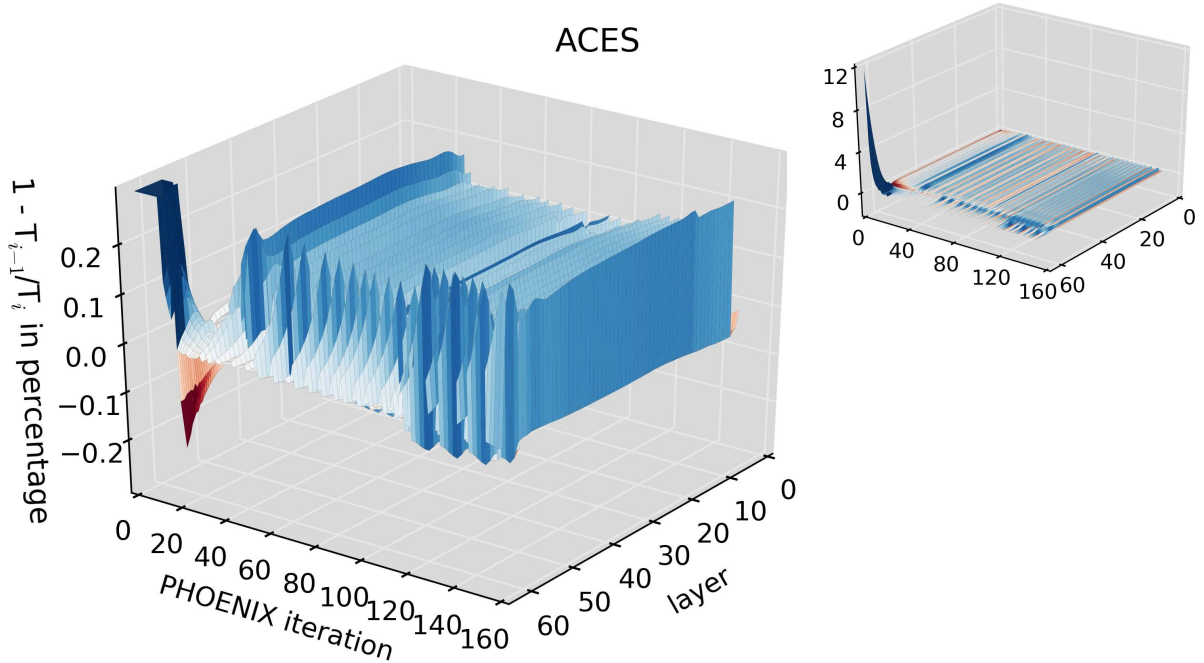


Figure 5.24: Changes in temperature between the i^{th} iteration of PHOENIX, T_i , and the previous iteration, T_{i-1} , for each atmospheric layer and each PHOENIX iteration of a $T_{\text{eff}} = 6000$ K and $\log(g) = 4$ model with solar element abundances but using the partial pressure table with a metallicity of $[M/H] = 1$ as initial species abundances for ACES. The left panel is the reduced scale of the full-scale representation on the right side, using identical axes.

ACES' sensitivity considering the initial species abundances strongly indicates the existence of pseudo-convergence. If this occurs in the close proximity of the true physical equilibrium composition, instabilities in the solution will arise. This explains, for instance, the almost periodical changes in temperatures during the PHOENIX iterative process (Fig. 5.24). The model alternates between an increase and a decrease in temperatures, i.e., from an atmosphere with a lack in energy to one with an excess in energy. There is no trend towards a conservation of energy and, directly coupled with this, a reduction of the temperature correction at the end of each iteration. PHOENIX tries to approach the solution of a converged model one time from a too high temperature and the other time from a too low temperature, oscillating around the physical solution. However, in both cases, the EOS results may vary slightly more than they physically would, causing a permanent overcorrection of the temperatures.

These issues are in particular an effect of the inclusion of minor species in the equilibrium problem. It demonstrates ACES' difficulties in constructing a reliable stoichiometric matrix when many trace species are taken into account, making the solution depending on the initial species abundances. Like in Sec. 5.1, a recalculation with ACES, but excluding the trace species from the closer consideration, influences significantly the behaviour of the simulations: no pressure fluctuations are present in the models where sub-solar metallicity tables were applied (Fig. 10 in the appendix), and the model with the $[M/H] = 1$ table converges straightforwardly after 60 PHOENIX iterations. In these cases, there is no affect of the initial species abundances on the equilibrium compositions.

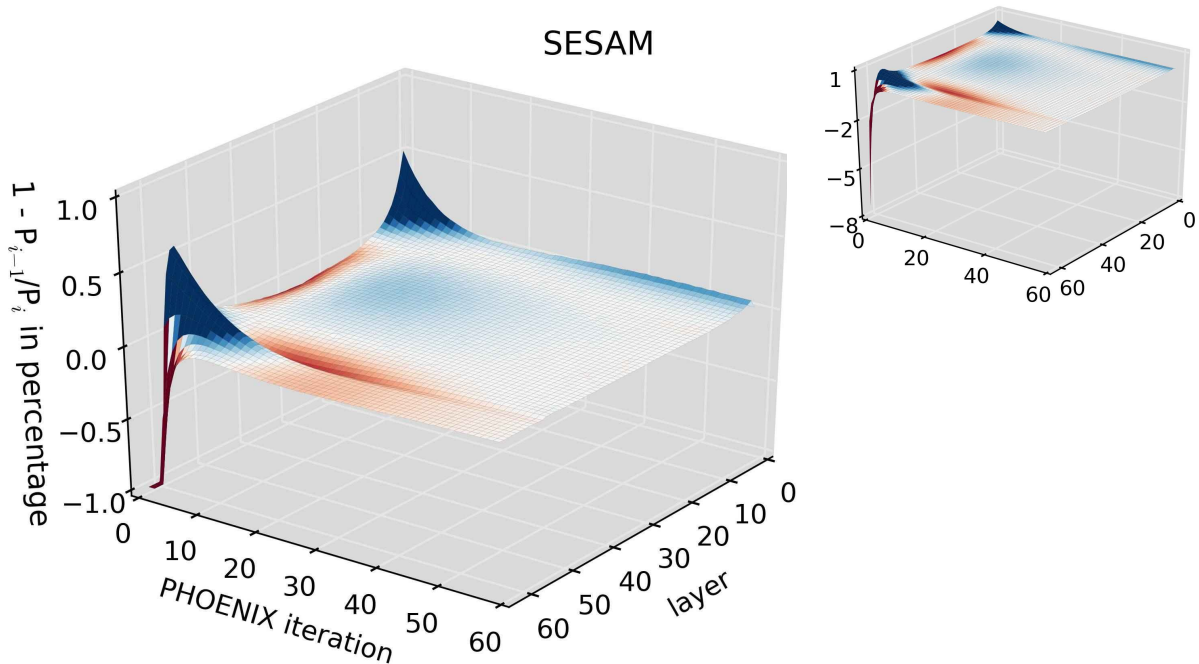


Figure 5.25: Changes in pressure between the i^{th} iteration of PHOENIX, P_i , and the previous iteration, P_{i-1} , for each atmospheric layer and each PHOENIX iteration of a $T_{\text{eff}} = 6000$ K and $\log(g) = 4$ model with solar abundances, calculated with the help of SESAM and initial species abundances in accordance with $[M/H] = -40$. The left panel is the reduced scale of the full-scale representation on the right side, using identical axes. These plots are exemplary: all models show identical results, independently whether metallicities of $-40, -20, -2, 0, 1, 20$, or 40 were applied.

The problems mentioned above do not arise when SESAM is used: the application of a partial pressure table is not required because it calculates initial abundances on the fly and, moreover and of particular importance, the determined equilibrium is always insensitive to the quality of these initial abundances. This can be shown under similar conditions compared to the ACES tests presented above. In order to realise this, SESAM was modified to determine the initial species values from the element abundances of arbitrary metallicities. However, the basic assumption of solar element abundances in the further calculation was unchanged. Not only the previous samples with $[M/H]$ of $-2, 0$, and 1 were tested but also non-physical metallicities of $-40, -20, 20$, and 40 were considered to test SESAM's robustness.

In each of these six cases, PHOENIX converged within 60 iterations. Furthermore, all models show exactly the same particular smooth behaviours regarding the changes in pressure (Fig. 5.25) and temperature (equal convergence behaviour as presented in Fig. 5.1). The resulting pressure profiles of the model atmospheres are identical across the sampled optical depth.

Consequently, and in contrast to ACES, SESAM's equilibrium compositions are not affected by the initial species abundances. They merely serve their one purpose within SESAM: an acceleration of the calculation time. How strongly the quality of the initial abundances influence the total number of SESAM iterations, required for one exemplary PHOENIX iteration, is shown in Fig. 5.26. For each test case, one additional PHOENIX iteration was calculated on top of a converged model with $T_{\text{eff}} = 6000$ K, $\log(g) = 4$, and solar element abundances. The initial abundances were varied by modifying the metallicities

assumed for **SESAM**'s initial estimate, using nine different values from $[M/H] = -40$ to $[M/H] = 40$. The plot displays the sum of the **SESAM** iterations required to determine the respective equilibrium compositions for all T - and P -points occurring during the **PHOENIX** iteration. In each case, **PHOENIX** executed the EOS 1154 times. Also presented in Fig. 5.26 is the mean number of **SESAM** iterations per each EOS call. For the negative metallicities of -20 , -30 , and -40 , all metals are assumed to be present only in small traces, namely, the respective element abundances are below $1 \cdot 10^{-24}$ mol when applying $[M/H] = -20$ and below $1 \cdot 10^{-44}$ mol for $[M/H] = -40$. This essentially complicates the equilibrium determination because the initial abundances are deviating strongly from the equilibrium state, prolonging **SESAM**'s iterative process. The situation is different for the positive metallicities: the initial species are significantly more abundant and, consequently, the equilibrium problem is more constrained and the solution can be found more straightforwardly. Regarding the continuously low total (and mean) number of iterations for all positive metallicities, **SESAM** handles initial species abundances that are above the equilibrium abundances without losing any efficiency in calculating the equilibria. Even with $[M/H] = -10$, the number of iterations compared to the $[M/H] = 0$ case does not increase.

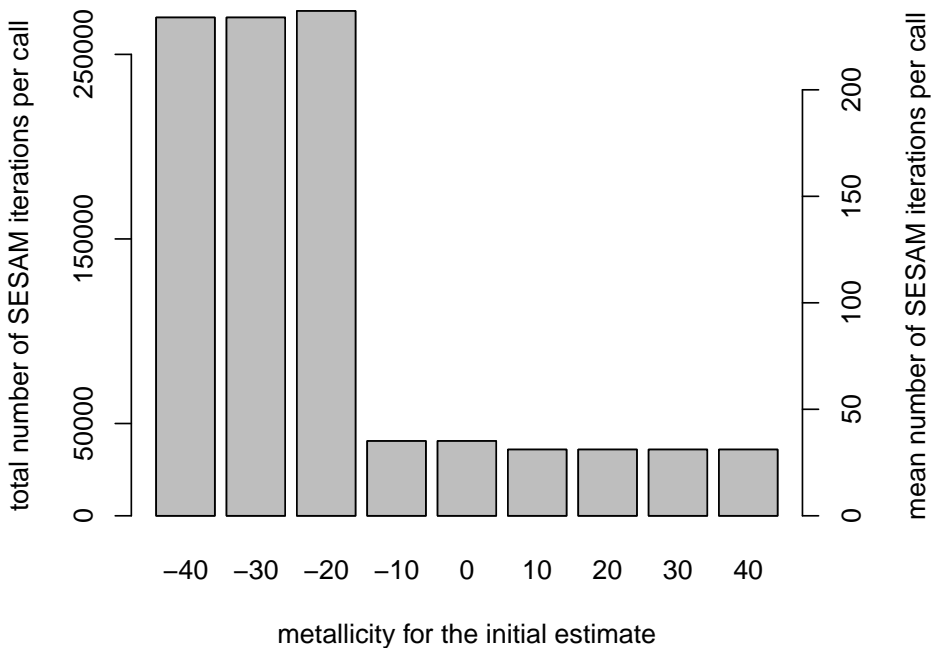


Figure 5.26: Total number and mean number of **SESAM** iterations for one **PHOENIX** iteration of the same model with $T_{\text{eff}} = 6000$ K, $\log(g) = 4$, and solar element abundances. Nine different element metallicities were considered for the initial estimate of the species abundances. In each case, **PHOENIX** called the EOS 1154 times.

5.4 Further model atmospheres

Sub-solar metallicity

In contrast to the previous atmospheres tested, now, a metal-poor star with a sub-solar metallicity of $[M/H] = -2$ was modelled instead of assuming solar element abundances. The object has $T_{\text{eff}} = 3000$ K and $\log(g) = 4$ and was calculated by the means of **SESAM** and **ACES**. This low effective temperature was chosen to ensure a complex system with a particular contribution of molecules and neutral elements to the opacities. By using a partial pressure table of $[M/H] = -2$, **ACES** was provided the best possible initial species abundances. As usual, **SESAM** determined these abundances on the fly by applying a simplex method.

With **SESAM**, **PHOENIX** converged after 90 iterations, and with **ACES** after 91. The final atmospheric pressure profiles differ only slightly from each other with a maximum deviation of 0.3 % (right panel in Fig. 5.27). However, a closer look to the changes in pressure during the **PHOENIX** iterative process in Fig. 5.28 reveals a significant difference between the two EOS's: like in all previously cases tested, **SESAM** shows a smooth behaviour throughout all **PHOENIX** iterations and optical depths, whereby **ACES** causes strong fluctuations of the changes in pressure from one iteration to the next. These jumps occur even until the model converged, which makes a stable solution uncertain. As in the previous test cases, this is caused by inconsistently calculated trace species. A recalculation of the model, but with minor species skipped, does not show these pressure fluctuations (Fig. 11 in the appendix).

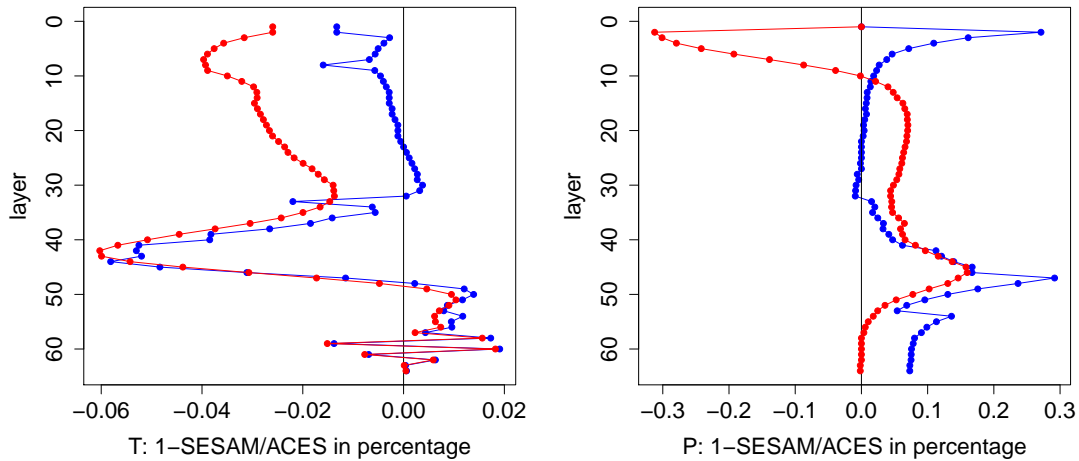


Figure 5.27: Percentage deviations in the final temperature (left) and pressure (right) profiles between **SESAM** and **ACES** for a model with $T_{\text{eff}} = 3000$ K, $\log(g) = 4$, and $[M/H] = -2$. In blue are the deviations between the codes when **ACES** takes trace species into account; in red are the deviations when **ACES** excludes them.

A good agreement between the two EOS's is found in the atmospheric temperature profile: the maximum deviation of all optical depths is $-6 \cdot 10^{-2}$ % around layer 44 (Fig. 5.27), regardless whether **ACES** skipped or included trace species in the calculation. A comparison

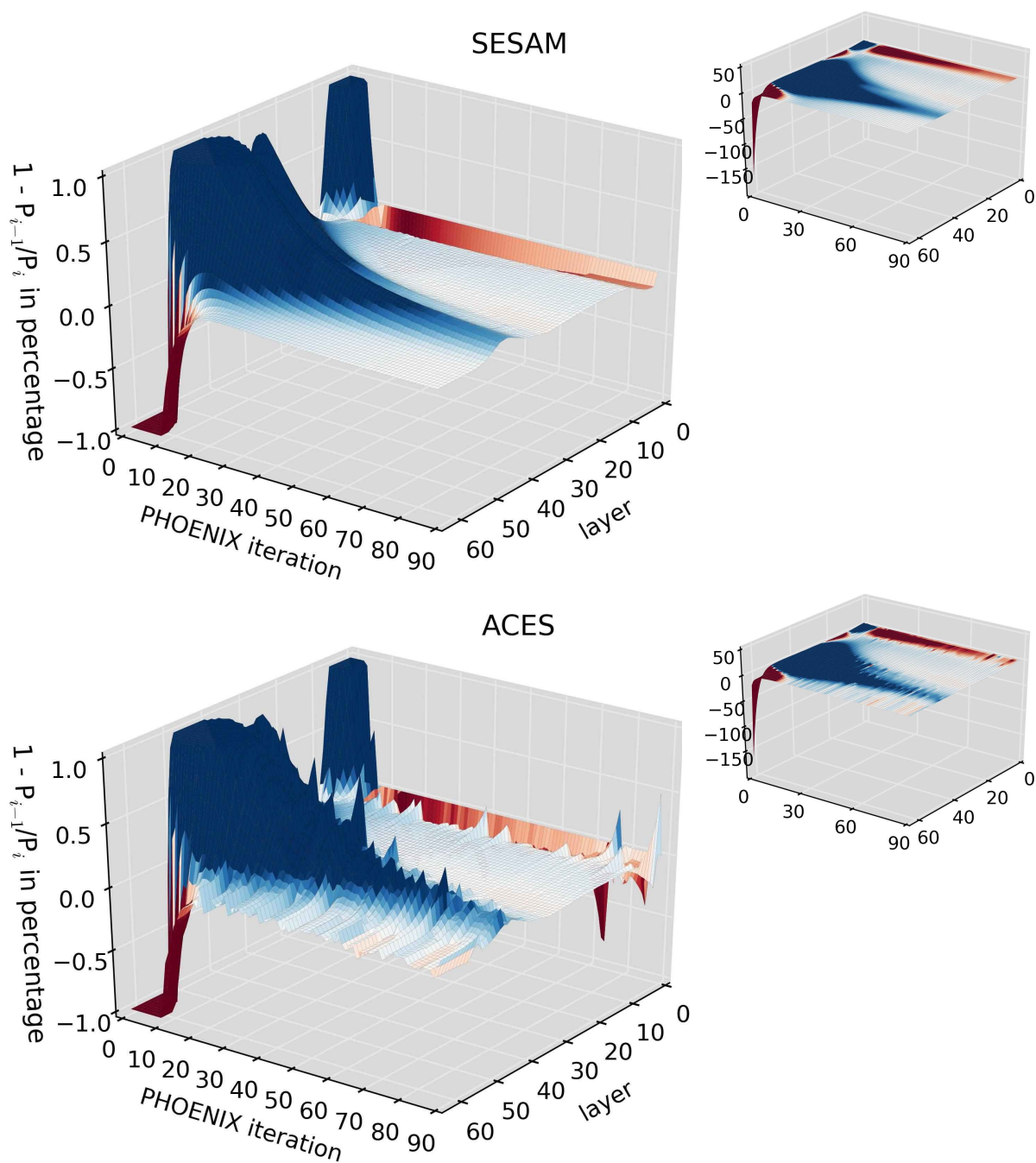


Figure 5.28: Changes in pressure between the i^{th} iteration of PHOENIX, P_i , and the previous iteration, P_{i-1} , for each atmospheric layer and each PHOENIX iteration of a $T_{\text{eff}} = 3000$ K and $\log(g) = 4$ model with $[M/H] = -2$. The left panels are the reduced scale of the full-scale representations on the right side, using identical axes. SESAM and ACES were applied for the top and bottom panels, respectively.

of the relative concentrations of three most abundant species atomic hydrogen, helium, and molecular hydrogen in Fig. 5.29 shows the direct correlation of the deviations in the hydrogen concentrations between **SESAM** and **ACES** to the deviation in the T -profiles. Considering the changes in temperature after each **PHOENIX** iteration for all optical depths, both EOS's are producing a straightforward convergence without any strong fluctuations. The deviations of the respective spectra are $7.0 \cdot 10^{-1} \%$ in the ultraviolet, $1.8 \cdot 10^{-1} \%$ in the optical, $9.2 \cdot 10^{-2} \%$ in the near-infrared, and $3.0 \cdot 10^{-2} \%$ mid-infrared spectral ranges. With respect to the spectrum, the difference between **SESAM** and **ACES** is irrelevant. Nevertheless, the deviations in the UV, NIR, and MIR are somewhat greater than in the model where a solar metallicity was assumed. This is due to the better agreement of the final T - and P -profiles between **SESAM** and **ACES**: in the $[M/H] = 0$ model, their maximum deviations are only 0.01 % and 0.1 %, respectively (Fig. 5.13). As described in Sec. 5.1, the temperature values are decisive in this connection due to the significant dependence of the chemical potentials on the temperatures.

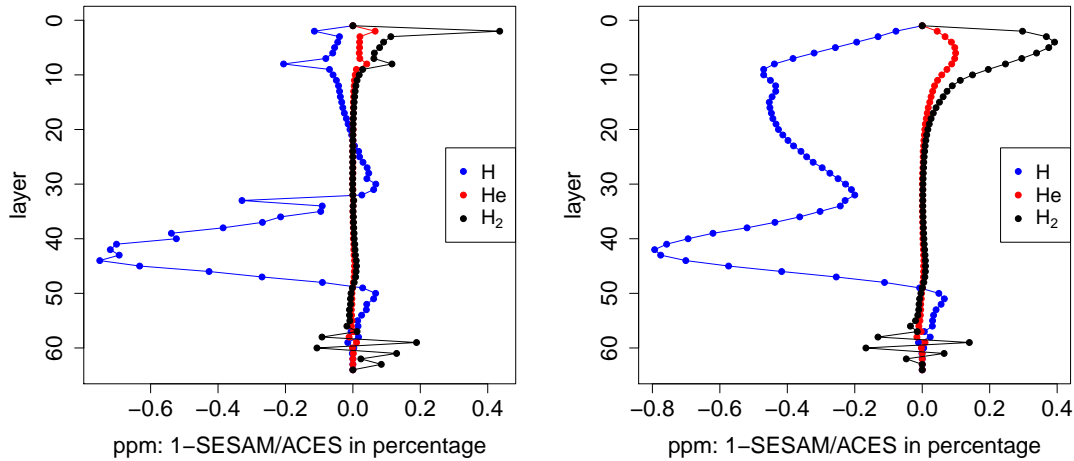


Figure 5.29: Percentage deviations of the relative concentrations (in ppm) of the three most abundant species H, He, and H_2 between **SESAM** and **ACES** of the same model of Fig. 5.27. In the left panel, **ACES** took trace species into account; in the right panel, **ACES** skipped the trace species.

Species in non-local thermodynamic equilibrium

The non-local thermodynamic equilibrium is an important state, as mentioned in Sec. 2.2.1. Considering the EOS, the only relevant difference between LTE and NLTE are the chemical potentials of the respective species provided by **PHOENIX**. The following test case is a star with an effective temperature of 6000 K and a surface gravity $\log(g)$ of 4. Furthermore, hydrogen and helium are present in NLTE.

The inclusion of **SESAM** brings about a straightforward convergence, analogously to Fig. 5.1. There are only marginal changes in the pressures between each **PHOENIX** iteration for all atmospheric layers, indicating a reliable final P -profile (Fig. 5.30). The application of **ACES** causes strong pressure fluctuations during the whole iterative process, as displayed in Fig. 5.30.

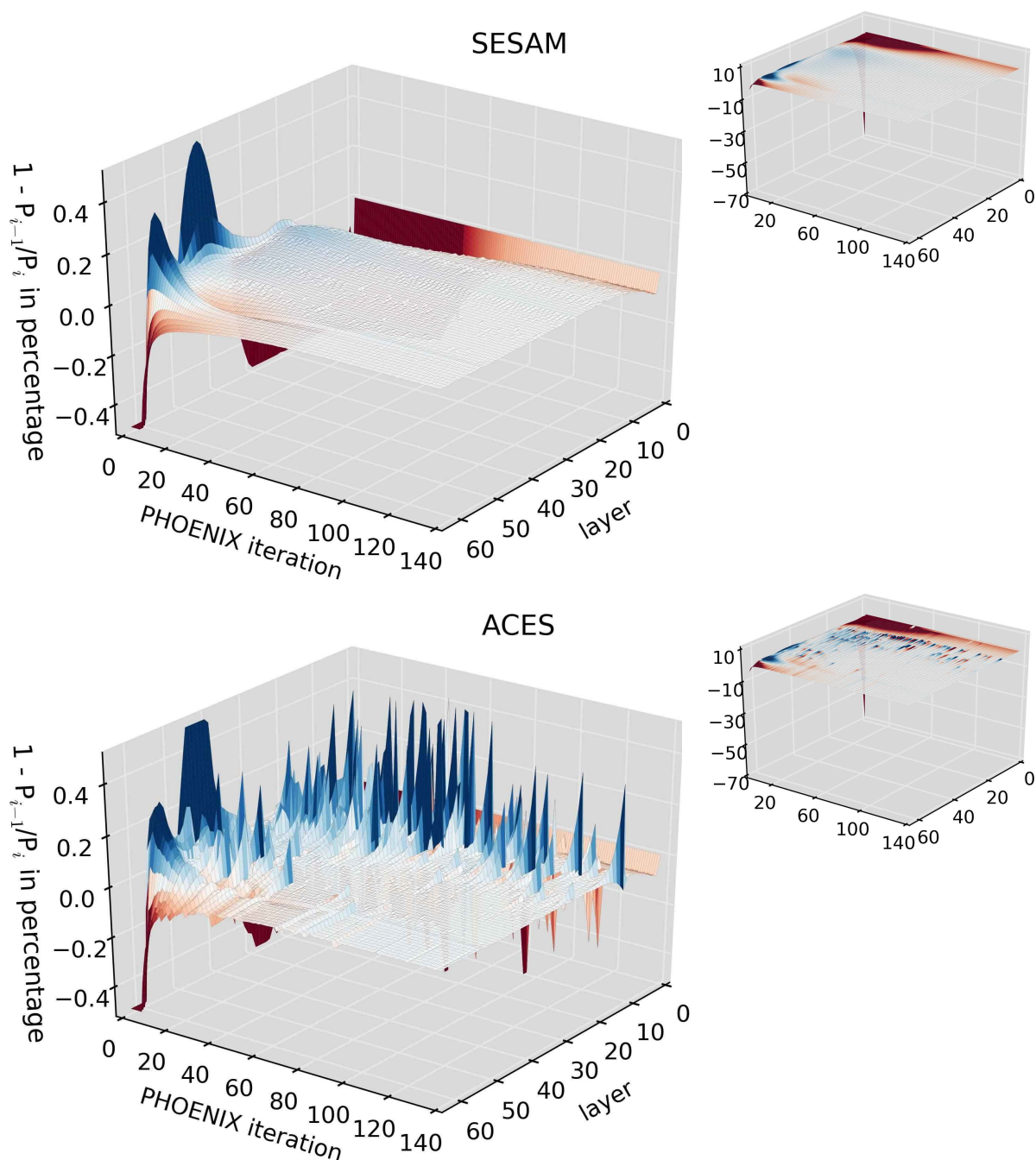


Figure 5.30: Changes in pressure between the i^{th} iteration of PHOENIX, P_i , and the previous iteration, P_{i-1} , for each atmospheric layer and each PHOENIX iteration of a $T_{\text{eff}} = 6000$ K and $\log(g) = 4$ model with solar abundances, assuming the species H and He being treated in NLTE. The left panels are the reduced scale of the full-scale representations on the right side, using identical axes. SESAM and ACES were applied for the top and bottom panels, respectively.

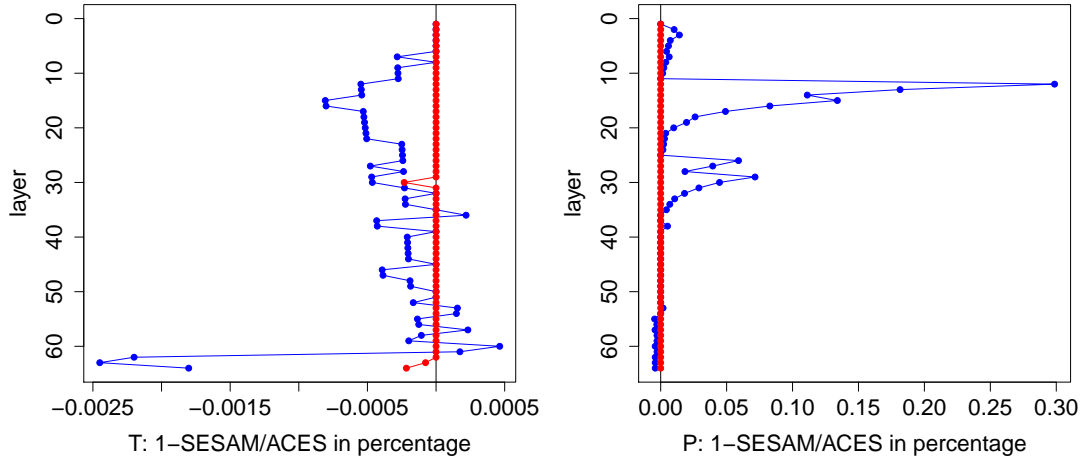


Figure 5.31: Percentage deviations in the final temperature (left) and pressure (right) profiles between **SESAM** and **ACES** for a model with $T_{\text{eff}} = 6000$ K and $\log(g) = 4$, assuming H and He being treated in NLTE. In blue are the deviations between the codes when **ACES** takes trace species into account; in red are the deviations when **ACES** excludes them.

Although the model is converged, the outer layers from 12 to 33 display instabilities regarding the pressure values, namely at optical depths from $\tau_{\text{std},12} = 8.6 \cdot 10^{-9}$ to $\tau_{\text{std},33} = 1.0 \cdot 10^{-4}$. Analogously to Fig. 5.22, the location of the fluctuations in Fig. 5.30 reveals that the inconsistently calculated minor species significantly influence the abundant molecules and, therefore, the atmospheric pressures in these layers.

In fact, comparing the resulting final pressure profile of **ACES** with **SESAM**, the pressures deviate mostly in these layers with ~ 0.1 %. This is shown in Fig. 5.31, along with the respective temperature profile.

The situation is different when **ACES** excludes trace species from the equilibrium problem: the pressure fluctuations do not appear (Fig. 12 in the appendix) and the final P -profile does not show any deviations from the one where **SESAM** was utilised.

The equilibrium abundances are in such a good agreement with each other that the T -profiles show a maximum deviation of only $\sim 10^{-3}$ %. The deviations of the resulting spectra are particularly low: $8.9 \cdot 10^{-3}$ % in the UV, $1.7 \cdot 10^{-4}$ % in the optical, $2.0 \cdot 10^{-4}$ % in the near-infrared, and $7.1 \cdot 10^{-5}$ % in the mid-infrared.

Convection

Convective motions occur frequently in the lower photospheric layers of cool stars and many giants. They arise around optical depths where the radiative gradient is greater than the adiabatic gradient, as specified by the Schwarzschild criterion (Eq. 2.1). This condition is implemented in **PHOENIX** and crucially derived from the EOS, which results provide the chemical abundances for the opacities, required to determine the respective gradients. This is highly temperature and pressure dependent. Consequently, small variations in the T - and P -profiles can become decisive in certain layers for the emergence of stable convective currents.

To test the influence of **SESAM** on the temperature and pressure profiles of **PHOENIX**, the atmosphere of a M-dwarf with $T_{\text{eff}} = 3000$ K and $\log(g) = 4$ was modelled, taking

convection into account.

As a result, the synthetic atmosphere achieves a steady and fast convergence after 19 PHOENIX iterations. This is presented in Fig. 5.32, along with a comparison for ACES. Although the model with ACES was determined after the same number of iterations, the T -profile during the PHOENIX iterative process is somewhat different: SESAM results in stable and constantly decreasing changes in the temperatures whereas ACES causes fluctuations between the 43th and 64th photospheric layers. Simultaneously, exactly this region from $\tau_{\text{std},43} = 8.6 \cdot 10^{-3}$ down to $\tau_{\text{std},64} = 100$ marks the optical depths where convection occurs, according to the results of both EOS models. This shows a slightly unstable behaviour of ACES in convective layers. It is caused by ACES' inconsistent treatment of trace species and it neither occurs when ACES excludes them from the equilibrium problem (cf. Fig. 13 in the appendix), nor when SESAM is used.

Regarding the P -profiles, the application of SESAM shows in Fig. 5.33 in all optical depths and after each PHOENIX iteration a particular smooth behaviour. ACES, on the other hand, produces slight fluctuations in the pressures due to the consideration of trace species.

Nevertheless, comparing the final temperature and pressure values, the maximum deviations are marginal, i.e., $\sim 10^{-2}$ % and $\sim 10^{-1}$ %, respectively (Fig. 5.34).

Figure 5.35 compares the deviations in the concentrations of the five most abundant species in the atmosphere. The left panel reveals that differences in the T - and P -profiles of layers 5 - 16 are directly related to significant deviations in the concentrations of water, carbon monoxide and molecular hydrogen. An exclusion of trace species in ACES results in basically the same T - and P -profiles as when SESAM is applied. Accordingly, the right panel of Fig. 5.35 shows that the respective species deviations are only $\sim 10^{-3}$ %.

The peak in Fig. 5.34 around layer 43 cannot be associated with deviations in the five most relevant species. It is located in exactly the layer where the convection starts. This deviation in the T -profile does only occur when ACES includes trace species. It is consequently related to ACES' inconsistently calculated low-abundant species. The explicit consideration of trace species results, therefore, in slightly different chemical equilibria and, directly coupled with this, different opacities. The deviations are not sufficient to significantly influence the radiative and adiabatic gradients because the utilisation of both EOS's produces the same convective layers. However, the opacities deviate from each other enough to affect the respective temperatures throughout the atmosphere. This influences the resulting spectra: the deviations are $3.3 \cdot 10^{-1}$ % in the ultraviolet, $3.2 \cdot 10^{-2}$ % in the optical, $6.5 \cdot 10^{-3}$ % in the near-infrared, and $3.0 \cdot 10^{-3}$ % in the mid-infrared spectral ranges.

Notable is the fast convergence after only 19 PHOENIX iterations, compared to the test case from Sec. 5.1 where 87 iterations were required. The reason for this is the pre-computed atmosphere, the models relied on as a starting point. It was calculated taking convection into account, whereas the models in Sec. 5.1 excluded the consideration of convective motions. This exclusion prolongs the iterative process of PHOENIX because the model eventually converges to a different result, deviating stronger from the starting atmosphere. For instance, with increasing opacities, convective motions arise to transport the local radiative energy from the inner part of the atmosphere to the outer part. A synthetic atmosphere, which does not take this process into account, can easily result in considerably hotter lower regions than an atmosphere where heat is transported through convection.

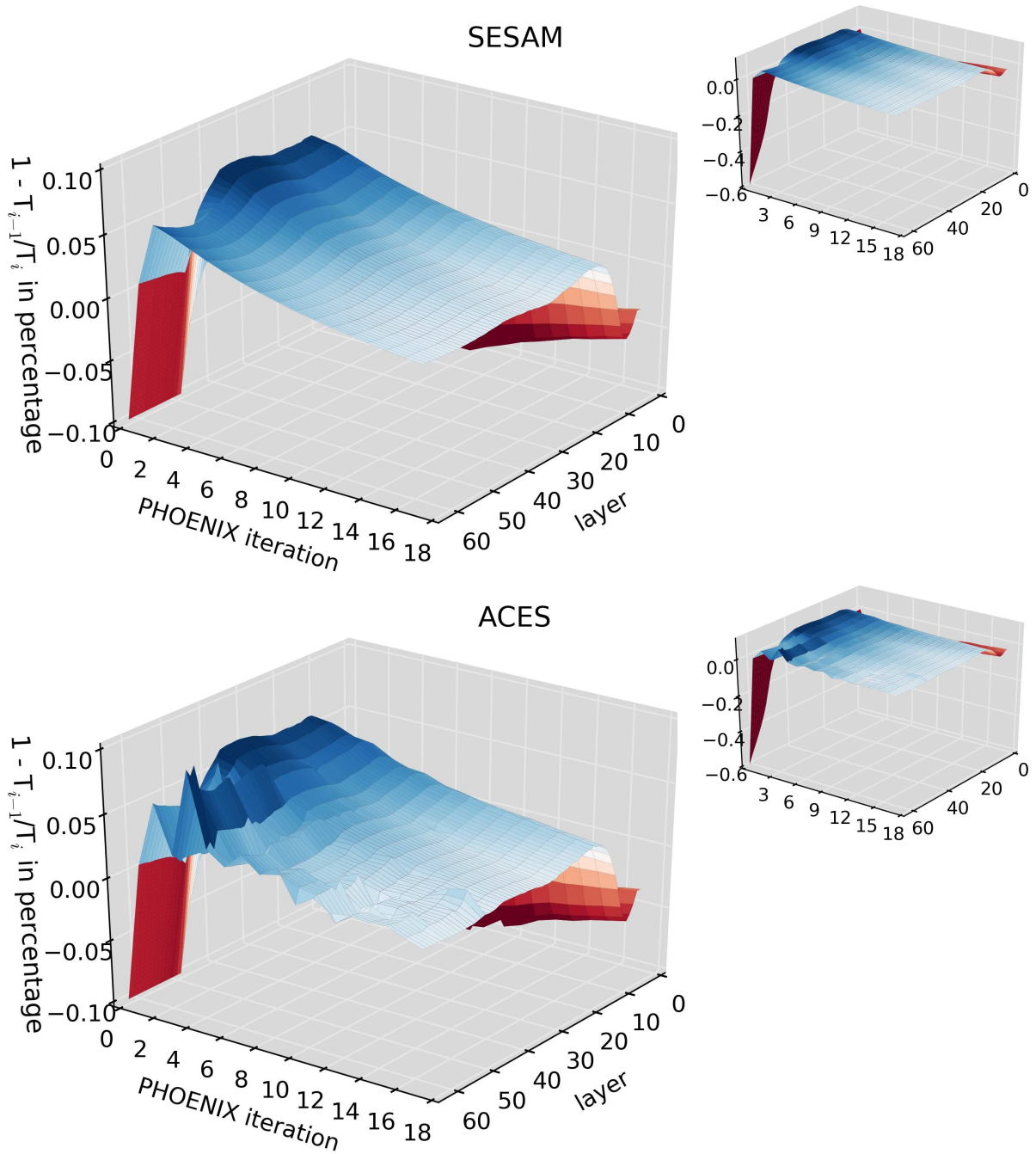


Figure 5.32: Changes in temperatures between the i^{th} iteration of PHOENIX, T_i , and the previous iteration, T_{i-1} , for each atmospheric layer and each PHOENIX iteration of a $T_{\text{eff}} = 3000$ K and $\log(g) = 4$ model with solar abundances and convection taken into account. The left panels are the reduced scale of the full-scale representations on the right side, using identical axes. SESAM and ACES were applied for the top and bottom panels, respectively.

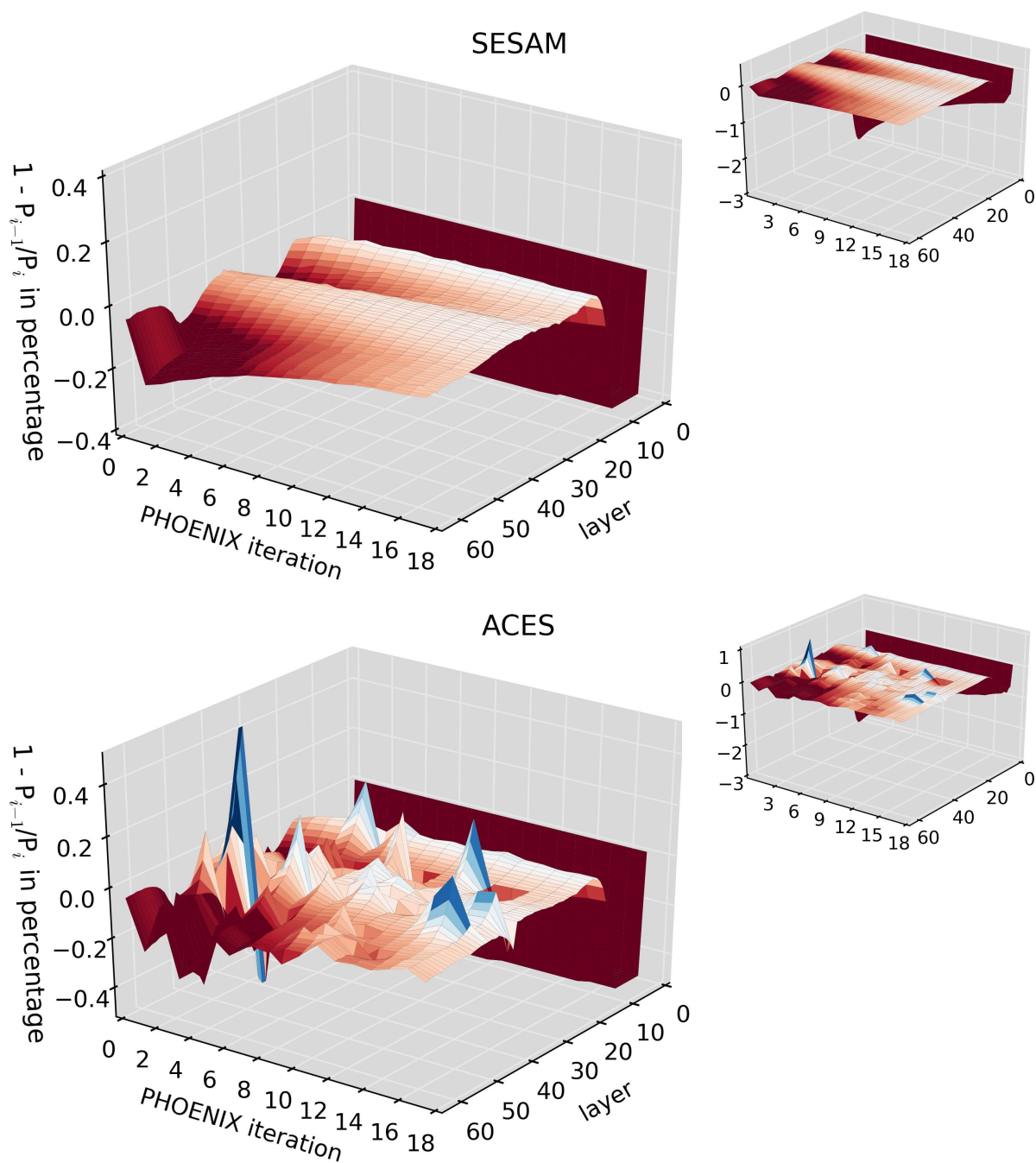


Figure 5.33: Changes in pressure between the i^{th} iteration of PHOENIX, P_i , and the previous iteration, P_{i-1} , for each atmospheric layer and each PHOENIX iteration of the same model atmosphere of Fig. 5.32. The left panels are the reduced scale of the full-scale representations on the right side, using identical axes. SESAM and ACES were applied for the top and bottom panels, respectively.

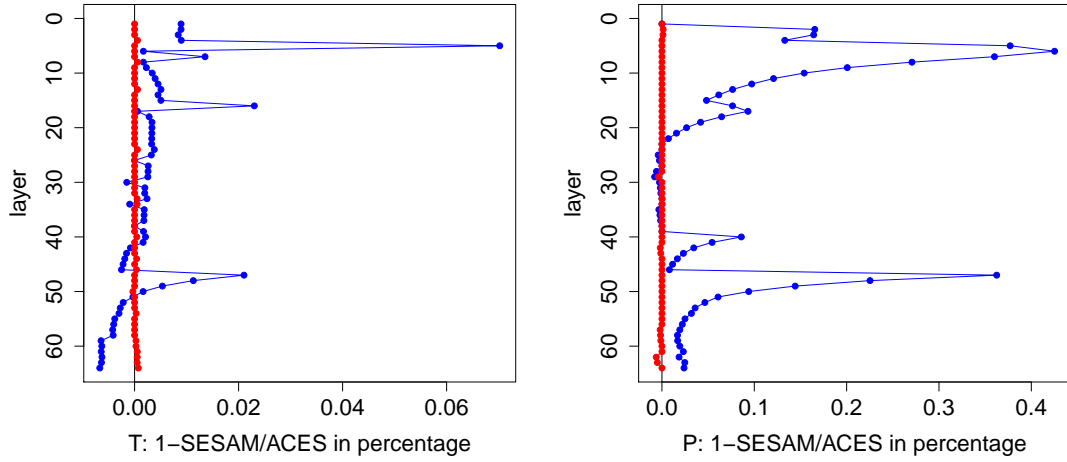


Figure 5.34: Percentage deviations in the final temperature (left) and pressure (right) profiles between SESAM and ACES for a model with $T_{\text{eff}} = 3000$ K and $\log(g) = 4$, including convective motions. In blue are the deviations between the codes when ACES takes trace species into account; in red are the deviations when ACES excludes them.

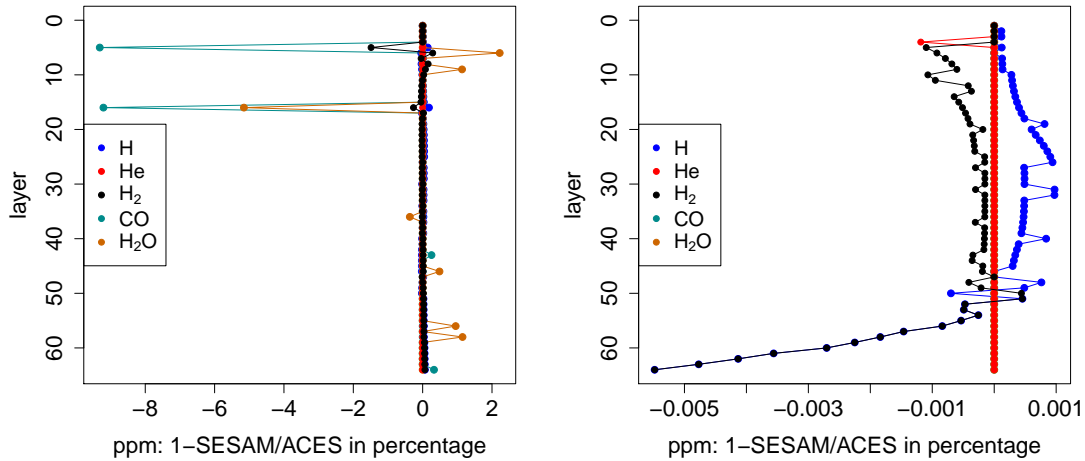


Figure 5.35: Percentage deviations of the relative concentrations (in ppm) of the five most abundant species H, He, H_2 , CO, and H_2O between SESAM and ACES of the same model of Fig. 5.34. In the left panel, ACES took trace species into account; in the right panel, ACES skipped the trace species.

5.5 Computational performance

It was shown above that **SESAM**'s inclusion in **PHOENIX** results in stable and reliable solutions of the atmospheric profile for different stars, covering a great variety of physical conditions. To quantify the computational time **SESAM** requires to determine the chemical equilibria, performance tests were made and compared with **ACES**' CPU times.

The read-in of the input parameter like the element abundances, the species list, the T - and P -points, and the thermodynamic data were deliberately excluded from the timing. To ensure an appropriate comparison between the different approaches considering the initially guessed species abundances, **SESAM**'s on-the-fly initial estimates calculation and **ACES**' import of the pre-computed partial pressure tables were included in the measurement. Furthermore, minor species were explicitly taken into account.

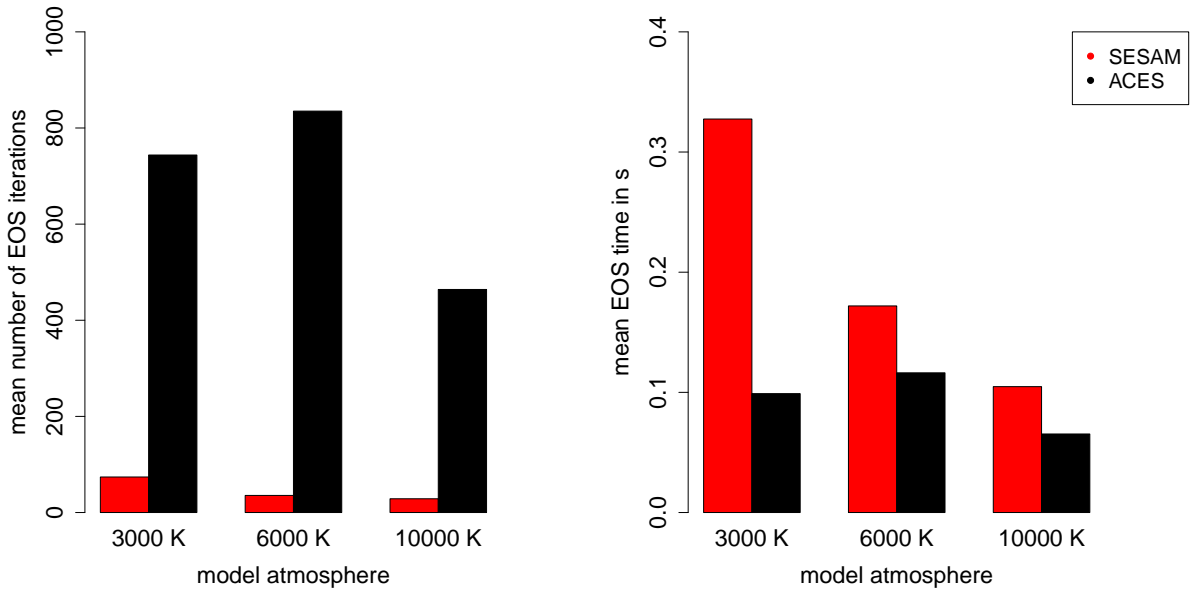


Figure 5.36: The left panel shows the mean number of all EOS iterations, averaging over 10 **PHOENIX** iterations for models with T_{eff} of 3000 K, 6000 K, and 10000 K, all with $\log(g) = 4$. The mean CPU times the EOS needed to compute the chemical equilibrium compositions during the 10 **PHOENIX** iterations are displayed in the right panel.

Figure 5.36 presents, in the left panel, the mean number of iterations that both EOS's needed to calculate the equilibrium compositions during 10 **PHOENIX** iterations of models with effective temperatures of 3000 K, 6000 K, and 10000 K. **SESAM** finds the chemical equilibria within significantly less iterations than **ACES**: on average 10 to 24 times fewer were required. This shows **SESAM**'s remarkable efficiency regarding its convergence behaviour (cf. Fig. 4.2). The right panel of Fig. 5.36 displays the respective mean CPU times, which the two EOS's needed for determining the final compositions for 10 **PHOENIX** iterations. Here, **SESAM** is 1.5 to 3.3 times slower than **ACES**. However, their performances are still of the same order of magnitude. The higher the effective temperature, the faster is **SESAM**: for 10 **PHOENIX** iterations of the 3000 K model, **SESAM** needed on average 0.3 s for solving the equilibrium problem, and it took only 0.1 s for the 10000 K model.

The reason for this is the complexity of the respective chemical compositions. For each PHOENIX iteration, equilibrium abundances are required for a broad range of temperatures and pressures. For instance, the model of a $T_{\text{eff}} = 3000$ K star includes temperatures from 1700 K to 8600 K and of a $T_{\text{eff}} = 10000$ K star temperatures from 5500 K to 25000 K. While only ionic and neutral atomic species are present at high temperatures, at low temperatures, in addition, a vast number of molecules must be taken into account. This affects especially the mean CPU times of the $T_{\text{eff}} = 3000$ K model where the biggest performance difference between the two EOS's occurs.

Although PHOENIX executes the EOS module more than a thousand times during each PHOENIX iteration, these small differences in CPU time between SESAM and ACES are generally irrelevant. Within PHOENIX, major computational effort is spent on the calculation of the opacities and the radiative transfer, due to fact that this is done for an enormous number of wavelength points, usually between $\sim 10^5$ and $\sim 10^6$ points. Regarding the total CPU time, which is required for a fully converged atmosphere, both EOS's account only a fraction of it. Since the calculation times of SESAM and ACES are in the same order of magnitude, it can be stated that SESAM's inclusion in PHOENIX does not significantly increase the total CPU times of PHOENIX while providing reliable results.

Chapter 6

Conclusions and Outlook

Conclusions

The new EOS **SESAM** has been successfully implemented as a module in the atmosphere modelling code **PHOENIX**. This work has created a basis for a substantial improvement of the simulation of atmospheres with terrestrial conditions. Now, targeted development of **PHOENIX** considering this field of application can proceed, building upon an EOS, which can reliably determine detailed chemical compositions at low temperatures. Some of these next steps will be discussed in the outlook below.

Tests considering the accuracy and reliability of **SESAM** with respect to specific temperatures and pressures and the capability of handling complex systems have already been performed by Meyer (2013). Therefore, the tests in Chapter 5 focused mainly on the investigation of the general interplay of the EOS and the **PHOENIX** framework.

For this purpose, twelve stars were considered in total, which involved various different physical conditions, varying from molecule-rich low-temperature atmospheres, to hot environments where mostly ions and neutral atoms are present in the atmosphere. Different surface gravities were chosen to imply a diversity in particle densities and extension of the photosphere. Furthermore, stars with convective motions, species treated in NLTE, and sub-solar chemical abundances were calculated.

In all the cases tested, the inclusion of **SESAM** resulted in a good and straightforward convergence of **PHOENIX** without any significant temperature and pressure variations between **PHOENIX** iterations for all optical depths. Furthermore, it was demonstrated that **SESAM** finds stable chemical compositions for slight variations in the temperature and pressure points.

To provide a direct comparison of **SESAM** with **ACES**, the currently used EOS in **PHOENIX**, all models were recalculated, utilising **ACES** under similar configurations: both EOS's were using the same thermodynamic data and trace species were explicitly taken into account at all time during the chemical equilibrium calculation. With exception to the hot models with an effective temperature of 10000 K, the application of **ACES** resulted in considerable pressure fluctuations between **PHOENIX** iterations. This effect is more pronounced in the cooler atmospheric layers. It is, therefore, directly related to low-temperature environments where the chemical composition is more complex with a high number of molecules. This unstable behaviour of **ACES** is caused by the inclusion of trace species in the equilibrium problem, indicating its difficulties in the construction of a reliable stoichiometric matrix in these cases. When **ACES** was applied in its standard configuration where trace species are

default to an arbitrarily chosen small value, the pressure fluctuations between PHOENIX iterations did not occur.

As a consequence, the final atmospheric temperature and pressure structures and the spectra of the respective converged models calculated with the two EOS's deviate slightly from each other. This can be directly related to deviations in the chemical compositions, determined by SESAM and ACES, letting PHOENIX converge to a different atmospheric equilibrium. Nevertheless, these deviations in the atmospheric temperature and pressure profiles are located in the lower single-digit percentage range, indicating that both EOS's are in an overall sufficient agreement with each other.

A proper treatment of low-abundance species should not be underestimated: due to the conservation of element abundances they still influence the other species' abundances and, in addition, they may contribute to the opacities in low-mass objects. Consequently, SESAM, with its ability to handle even a high number of trace molecules, is in this regard superior to ACES, which produces stable and reliable solutions only if trace species are excluded from the equilibrium problem.

The two EOS's are using initially guessed species abundances to accelerate their iterative process: SESAM calculates them on the fly with a simplex method, whereby ACES uses pre-computed partial pressure tables. It was shown that SESAM's equilibrium composition is independent from any value of the initial species abundances, providing in each case a very robust convergence behaviour of the code. On the other hand, the equilibrium composition determined by ACES relies on the starting abundances of the tables, making a stable solution of ACES problematic. Indeed a convergence of the PHOENIX model could have not been achieved in each case tested while using ACES. Again, this is an effect of the trace species, explicitly included in the equilibrium problem for testing purposes.

SESAM's inclusion of an initial estimate for the initial species abundances is an additional advantage of SESAM from which PHOENIX can benefit: the calculation, storing, reading in, and processing of pre-computed partial pressure tables are no longer necessary. In particular in multi-dimensional computations, the computational time required to perform the input and output operations for the partial pressure table can be saved. Furthermore, models with a wide variety of element abundances can be computed easily and without pre-computations of the respective partial pressure tables.

The computational performances of SESAM and ACES were measured. As a result, SESAM required in general 10 to 24 times fewer iterations than ACES to find the equilibrium composition, whereas ACES was 1.5 to 3.3 faster than SESAM. However, these differences are only marginal, compared to the CPU-time that PHOENIX spends on the calculation of the opacities and the radiative transfer.

Outlook

The overall positive interplay between PHOENIX and SESAM has been verified. The simulations in this thesis did not involve effects such as dynamic environments, multi-dimensional models, a high number of NLTE species, or the application of DRIFT. No deviation from the very good convergence behaviour of PHOENIX demonstrated in Chapter 5 is expected in these cases because the solution of the chemical equilibrium problem does not depend on these configurations. For the sake of completeness, these tests should be carried out, though. However, a direct comparison with ACES in such models is particularly interesting.

For instance, PHOENIX has occasionally shown convergence problems when calculating cool atmospheres using DRIFT. Stable equilibrium compositions for slight variations in the temperature and pressure values are particularly important in this context. The application of SESAM might provide a better convergence of these models.

It has been shown that the spectra of models calculated with SESAM and ACES deviate from each other, involving the lines of the neutral atoms, molecules, and ions. Considering specifically the analysis of cool objects like, e.g., M-dwarfs, there are still issues in the agreement between observed and synthetic spectra (e.g. Passegger et al., 2016). This may be due to numerous factors: the accuracy of the thermodynamic data, the opacities, and especially also the EOS, to name only a few. The fact that some spectral features are different with SESAM could already provide a model improvement. This could be evaluated by calculating a new PHOENIX model-grid with the application of SESAM and the subsequent comparison with observed spectra.

The computational performance of SESAM can be improved by a general optimisation of the code. Respective profiling tests may help in this context to analyse the run time. In addition, a parallelisation of all loops over non-component species is possible. For instance, the computation of the change of the reaction-extend variable $\delta\xi_j$ (Eq. 3.47) can be processed independently and, therefore, these calculations can be broken down in subtasks. However, a significant reduction of the CPU-time can be expected only when the chemical equilibrium problem includes a high number of species.

In Sec. 3.1, it was discussed why the ideal gas law is a valid approximation in photospheres of main-sequence stars. For a more accurate calculation of other objects, SESAM can be adapted to the respective equations of state of non-ideal gases. There are numerous equations of states developed, suitable for specific conditions or objects. For instance, an improvement of the calculation of white dwarfs could be achieved by including a degenerated equation of state. Regarding Earth-like atmospheric conditions, for regimes with high pressures and low temperatures, the ideal gas approximation does not accurately take into account phase-transitions. Furthermore, an appropriate expression of the chemical potentials has to be chosen to consider influences of, e.g., the interactions between the species. This can be done by means of the activity coefficients γ_i of species i , which quantify the strength of the deviation from the ideal gas. By replacing Eq. 3.19 with

$$\mu_i^{\text{non-ideal}} = \mu_i^*(T, P) + RT \ln \gamma_i(T, P, \mathbf{x})x_i, \quad (6.1)$$

the chemical potentials are now complex functions of temperature, pressure and composition and can be determined if the experimental values of the activity coefficients are provided.

With SESAM, PHOENIX has a new EOS, which is capable of finding the chemical compositions for low gas temperatures. The next step to significantly improve the accuracy of the simulation of terrestrial conditions is to include relevant line data and opacities of the chemical species in PHOENIX. However, regarding cool, low-mass objects like terrestrial planets, there are several processes that lead to deviations from the chemical equilibrium approximation. An overview of these processes is given in, e.g., Oswalt et al. (2013)

and Pielke et al. (1998), and only a few of them are briefly highlighted here. Such a chemical disequilibrium is given whenever radiative and hydrodynamic processes change the local conditions faster than the chemical reactions adapt to them. Photochemistry, e.g., photolysis and photo-catalysis, play an important role in low-density environments with respect to collisional processes. For instance, convection can transport molecules from deeper to upper atmospheric layers where they can be photo-dissociated by ultraviolet radiation. The radiative properties of the atmospheres can be strongly influenced by, e.g., dust grains, clouds formation, and the production of powerful greenhouse agents like soot and other atmospheric particulates produced by fire, volcanoes and a living vegetation. Electrical discharges temporarily affect the local chemical composition. Dust grains, aerosols and ice can form in the atmosphere and settle down, which removes them from the gas-phase equilibrium. However, they can be transported from one location to another by convective motions or by local or global winds, making a replenishment possible if they reach a temperature and pressure point where they evaporate. In addition, erosive up-streams can transport particles of soft rock into the atmosphere. There are further atmosphere-surface interactions: the temperature and pressure of the atmosphere determine if liquids and ice form, which shape the surface by rivers, oceans, or glaciers. In turn, these surface features influence the albedo of the planet, changing the radiative properties of the atmosphere. Other disequilibrium effects are caused by the fact that some chemical reactions proceed slower at low temperatures and low pressures like, for instance, the conversion from CO to CH₄ (Prinn and Barshay, 1977) making it necessary to take the respective time-scales of the reactions into account.

A proper numerical treatment of these complex processes requires, along with a vast number of measured and theoretical quantities, a time-dependent, multi-dimensional approach, which will be processable by coming generations of super-computing facilities. However, by means of simplifications and sufficiently low resolution, these processes can be modelled already today with current computational frameworks like PHOENIX. For instance, the inclusion of a modular disequilibrium treatment of selected species could open up numerous possibilities for the simulations of terrestrial (and other) environments. The disequilibrium processes mentioned above could be considered in a separate module by solving appropriate rate equations, or by explicit calculations. This feature is not implemented yet but could be realised as follows. First, PHOENIX provides SESAM the temperature, gas pressure, element abundances, and lists of species, which should be treated in equilibrium and in disequilibrium. Supplied with this input data, SESAM determines the respective equilibrium composition as described in the iterative scheme in Sec. 4.1, taking all species into account. If the abundances of the selected disequilibrium species are below a certain threshold, these disequilibrium species are assumed to be irrelevant for the disequilibrium processes, and the final equilibrium composition is found. However, if the abundances of the disequilibrium species are bigger than this threshold, their abundances are handed over to the module, which calculates their disequilibrium properties. The disequilibrium species are removed from the gas-phase equilibrium and, in order to provide the conservation of mass constraint for the equilibrium species, a new chemical equilibrium is determined by SESAM but, this time, excluding the disequilibrium species from the equilibrium problem. The resulting equilibrium composition of the equilibrium species is the final one. Finally, the respective abundances of all species are transferred to the PHOENIX main iteration.

As an alternative approach, the disequilibrium species can be considered as additional

constraint in **SESAM**. After **SESAM** hands over the disequilibrium species to the respective module, the module determines their disequilibrium properties and supplies **SESAM** with their new abundances. Instead of recalculating the chemical equilibrium without these species, they are treated as inert species in the recalculation. This provides a method to explicitly include the disequilibrium species in the gas-phase equilibrium while keeping their abundances fixed.

The level of detail for these procedures is limited only to the available computational power. For instance, **SESAM** could easily supply a list of all condensed species at the temperature-pressure locations to a climate module, making it possible for **PHOENIX** to take the influence of the global atmospheric circulation into account.

Appendix

ACES' atmospheric pressure structures with trace species skipped

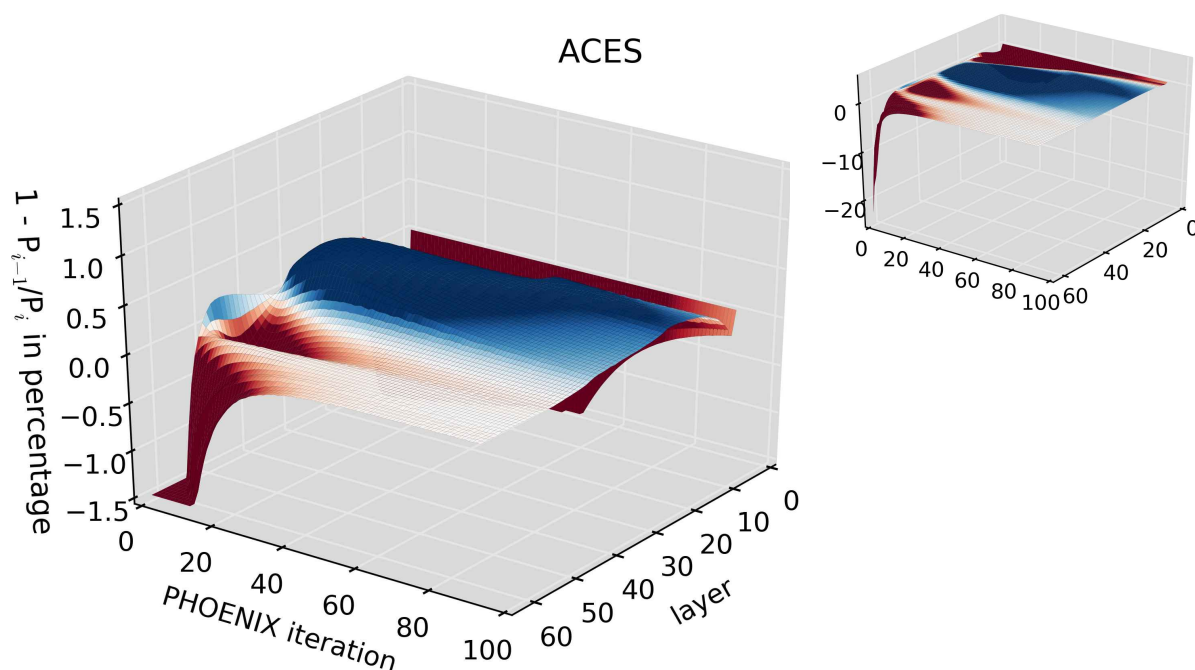


Figure 1: Changes in pressure between the i^{th} iteration of PHOENIX, P_i , and the previous iteration, P_{i-1} , for each atmospheric layer and each PHOENIX iteration. The left panel is the reduced scale of the full-scale representation on the right side, using identical axes. These plots show the ACES model with $T_{\text{eff}} = 3000$ K and $\log(g) = 3$, analogous to Fig. 5.2 but with trace species skipped.

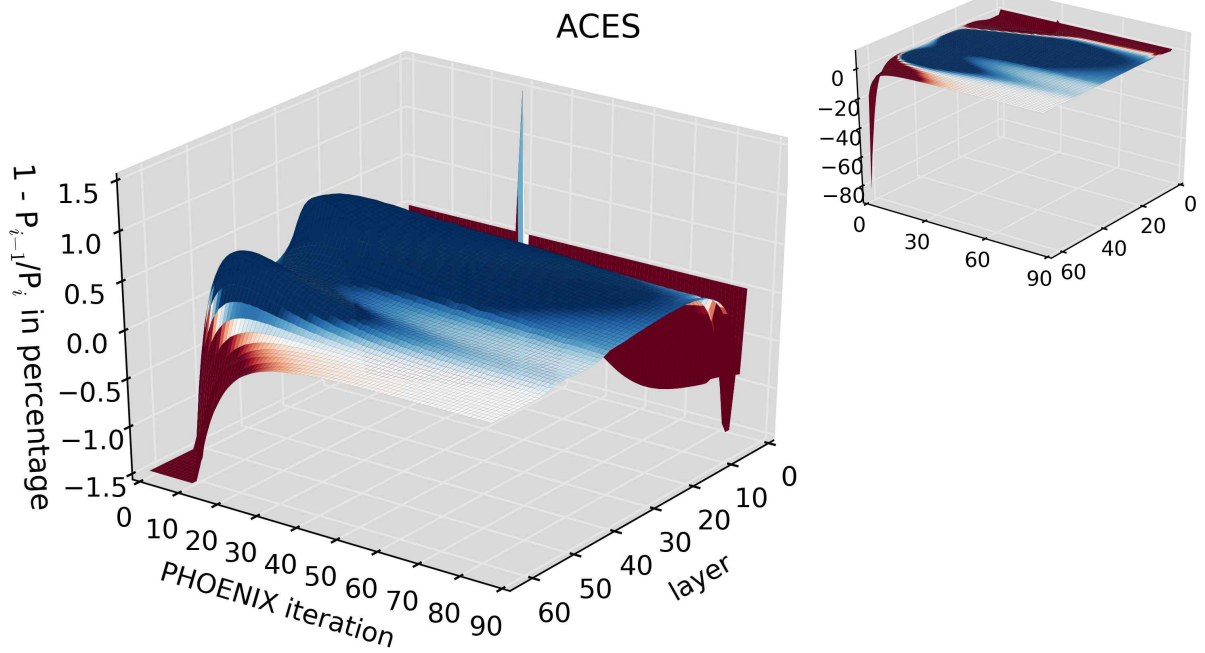


Figure 2: Same as in Fig. 1, but for a $T_{\text{eff}} = 3000$ K and $\log(g) = 4$ model, analogous to Fig. 5.3 but with trace species skipped.

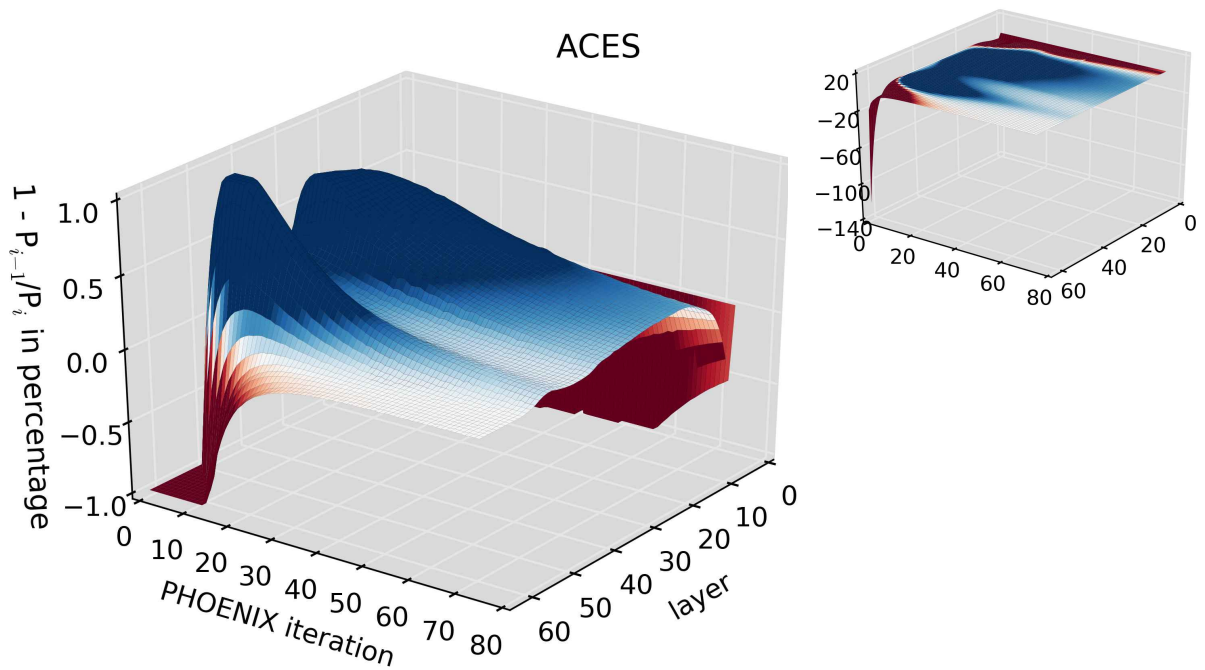


Figure 3: Same as in Fig. 1, but for a $T_{\text{eff}} = 3000$ K and $\log(g) = 5$ model, analogous to Fig. 5.4 but with trace species skipped.

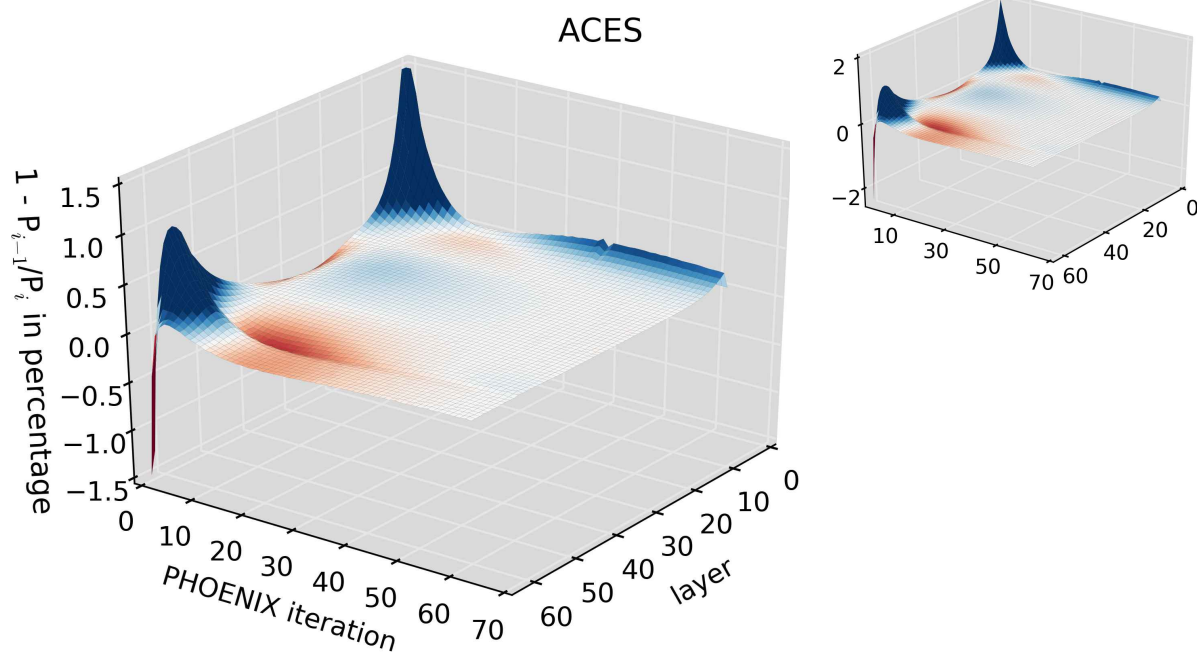


Figure 4: Same as in Fig. 1, but for a $T_{\text{eff}} = 6000$ K and $\log(g) = 3$ model, analogous to Fig. 5.5 but with trace species skipped.

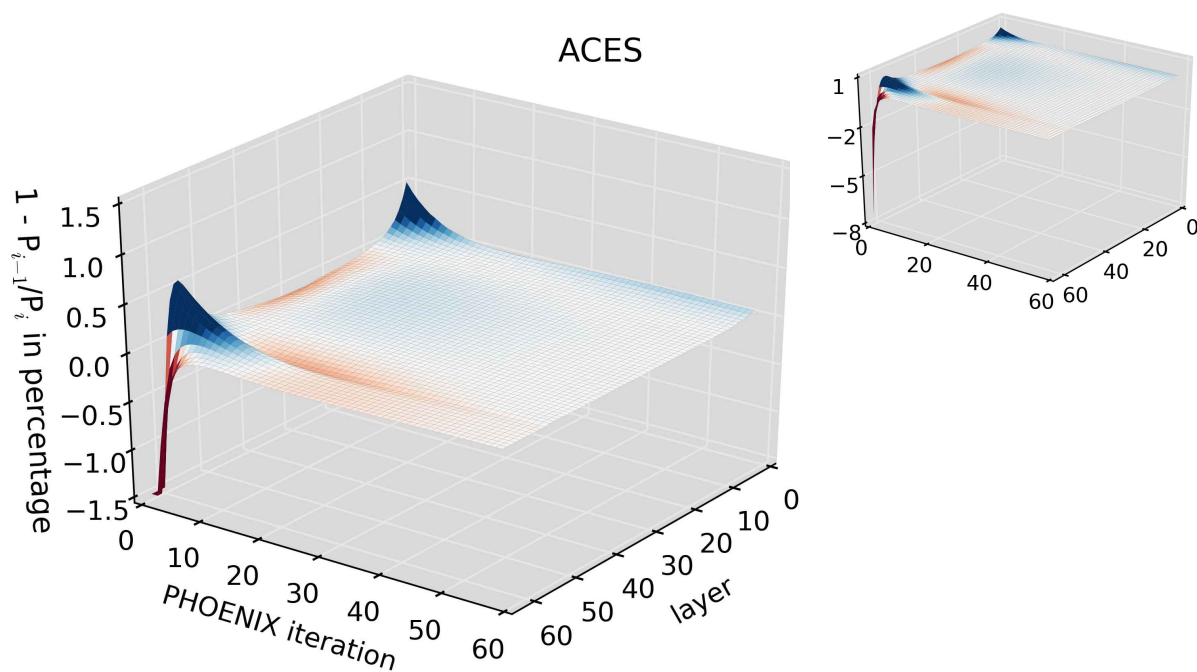


Figure 5: Same as in Fig. 1, but for a $T_{\text{eff}} = 6000$ K and $\log(g) = 4$ model, analogous to Fig. 5.6 but with trace species skipped.

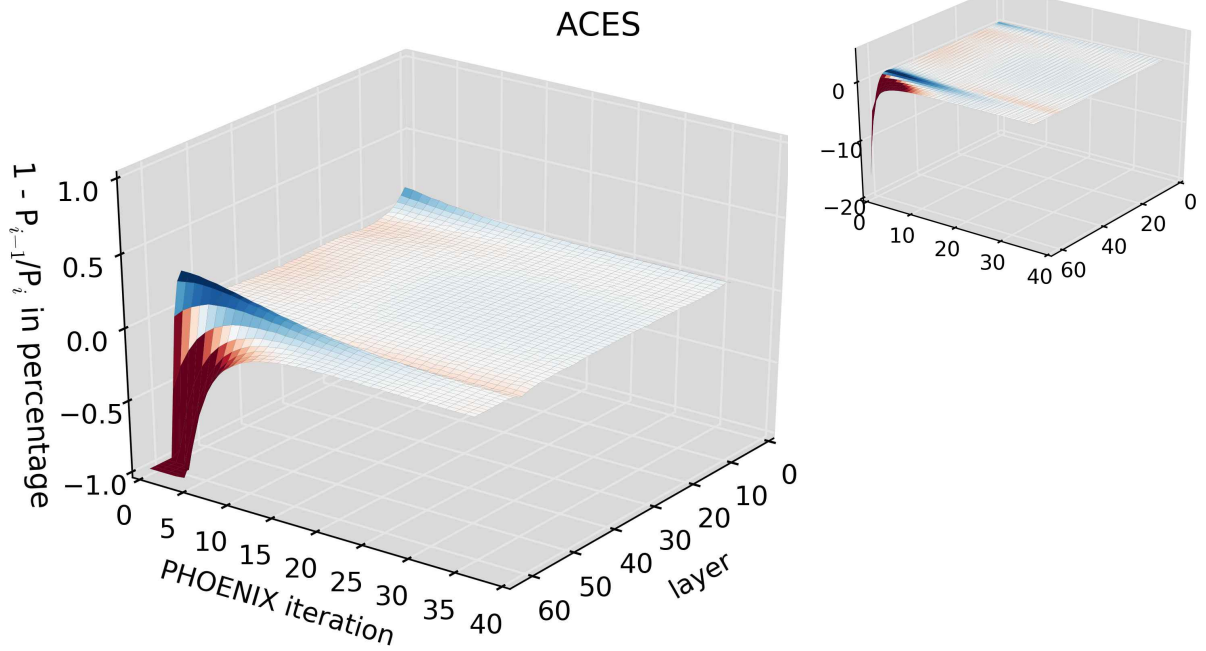


Figure 6: Same as in Fig. 1, but for a $T_{\text{eff}} = 6000$ K and $\log(g) = 5$ model, analogous to Fig. 5.7 but with trace species skipped.

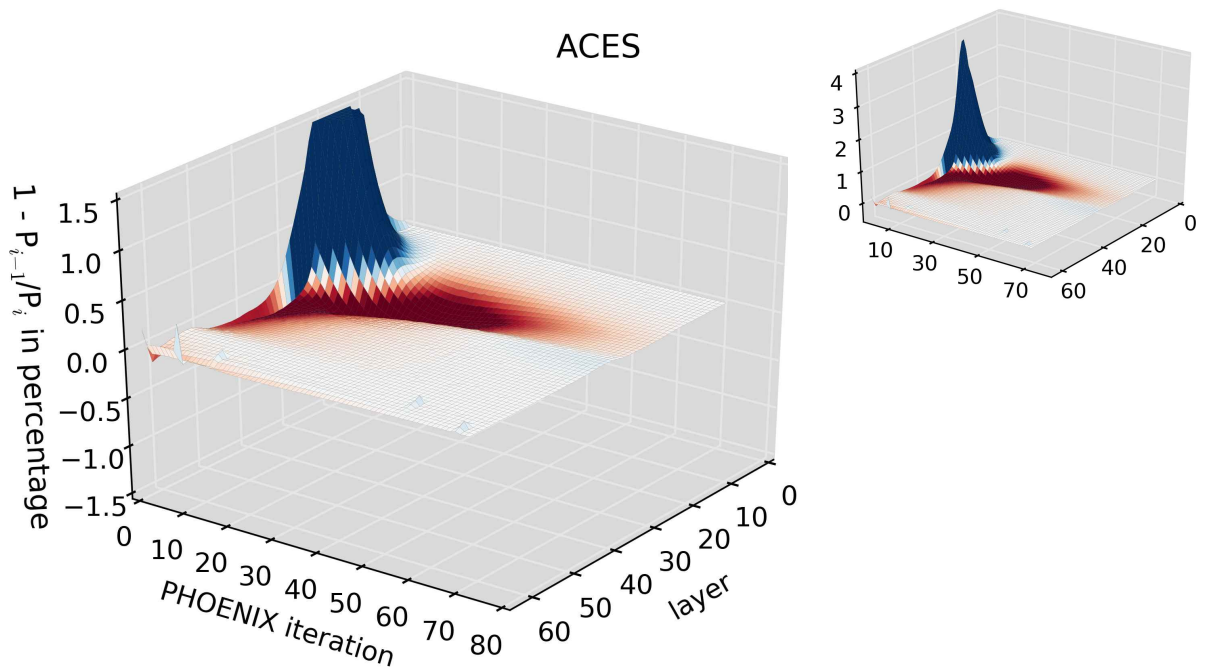


Figure 7: Same as in Fig. 1, but for a $T_{\text{eff}} = 10000$ K and $\log(g) = 3$ model, analogous to Fig. 5.8 but with trace species skipped.

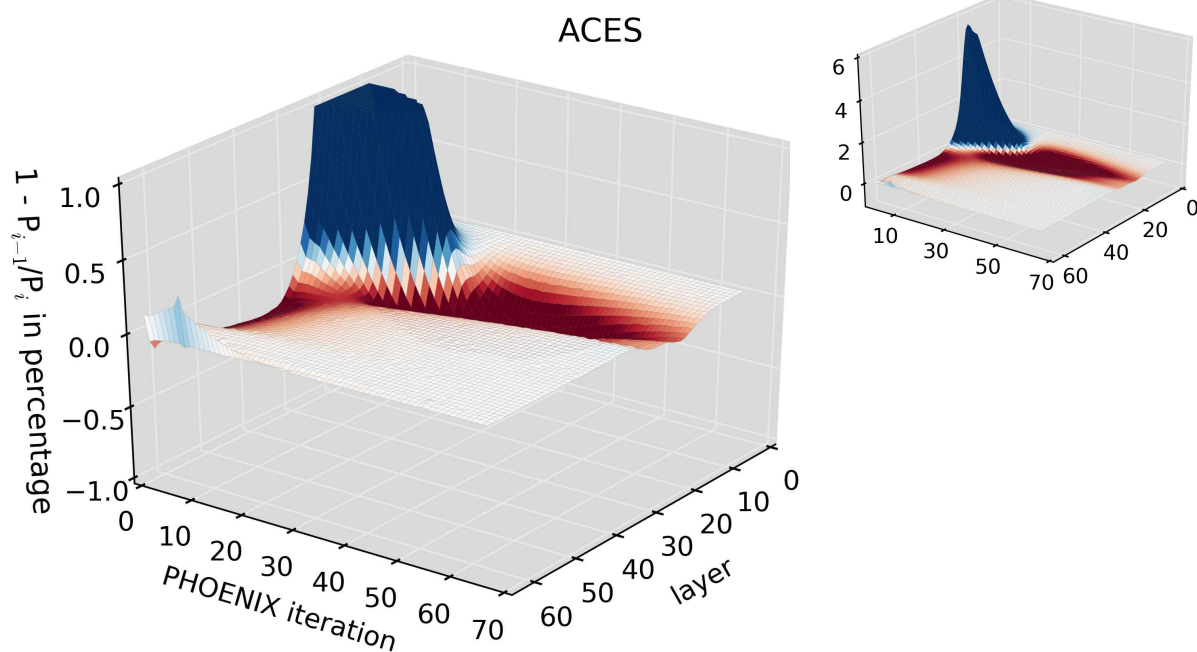


Figure 8: Same as in Fig. 1, but for a $T_{\text{eff}} = 10000$ K and $\log(g) = 4$ model, analogous to Fig. 5.9 but with trace species skipped.

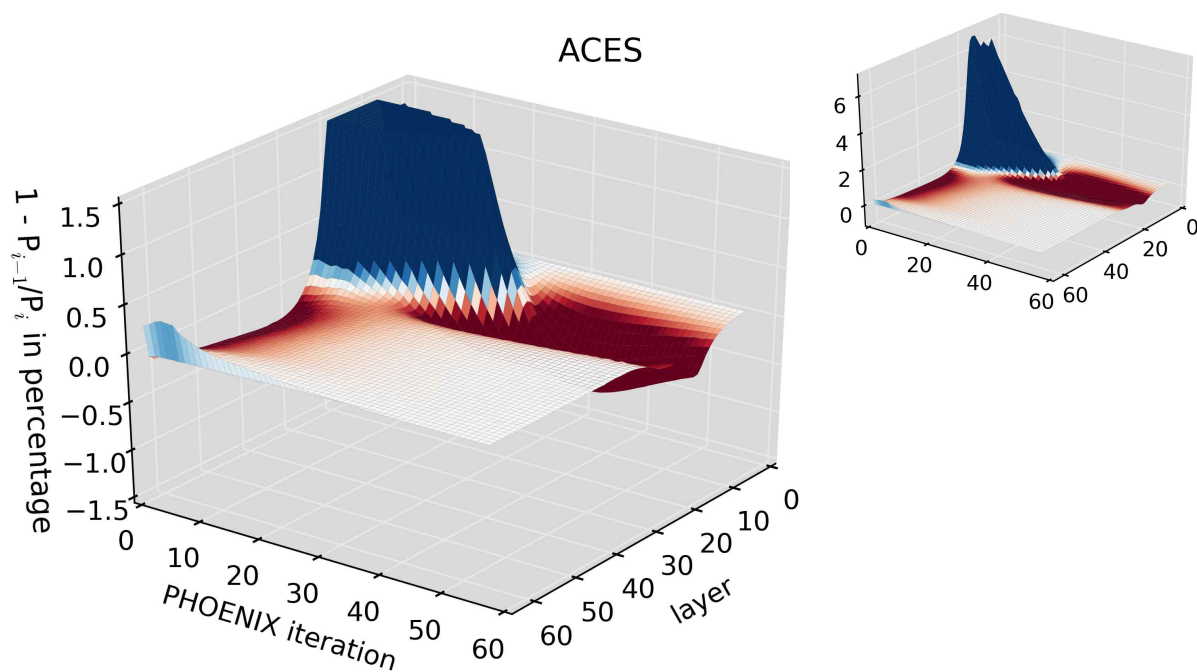


Figure 9: Same as in Fig. 1, but for a $T_{\text{eff}} = 10000$ K and $\log(g) = 5$ model, analogous to Fig. 5.10 but with trace species skipped.

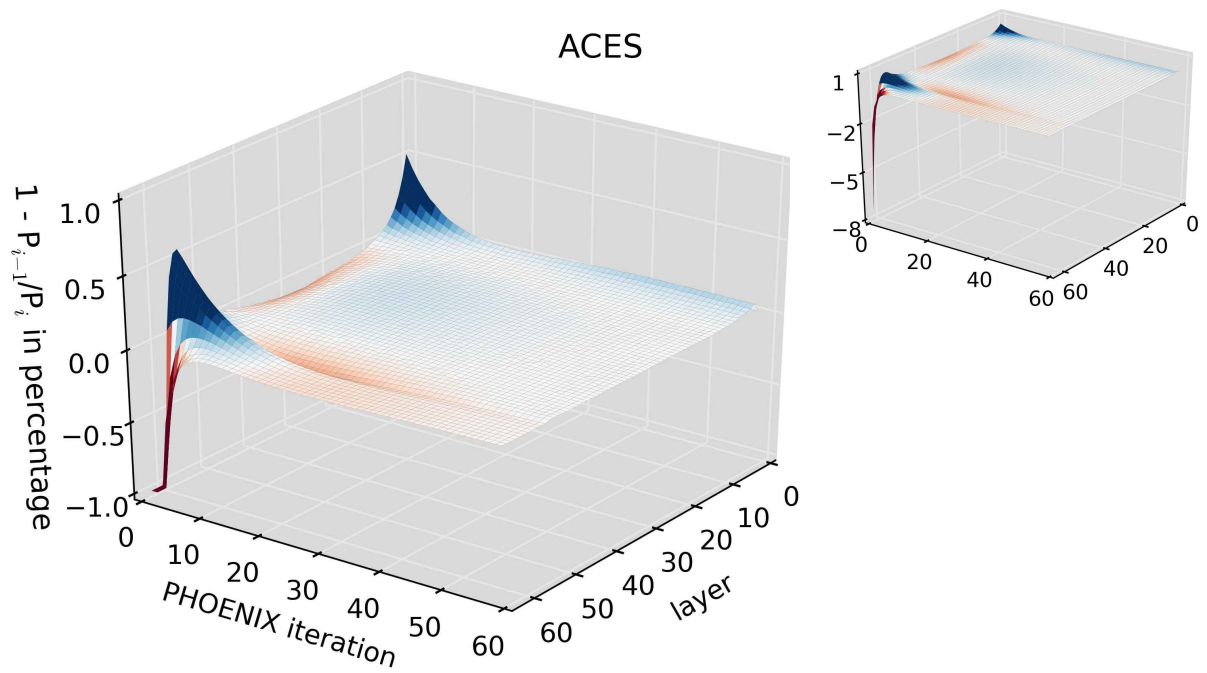


Figure 10: Same as in Fig. 1, but for a $T_{\text{eff}} = 6000$ K and $\log(g) = 4$ model with solar element abundances but using the partial pressure table with a metallicity of -2 as starting species abundances, analogous to Fig. 5.22 but with trace species skipped.

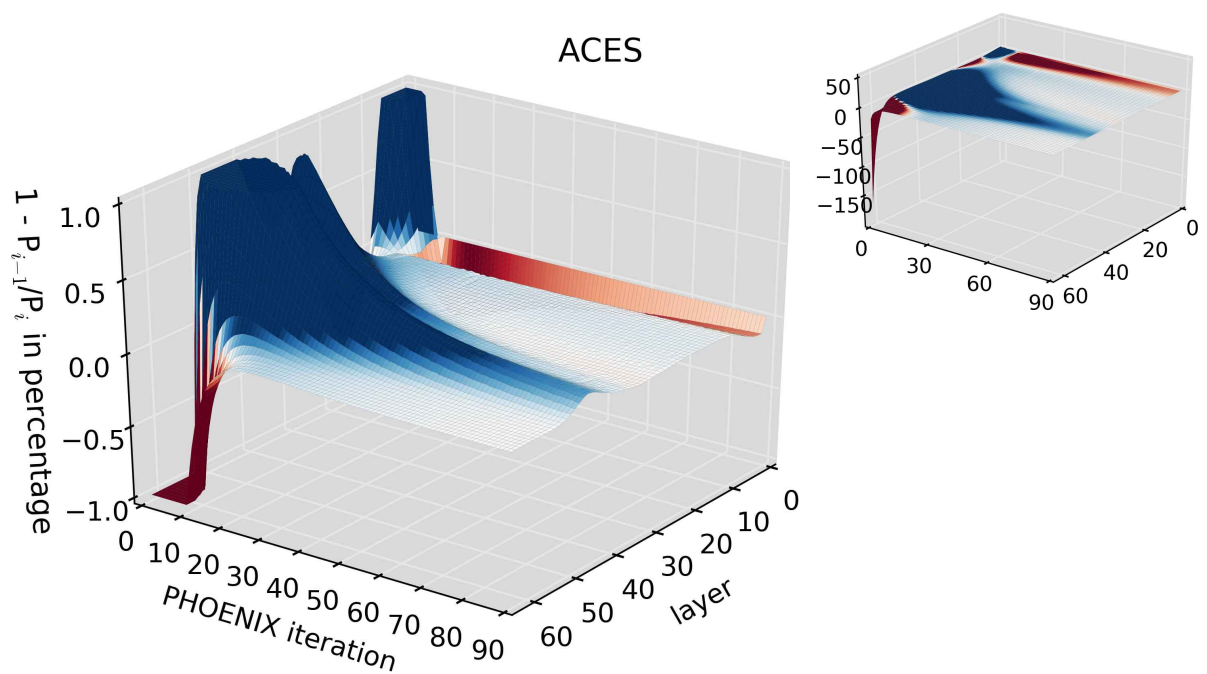


Figure 11: Same as in Fig. 1, but for a $T_{\text{eff}} = 3000$ K and $\log(g) = 4$ model with $[M/H] = -2$, analogous to Fig 5.28 but with trace species skipped.

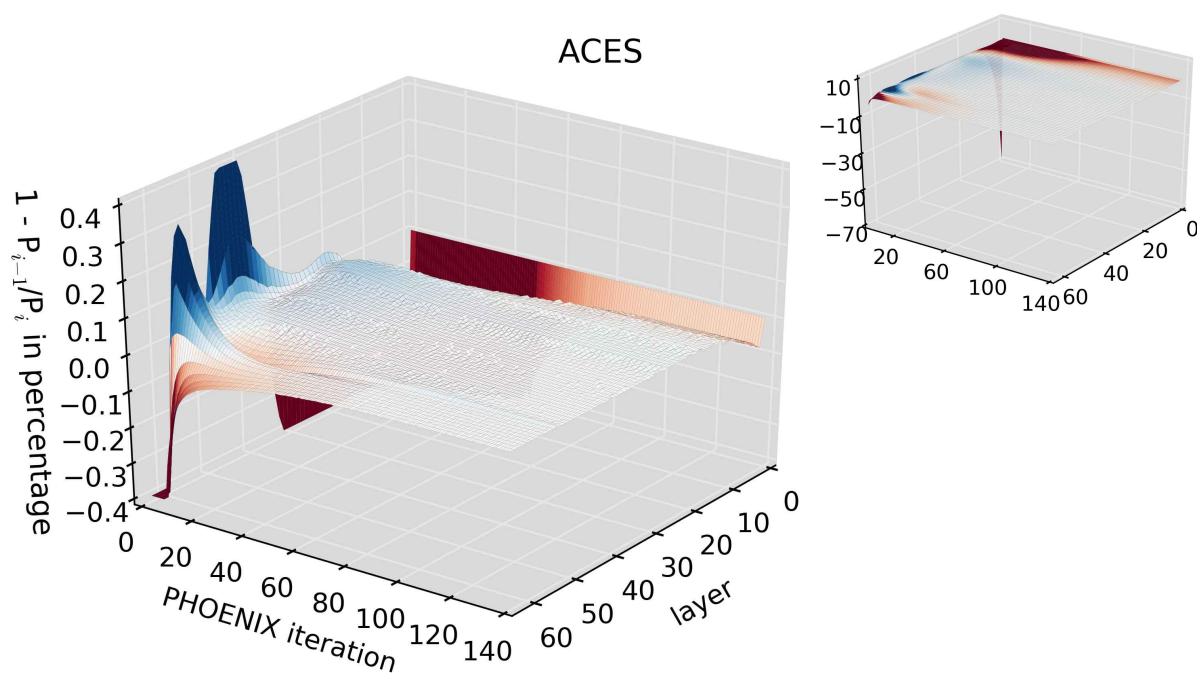


Figure 12: Same as in Fig. 1, but for a $T_{\text{eff}} = 6000$ K and $\log(g) = 4$ model with solar abundances, assuming the species H and He being treated in NLTE, analogous to Fig. 5.30 but with trace species skipped.

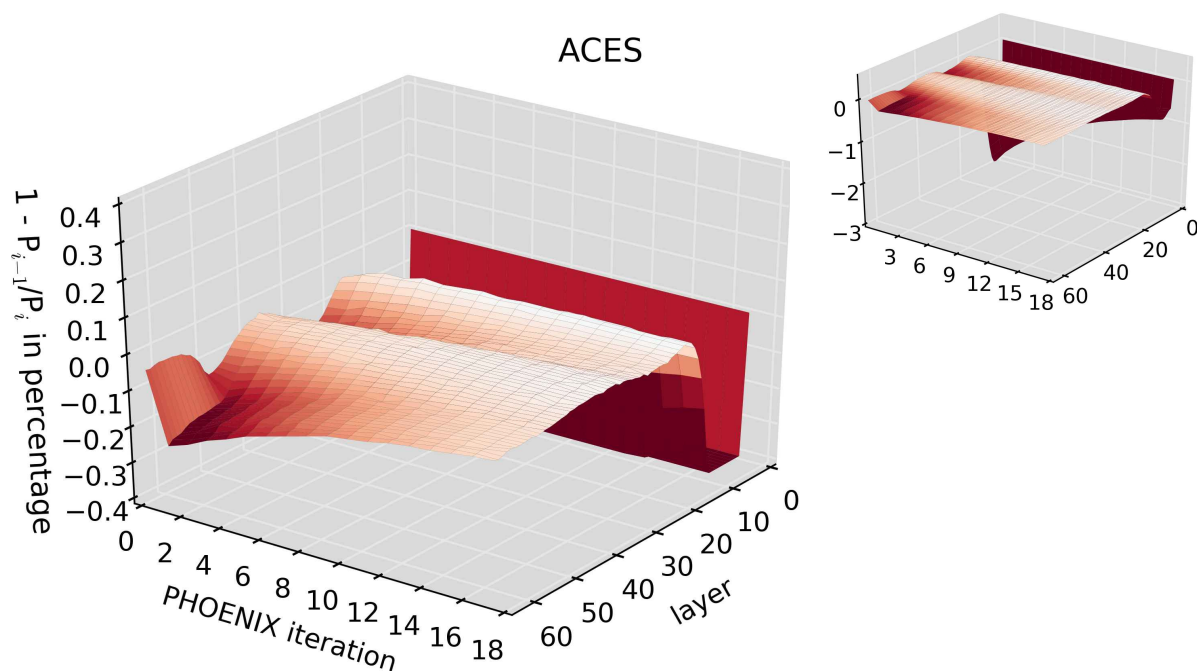


Figure 13: Same as in Fig. 1, but for a $T_{\text{eff}} = 3000$ K and $\log(g) = 4$ model with solar abundances and convection taken into account, analogous to Fig. 5.33 but with trace species skipped.

Bibliography

- P. S. Bishnu, D. Hamiroune, M. Metghalchi, and J. C. Keck. Constrained-equilibrium calculations for chemical systems subject to generalized linear constraints using the nasa and stanjan equilibrium programs. *Combustion Theory and Modelling*, 1(3):295–312, 1997.
- E. Böhm-Vitense. Über die Wasserstoffkonvektionszone in Sternen verschiedener Effektivtemperaturen und Leuchtkräfte. Mit 5 Textabbildungen. *Zeitschrift für Astrophysik*, 46:108, 1958.
- E. Böhm-Vitense and G. D. Nelson. About the proper choice of the characteristic length in the convection theory. *The Astrophysical Journal*, 210:741–749, 1976.
- A. Botnen and M. Carlsson. Multi3d, 3d non-lte radiative transfer. In *Numerical astrophysics*, pages 379–382. Springer, 1999.
- S. Boyd and L. Vandenberghe. *Convex optimization*. Cambridge university press, 2004.
- S. R. Jr. Brinkley. Calculation of the equilibrium composition of systems of many constituents. *The Journal of Chemical Physics*, 15(2):107–110, 1947. doi: 10.1063/1.1746420. URL <http://link.aip.org/link/?JCP/15/107/1>.
- C. J. Cannon. Angular quadrature perturbations in radiative transfer theory. *Journal of Quantitative Spectroscopy and Radiative Transfer*, 13(7):627–633, 1973.
- M. Carlsson. A computer program for solving multi-level non-lte radiative transfer problems in moving or static atmospheres. In *Physics of Formation of FeII Lines Outside LTE*, pages 273–275. Springer, 1988.
- B. W. Carroll and D. A. Ostlie. *An Introduction to Modern Astrophysics*. Pearson Addison-Wesley, 2007. ISBN 9780805304022.
- M. W. Chase. Nist-janaf thermochemical tables fourth edition part i-ii. *Journal of Physical and Chemical Reference Data*, Monograph No. 9, 1998.
- H. L. L. Chatelier. Le chatelier’s principle. *Comptes rendus*, 99:786–789, 1884.
- R. Clausius. X. on a modified form of the second fundamental theorem in the mechanical theory of heat. *The London, Edinburgh, and Dublin Philosophical Magazine and Journal of Science*, 12(77):81–98, 1856.
- T. De Donder and P. Van Rysselberghe. *Thermodynamic theory of affinity*, volume 1. Stanford university press, 1936.

- M. Dehn. *Self-consistent Dust Modelling in Brown Dwarfs*. PhD thesis, Universität Hamburg, Von-Melle-Park 3, 20146 Hamburg, 2007. URL <http://ediss.sub.uni-hamburg.de/volltexte/2007/3255>.
- E. Freedman. Blake - A Thermodynamic Code Based on Tiger: User's Guide and Manual. *Technical Report ARBRL-TR-02411, Ballistic Research Laboratory, US Army Armament Research and Development Command*, (AD/A-121-259), 1982.
- B. Freytag, M. Steffen, and B. Dorch. Spots on the surface of betelgeuse— results from new 3 d stellar convection models. *Astronomische Nachrichten*, 323(3-4):213–219, 2002.
- J. W. Gibbs. *A method of geometrical representation of the thermodynamic properties of substances by means of surfaces*. Connecticut Academy of Arts and Sciences, 1873.
- S. Gordon and B. J. McBride. Computer program for computation of complex chemical equilibrium compositions, rocket performance, incident and reflected shocks, and chapman-jouguet detonations. *NASA SP-273*, 1971.
- S. Gordon and B. J. McBride. Computer program for calculation of complex chemical equilibrium compositions and applications. part 1: Analysis. *NASA reference publication*, 1311, 1994.
- G. Gräfener, L. Koesterke, and W.-R. Hamann. Line-blanketed model atmospheres for wr stars. *Astronomy & Astrophysics*, 387(1):244–257, 2002.
- C. M. Guldberg and P. Waage. Studies concerning affinity, cm forhandlinger: Videnskabs-selskabet i, 1864.
- B. Gustafsson, R.A. Bell, K. Eriksson, and Å. Nordlund. A grid of model atmospheres for metal-deficient giant stars. i. *Astronomy & Astrophysics*, 42:407–432, 1975.
- P. H. Hauschildt. A fast operator perturbation method for the solution of the special relativistic equation of radiative transfer in spherical symmetry. *Journal of Quantitative Spectroscopy and Radiative Transfer*, 47(6):433–453, 1992.
- P. H. Hauschildt. Multi-level non-lte radiative transfer in expanding shells. *Journal of Quantitative Spectroscopy and Radiative Transfer*, 50(3):301–318, 1993.
- P. H. Hauschildt and E. Baron. Numerical solution of the expanding stellar atmosphere problem. *Journal of Computational and Applied Mathematics*, 109(1):41–63, 1999.
- P. H. Hauschildt and E. Baron. A 3d radiative transfer framework-xi. multi-level nlte. *Astronomy & Astrophysics*, 566:A89, 2014.
- P. H. Hauschildt, T. S. Barman, E. Baron, and F. Allard. Temperature correction methods. In *Stellar Atmosphere Modeling*, volume 288, page 227, 2003.
- Ch. Helling, P. Woitke, and W.-F. Thi. Dust in brown dwarfs and extra-solar planets-i. chemical composition and spectral appearance of quasi-static cloud layers. *Astronomy & Astrophysics*, 485(2):547–560, 2008.

- I. Hubeny. A computer program for calculating non-lte model stellar atmospheres. *Computer Physics Communications*, 52(1):103–132, 1988.
- I. Hubeny. *Planets, Stars and Stellar Systems, Vol. 4 Stellar Structure and Evolution*. Springer Reference, 2013. ed. Oswalt, T. D. and Barstow, M. A.
- I. Hubeny and D. Mihalas. *Theory of Stellar Atmospheres: An Introduction to Astrophysical Non-equilibrium Quantitative Spectroscopic Analysis*. Princeton University Press, 2014.
- V. N. Huff, S. Gordon, and V. E. Morrell. General method and thermodynamic tables for computation of equilibrium composition and temperature of chemical reactions. *NACA Technical Report 1037*, 1951.
- T.-O. Husser, S. Wende-von Berg, S. Dreizler, D. Homeier, A. Reiners, T. Barman, and P. H. Hauschildt. A new extensive library of phoenix stellar atmospheres and synthetic spectra. *Astronomy & Astrophysics*, 553:A6, 2013.
- G. Job and F. Herrmann. Chemical potential - a quantity in search of recognition. *European journal of physics*, 27(2):353, 2006.
- J. Keck. Rate-controlled constrained-equilibrium theory of chemical reactions in complex systems. *Progress in Energy and Combustion Science*, 16(2):125–154, 1990.
- R. L. Kurucz. Atlas: A computer program for calculating model stellar atmospheres. *SAO Special report*, 309, 1970.
- R. L. Kurucz and B. Bell. Atomic line list. <http://kurucz.harvard.edu/atoms.html>, 2011.
- B. J. McBride and S. Gordon. Computer program for calculation of complex chemical equilibrium compositions and applications, ii. users manual and program description. *NASA reference publication*, 1311:84–85, 1996.
- B. J. McBride, M. J. Zehe, and S. Gordon. Nasa glenn coefficients for calculating thermodynamic properties of individual species. 2002.
- M. H. Metghalchi. Rate-controlled constrained-equilibrium (rcce) modeling of propulsive performance of energetic materials in a hypersonic nozzle. Technical report, Northeastern University Boston MA, Dept. of Mechanical Engineering, 2009.
- M. Meyer. *General Equation of State for Gaseous Environments*. Thesis (M. Sc.), Universität Hamburg, 2013.
- D. Mihalas. *Stellar atmospheres*. W.H. Freeman and Company, San Francisco, 1970. ISBN 0716703335.
- D. Mihalas. *Stellar atmospheres (2nd edition)*. W.H. Freeman and Company, San Francisco, 1978.
- C. E. Mortimer and U. Müller. *Chemie: Das Basiswissen der Chemie*. Georg Thieme Verlag, 2014.

- L. M. Naphtali. Complex chemical equilibria by minimizing free energy. *The Journal of Chemical Physics*, 31(1):263–264, 1959. doi: 10.1063/1.1730307. URL <http://link.aip.org/link/?JCP/31/263/1>.
- L. M. Naphtali. Calculate complex chemical equilibria. *Industrial and Engineering Chemistry*, 53(5):387–388, 1961. doi: 10.1021/ie50617a028. URL <http://pubs.acs.org/doi/abs/10.1021/ie50617a028>.
- T. D. Oswalt, L. M. French, and P. Kalas. *Planets, Stars and Stellar Systems: Volume 3: Solar and Stellar Planetary Systems*. Springer Netherlands, 2013.
- V. M. Passegger, A. Reiners, S. V. Jeffers, S. Wende, P. Schöfer, P. J. Amado, J. A. Caballero, D. Montes, R. Mundt, Ig. Ribas, et al. Spectroscopic characterisation of carmenes target candidates from feros, cafe and hrs high-resolution spectra. *arXiv preprint arXiv:1607.08738*, 2016.
- R. A. Pielke, R. Avissar, M. Raupach, A. J. Dolman, X. Zeng, A. S. Denning, et al. Interactions between the atmosphere and terrestrial ecosystems: influence on weather and climate. *Global change biology*, 4(5):461–475, 1998.
- S. B. Pope. The computation of constrained and unconstrained equilibrium compositions of ideal gas mixtures using gibbs function continuation. *FDA03-02, Cornell University*, 2003.
- W. H. Press. *Numerical recipes in Fortran 77: the art of scientific computing*, volume 1. Cambridge university press, 1992.
- R. G. Prinn and S. S. Barshay. Carbon monoxide on jupiter and implications for atmospheric convection. *Science*, 198(4321):1031–1034, 1977.
- Reaction Design. CHEMKIN, [Online]. Available: <http://www.reactiondesign.com/products/chemkin/> [2016, January 12]., 2016.
- N. I. Reid and S. L. Hawley. *New light on dark stars: red dwarfs, low-mass stars, brown dwarfs*. Springer Berlin Heidelberg, 2005.
- W. C. Reynolds. The element potential method for chemical equilibrium analysis: Implementation in the interactive program stanjan, version 3. Technical report, 1986.
- M. M. Ruda. A comparison of solution methods for the chemical equilibrium problem, 1982.
- R. J. Rutten. *Radiative transfer in stellar atmospheres*. Utrecht University lecture notes, 8th edition, 2003.
- M. Schwarzschild. *Structure and Evolution of the Stars*. Dover Publications Inc., 1958.
- W. R. Smith. The computation of chemical equilibria in complex systems. *Industrial & Engineering Chemistry Fundamentals*, 19(1):1–10, 1980. doi: 10.1021/i160073a001. URL <http://dx.doi.org/10.1021/i160073a001>.

- W. R. Smith and R. W. Missen. Calculating complex chemical equilibria by an improved reaction-adjustment method. *Can. J. Chem. Eng.*, 46:269–272, 1968.
- W. R. Smith and R. W. Missen. What is chemical stoichiometry? *Chemical Engineering Education*, 13(1):26–32, 1979.
- W. R. Smith and R. W. Missen. *Chemical reaction equilibrium analysis: theory and algorithms*. Wiley series in chemical engineering. Wiley, 1982. ISBN 9780471093473.
- E. E. Stone. Complex chemical equilibria: Application of newton-raphson method to solve non-linear equations. *Journal of Chemical Education*, 43(5):241, 1966. doi: 10.1021/ed043p241. URL <http://dx.doi.org/10.1021/ed043p241>.
- J. H. Van't Hoff. *Etudes de dynamique chimique*, volume 1. Muller, 1884.
- H.-H. Voigt. *Abriss der Astronomie*. John Wiley & Sons, 2012.
- W. B. White, S. M. Johnson, and G. B. Dantzig. Chemical equilibrium in complex mixtures. *The Journal of Chemical Physics*, 28(5):751–755, 1958. doi: 10.1063/1.1744264. URL <http://link.aip.org/link/?JCP/28/751/1>.
- F.C. Wong, J.J. Gottlieb, and L.-S. Lussier. Chemical equilibrium analysis of combustion products at constant volume. Technical report, Defence Research and Development Canada - Valcartier Tech. Rep. DRDC Valcartier TR-2003-375, 2003.

Danksagung

Ich danke herzlich Peter Hauschild für die Vergabe dieses wunderbaren Themas, die hilfreichen Anmerkungen und dafür, diese Arbeit zu begutachten.

Großer Dank gilt Prof. Dr. Ralph Neuhäuser für die Bereitschaft, Zweitgutachter zu sein.

Dem Sternwartenpersonal, insbesondere Angelika Kleinoth und Anke Vollersen, danke ich für die stets freundliche Hilfsbereitschaft bei allen verwaltungs- und buchtechnischen Angelegenheiten.

Sören Witte und Andreas Schweitzer danke ich sehr herzlich für die hilfreichen Diskussionen und das Korrekturlesen dieser Arbeit. Besonders dir, Sören, danke ich für deine Begleitung und Unterstützung durch die letzten Jahren, angefangen mit meiner Bachelorarbeit.

Ein ganz besonderer Dank geht an Sebastian Knop: Knop, du gabst mir die Machete für meinen Weg durch den Dschungel in die Hand. Und sobald sie während der Reise stumpf wurde, warst du rettend mit dem Schleifstein da und zeigtest mir aufmunternd, an welchen Stellen ich sie schärfen sollte. Dabei vergaßst du nie, im Vorbeigehen noch auf einen vielversprechenden Pfad zu deuten. Ich danke dir zutiefst und von ganzem Herzen für deine Unterstützung und deine Zuversicht auf dieser Expedition.

Der PHOENIX Arbeitsgruppe danke ich für die vielen gemeinsamen Pizzaessen, das Aufdecken von Spionen, das Sammeln von Artefakten und das Achterbahnfahren. Achterbahn! Wir haben Mafiamopster ausgehebelt, Zeppeline bestiegen, wurden von THE ORDER OF THE CRIMSON HAND traumatisiert und haben sie schlußendlich besiegt. Es war toll mit euch!

Mein tiefster, liebevollster Dank gebührt Ivan De Gennaro Aquino. Unerschütterlich gabst du mir Kraft, Halt, Unterstützung, Freude und Liebe wie ich sie noch nie zuvor erlebt habe. Danke, dass du für mich da bist, für deine Geduld, deine Pizza und den kontinuierlichen Koffeinnachschub im Haus. Du bist einfach unglaublich. *..every single day of my life..*

Eidesstattliche Versicherung

Hiermit versichere ich an Eides statt, die vorliegende Dissertationsschrift selbst verfasst und keine anderen als die angegebenen Hilfsmittel und Quellen benutzt zu haben.

Die eingereichte schriftliche Fassung entspricht der auf dem elektronischen Speichermedium.

Die Dissertation wurde in der vorgelegten oder einer ähnlichen Form nicht schon einmal in einem früheren Promotionsverfahren angenommen oder als ungenügend beurteilt.

Hamburg, den 03.05.2017